UNIVERSITÀ DEGLI STUDI DI CATANIA

Dottorato di Ricerca in Scienza dei Materiali e Nanotecnologie – XXIX Ciclo

---

Antonino Rapisarda

Localized Surface Plasmon Resonance: Nanoscale Sensing for Processes at Interfaces

Tutor: Prof. re Giovanni Marletta

Coordinatore: Prof. ssa Maria Grazia Grimaldi

Tesi per il conseguimento del titolo

LOCALIZED SURFACE PLASMON RESONANCE:

NANOSCALE SENSING FOR PROCESSES AT INTERFACES

by

ANTONINO RAPISARDA

B. S. University of Catania, Italy 2012

M. S. University of Catania, Italy 2013

A dissertation submitted in partial fulfillment of the requirements
for the degree of Doctor of Philosophy
in Material Science and Nanotechnologies
in the Department of Chemistry,
at the University of Catania,
Italy

November 2016

Major Professor: Giovanni Marletta

ABSTRACT

This PhD thesis reports the use the emerging surface-sensitive optical technique of localized surface plasmon resonance (LSPR) to characterize the interaction of relevant classes of biomolecules, e.g. peptides, proteins, lipids and DNA strands, at solid-liquid interfaces, with an emphasis on deciphering kinetics and pathways of dynamic adsorption processes.

LSPR-based biosensor exploits the high sensitivity of the plasmon frequency to refractive index changes confined to 5-30 nanometers around the metal nanoparticles deposited on the sensor surface to monitor in situ and in real time the interaction of unlabeled biological molecules skipping the misleading contribution from the bulk of solution affecting conventional optical technique, e.g. SPR and OWLS.

In the present dissertation the advantages of applying this powerful technique are thoroughly demonstrated by investigating four case studies concerning relevant aspects for the biointerfaces science. The case of study 1 will involve the adsorption kinetics of single and binary solution of proteins onto model hydrophilic and hydrophobic surfaces. The analysis of the adsorption kinetics reveals that competitive adsorption occurs, at physiological pH 7.4 and relatively high ionic strength (NaCl 0.1 M), favoring the heavier protein (fibronectin, in our case), which is shown to adsorb faster and in larger amount than the lighter one (human serum albumin, in our case). The case of study 2 will discuss the DNA hybridization process for binary solutions of respectively perfectly matching (PM) and single base mismatching (MM) 93-mer ssDNA from KRAS codon 12, with a surface tethered probe complementary to the PM sequence. Sensitivity down to obtaining down to 10 nM and 13 nM, respectively for PM and MM were obtained, showing that the hybridization process occurs at a lower rate for MM with respect to PM target. The competitive hybridization was accounted for by an inhibition model, where the non-complementary sequences kinetically hinder the hybridization of the perfect matching sequences, owing to their above mentioned affinity constant differences for the same probe. The case of study 3 will cover the kinetics of phospholipid vesicle adsorption on silicon oxide surfaces as function of pH. Two different regimes have been observed for acidic and basic conditions. At low pH, vesicles adsorption showed one-step exponential kinetics. Moreover, no significantly variation of the adsorption rate was observed over the investigated pH range 3-6, suggesting the process is controlled by Van der Waals interactions and steric forces. At high pH, vesicles adsorb showing two-step kinetic. Furthermore, it was observed that the rate of the first step slows down linearly with the increasing of pH, suggesting that the process is primarily driven by vesicle-surface electrostatic repulsion. The case of study 4 will report preliminary results from the study of pH stimuli-responsive smart surfaces, formed by gold nanodisks array of an LSPR sensor chip decorated with Trichogin GA IV and two of its positively-charged analogs, i.e. Lipo-Lys and L20, in which four and eight Lysines positive charged residues have been introduced respectively. The surface-bound peptides exhibit reversible and rapid switching between conformations and can withstand several cycles of swelling and collapsing with no significant loss from the surfaces.

Overall, the results here reported demonstrated the great potential of LSPR technique as a unique tool to monitor specific and non-specific biomolecular interactions at interfaces in application fields ranging from biosensing to materials science.

ACKNOWLEDGMENTS

First and foremost I wish to thank my advisor, professor Giovanni Marletta for giving me the opportunity of conducting my research as part of his team. His continuous support during years, the integration into running projects combined with the possibility to bring my own ideas and the freedom to conduct own measurements were most important for this thesis. Furthermore I would like to thank him for his patience while correcting my papers and for the injection of motivation coming from every single discussion we had.

In addition, I would like to express my deep and sincere gratitude to Dr. Nicoletta Giamblanco for fruitful collaboration on several projects and for sharing both my cheers and frustrations with experimental work during the whole period of the Ph. D study.

I would also like to thank you Dr. Grazia M.L. Messina for giving me the possibility to take part in the research project “Peptide conformational switches: design, synthesis and characterization” and for the numerous on- and off topic discussion. I also thank Dr. Marta De Zotti from University of Padua for having supplied the peptides for my research.

Special thanks to all my past and present colleagues in the Laboratory for Molecular Surface and Nanotechnology (LAMSUN) for invaluable help and a jolly work environment. In particular Gianfranco Sfuncia and Vanna Torrisi introduced me to atomic force microscopy and have helped me in various circumstances.

Finally, I wish to express gratitude to our administrative, Sabrina Tosto. I do not want to imagine what it would have been like to attempt this feat without your outstanding professional support.

TABLE OF CONTENT

APPENDIX 2: A. Rapisarda, N. Giamblanco, G. Marletta. Kinetic Discrimination of DNA single-base mutations by Localized Surface Plasmon Resonance. Journal of Colloid and Interface Science 487 (2017) 141-148.

APPENDIX 3: A. Rapisarda, N. Giamblanco, G. Marletta. Kinetics Study of Adsorption Competition at hydrophobic and hydrophilic surfaces. Colloids and Surfaces B: Biointerfaces (Manuscript submitted)

LIST OF FIGURES

LIST OF TABLES

INTRODUCTION

Motivation and Aim of the thesis

Adsorption of molecules from solution is one of the most fundamental processes in soft matter physics/surface chemistry [1]. All amphiphilic molecules – surfactants, polar lipids, surface active polymers – have a tendency to adsorb at surfaces [2].

There is a broad range of applications where adsorption of a biological relevant macromolecules at a solid surface is a key event [3], such as solid-phase immunoassay for medical diagnostic tests [4], prediction and preventing unfavourable consequences of blood coagulation caused by artificial implants [5], or biofilms used on contact lenses [6], and oil-in-water emulsions in food industry stabilized by sodium caseinate [7].

Monitoring the adsorption process is not easy [8]. Adsorption is a reversible and often highly dynamic process and the adsorbed layer is usually very thin, just a monolayer [9]. Therefore, detailed characterization of adsorbed layers and efficient monitoring of adsorption processes require very high surface-sensitivity analytical techniques able to follow interfacial interactions in situ and in real time [10]. Another highly desirable quality of these techniques is the ability to monitor biomolecules-surface interactions avoiding any step of labeling which is tedious, and often occupies the active sites of the biomolecules [11].

During recent years nanoplasmonic biosensing platforms have emerged as a powerful tool to investigate interfacial phenomena, taking the advance of optical phenomena such as extraordinary optical transmission and localized surface plasmon resonance (LSPR) for high-sensitivity measurements [12]. The main advantages of the LSPR technique consists of a relatively short penetration depth (about 10−20 nm compared to, e.g., 100−600 nm and around 250 nm for conventional SPR and quartz crystal microbalance (QCM), respectively) [13]. The LSPR penetration depth is comparable to the length scale of most of relevant biomacromolecules, and so offers a better resolution in the detection of these analytes [14]. Nevertheless LSPR technique has great potential for label-free, in situ tracking of biomolecules adsorption kinetic, up to now most publication concern with lipid vesicles adsorption kinetics [15].

The aim of this dissertation is to demonstrated the general applicability of the LSPR technique for investigating adsorption kinetics of relevant class of biomolecules, e.g. peptides, proteins, lipids and DNA, onto solid surfaces. This approach enabled us to gain new insights into the underlying mechanisms of softmatter interactions with solid surfaces.

Thesis outline

A brief summary of the chapters is provided below.

Chapter 1:*"Nanoplasmonic based refractive index sensors".* This chapter introduces fundamentals of localized surface plasmon resonance (LSPR) phenomenon, its physical modeling and relevant parameters. It is followed by a review of experimental setup for LSPR measurements with emphasis on wavelength-shift detection method and its sensing performance.

Chapter 2:*" Kinetics Study of Adsorption Competition at hydrophobic and hydrophilic surfaces".* This chapter describes the use of silica coated gold nanodisks array as a sensor for monitoring the adsorption of proteins with specific biological interest, i.e. fibronectin and albumin, on hydrophilic and hydrophobic model surfaces obtained by functionalizing the LSPR sensor chips. The amount and rate of protein adsorbed on the tested surfaces are monitored in real time from both single and binary protein solutions. The results shows that Fibronectin adsorption is more efficient than albumin one during both transport phase and surface affinity driven step.

Chapter 3:*" Kinetic Discrimination of DNA single-base mutations by LSPR".* This chapter describes the use of gold nanodisks array to reveals surface hybridization reactions. The gold nanodisks are functionalized with thiol modified ssDNA probe, followed by a real-time measurement monitoring the binding interactions of perfect match (PM) and single base mismatch (MM) ssDNA from both pure and binary mixture target solution. Limits of detection of 10 nM and 13 nM respectively for PM and MM were determined. The presented biosensor was not only useful for DNA quantification purposes, but also to reveal the binding kinetics occurring at the sensor surface. The observed kinetics for competitive hybridization are modeled for by an inhibition model, where the non-complementary sequences kinetically hinder the hybridization of the perfect matching sequences owing to their above mentioned affinity constant differences for the same probe.

Chapter 4:*"Influence of pH on Kinetics of Phospholipid Vesicles Adsorption".* In this chapter presents the study of the adsorption of small unilamellar vesicles (SUV) of palmitoyloleoylphosphatidylcholine (POPC) on silicon dioxide surfaces as a function of pH buffer. The results show that the kinetic pathway of the transformation of spherically closed lipid bilayers to supported lipid bilayers changes according to the ionization state of the substrate and phospholipid molecules.

Chapter 5:"*Preliminary study on pH-induced reversible stretching-contracting modes in stimuli-responsive peptabiotics".* The pH-induced swelling and collapse of the gold nanodisks surface-bound peptides bearing ionizable groups in lateral chain were quantified in real time by in situ LSPR measurement in liquid environment. Switching between peptide conformations at pH values of 3 and 11 is rapid and reversible, and it is characterized by swelling factors (difference maximum thickness-minimum thickness) that increase as the number of ionizable group introduced in the peptide backbone.

Chapter 6: *"Conclusions"*. The experiments conducted to achieve the project aim of this thesis are summarized and the major conclusions are drawn.

Appendix 1:*" Complementary experimental techniques".* This chapter presents the complementary techniques used within this thesis and the principles relating to their application. The relevant theoretical background, data treatment and interpretation are outlined.

References

1. V. Hlady, J. Buijs. Protein adsorption on soli. d surfaces. Curr. Opin. Biotechnol. 7 (1996) 72–77.
2. M. Rabe, D. Verdes, S. Seeger. Understanding protein adsorption phenomena at solid surfaces. Advances in Colloid and Interface Science 162 (2011) 87-106.
3. J. Talbot, G. Tarjus, P.R. Van Tassel, , P. Viot. From car parking to protein adsorption: an overview of sequential adsorption processes. Colloids and Surfaces A: Physicochemical and Engineering Aspects. 165 (2000) 287-324.
4. K. K. Jain. Applications of Nanobiotechnology in Clinical Diagnostics. Clinical Chemistry 53 (2007) 2002-2009.
5. K. M. Hansson, S. Tosatti, J. Isaksson, J. Wetterö, M. Textor, T.L. Lindahl, Pentti Tengvall. Whole blood coagulation on protein adsorption-resistant PEG and peptide functionalized PEG-coated titanium surfaces. Biomaterials 26 (2005) 861-872.
6. J. L. Bohnerr, T. A. Horbetr, B. D. Rarner, F. H. Roycef. Adsorption of Proteins From Artificial Tear Solutions to Contact Lens Materials. Investigative Ophthalmology & Visual Science 29 (1988) 362-373.
7. Eric Dickinson. Flocculation of protein-stabilized oil-in-water emulsions. Colloids and Surfaces B: Biointerfaces 81 (2010) 130-140.
8. K. Nakanishi, T. Sakiyama, K. Imamura. On the adsorption of proteins on solid surfaces, a common but very complicated phenomenon. Journal of Bioscience and Bioengineering 91 (2001) 233-244.
9. K. E. Sapsford, F. S. Ligler. Real-time analysis of protein adsorption to a variety of thin films. Biosensors and Bioelectronics 19 (2004) 1045-1055.
10. J. Vörös. The Density and Refractive Index of Adsorbing Protein Layers. Biophysical Journal 87 (2004) 553-561.
11. M. A. Cooper. Label-free screening of bio-molecular interactions. Anal. Bioanal. Chem. 377 (2003) 834–842.
12. M. C. Estevez, M. A. Otte, B. Sepulveda, L. M. Lechuga. Trends and challenges of refractometric nanoplasmonic biosensors: A review. Analytica Chimica Acta 806 (2014) 55-73.
13. B. Sepúlveda, , P. C. Angeloméb, L. M. Lechugaa, , L. M. Liz-Marzánb. LSPR-based nanobiosensors. Nano Today 4 (2009) 244-251.
14. A. Dmitriev. (2012) Nanoplasmonic Sensors. New York, NY: Springer.
15. J. A. Jackman, V. P. Zhdanov, N. Cho. Nanoplasmonic Biosensing for Soft Matter Adsorption: Kinetics of Lipid Vesicle Attachment and Shape Deformation. Langmuir 30 (2014) 9494-9503.

LIST OF PUBLICATIONS

Journal articles (peer-reviewed)

1. A. Rapisarda, N. Giamblanco, G. Marletta. Kinetic Discrimination of DNA single-base mutations by Localized Surface Plasmon Resonance. Journal of Colloid and Interface Science 487 (2017) 141-148.
2. A. Rapisarda, N. Giamblanco, G. Marletta. Kinetics Study of Adsorption Competition at hydrophobic and hydrophilic surfaces. Colloids and Surfaces B: Biointerfaces (submitted).
3. A. Rapisarda, G. Marletta. Kinetics of phospholipid vesicles adsorption controlled by pH studied by Localized Surface Plasmon Resonance. (Manuscript in preparation).
4. G.M.L. Messina, M. De Zotti, A. Rapisarda, F. Formaggio and G. Marletta. pH-induced reversible stretching-contracting modes in stimuli-responsive peptabiotics (Manuscript in preparation).

Conference contributions (oral presentations)

1. Characterization of biopolymer thin films by localized surface plasmon-enhanced nanosensors; A. Rapisarda*, N. Giamblanco and G. Marletta. Macrogiovani 2016 – Associazione Italiana di Scienze e Tecnologia delle Macromolecole (AIM), Catania, Italia 12-13 Maggio 2016.
2. pH-induced reversible stretching-contracting modes in stimuli-responsive peptabiotics; G.M.L. Messina*, M. De Zotti, A. Rapisarda, F. Formaggio and G. Marletta; E-MRS 2016 Spring Meeting, Lille Grand Palais, 2-6 Maggio 2015

Conference contributions (poster presentations)

1. Protein adsorption processes studied by localized surface plasmon resonance nanosensors; A. Rapisarda* and G.Marletta; E-MRS 2015 Spring Meeting, Lille Grand Palais, 11-15 Maggio 2015;

CHAPTER 1.

NANOPLASMONIC BASED REFRACTIVE INDEX SENSORS

1.1 Introduction to physics of nanoplasmonics

Nanoplasmonics is the study of optical phenomena in nanoscale vicinity of metal surfaces [1]. At first look, this definition may be counterintuitive because, accordingly with the well-known concept of diffraction limit, an optical field associated with visible light cannot be confined or localized to a region whose size is less than half the light wavelength. [2]. However, because the nanoparticles dimensions are less than the metal's skin depth, i.e. how deeply the optical radiation penetrates the metal, corresponding to the smaller electromagnetic length scale, it is the size of nanoparticles that defines the spatial scale of the optical energy localization [3]. Since the skin depth is roughly 25 nm for coinage metals, copper, and alkaline metals over the whole optical and most of IR region, this size represent the upper limit for the observation of light confinement on the nanoscale [2]. On the other end, the nanoparticles should not be smaller than the so-called nonlocality length l_{nl}, i.e. the distance that an electron with Fermi velocity v_f ~$2x10^6$ m/s moves during one optical oscillation [4]. Since an half a period is about a femtosecond, that nonlocality length is 2 nm. Thus nanoplasmonic phenomena unfold on a characteristic length scale between 2 and 20 nm [2].

To first approssimation, the conduction electrons of the metal nanoparticle can be modeled as a Drude's gas, they move freely and, driven by external light's dielectric field, are periodically displaced with respect to the fixed ionic cores [5]. The displacement creates charges at opposite surfaces. Because those charges attract each other, there also exists a restoring force, allowing for a resonance to occur at a specific frequency, i.e. the particle dipole plasmon frequency, where the response of the electrons shows a $\pi/2$ phase lag with respect to the driving field [6] The quantum of this charge density oscillation is called a localized surface plasmon polariton (LSPP) [6]. Thus, a resonantly enhanced field builds up inside the particle, which in the small particle limit is homogeneous throughout its volume, producing a dipolar field outside the particle. This leads to enhanced absorption and scattering cross sections for electromagnetic waves, as well as to a strongly enhanced near field in the immediate vicinity of the particle surface [7].

1.1.1 Mie theory for light scattering by a spherical particle

In the early 20th century, Gustav Mie developed an analytical solution to Maxwell's equations that describes the scattering and absorption of light by spherical particles. For very small particles (d << λ), Mie scattering agrees with the more familiar Rayleigh scattering [8]. Finding the scattered fields produced by a plane wave incident on a homogeneous conducting sphere results in the following total scattering, extinction, and absorption cross-sections [9]:

$$\sigma_{sca} = \frac{2\pi}{|k|^2}\sum_{L=1}^{\infty}(2L+1)\left(|a_L|^2 + |b_L|^2\right) \qquad Eq.1$$

$$\sigma_{sca} = \frac{2\pi}{|k|^2}\sum_{L=1}^{\infty}(2L+1)[R_e(a_L + b_L)] \qquad Eq.2$$

$$\sigma_{abs} = \sigma_{ext} + \sigma_{sca} \qquad Eq.3$$

where k is the incoming wavevector and L are integers representing the dipole, quadrupole, and higher multipoles of the scattering. In the above expressions, a_L and b_L are the following parameters, composed of the Riccati-Bessel functions ψ_L and χ_L [10]:

$$a_L = \frac{m\psi_L(mx)\psi_L'(x) - \psi_L'(mx)\psi_L(x)}{m\psi_L(mx)\chi_L'(x) - \psi_L'(mx)\chi_L(x)} \qquad Eq.4$$

$$b_L = \frac{\psi_L(mx)\psi_L'(x) - m\psi_L'(mx)\psi_L(x)}{\psi_L(mx)\chi_L'(x) - m\psi_L'(mx)\chi_L(x)} \qquad Eq.5$$

Here, $m = \tilde{n}/n_m$, where $\tilde{n} = n_R + in_I$ is the complex refractive index of the metal, and n_m is the real refractive index of the surrounding medium. Also, $x = k_m r$, where r is the radius of the particle.
If the nanoparticle is assumed to be very small as compared to the wavelength, x << λ. In this case, accordingly to approssimation by Bohren and Hoffmann [9], the Riccati-Bessel functions can be approximated by power series:

$$a_l \approx -\frac{i2x^3}{3}\frac{m^2-1}{m^2+2} \qquad Eq.6$$

$$b_l \approx 0 \qquad Eq.7$$

and the higher order a_L and b_L are zero (again, only when keeping terms up to x^3). To find the real part of a_1 as required in Eq. 2, substitute $m = (n_R + in_I)/n_m$ into Eq. 6:

$$a_l \approx -\frac{i2x^3}{3}\frac{n_R^2 - n_I^2 + i2n_R n_I - n_m^2}{n_R^2 - n_I^2 + i2n_R n_I + n_m^2} \qquad Eq.8$$

Next, switch to the complex metal dielectric function $\tilde{\varepsilon} = \varepsilon_1 + i\varepsilon_2$ with the following relations:

$$\varepsilon_1 = n_R^2 - n_I^2 \qquad Eq.9$$

$$\varepsilon_2 = 2n_R n_I \qquad Eq.10$$

and switch to the medium's dielectric function: $\varepsilon_m = n_m^2$.
These substitutions lead to:

$$a_l = \frac{2x^3}{3}\frac{-i\varepsilon_i^2 - i\varepsilon_l\varepsilon_m + 3\varepsilon_2\varepsilon_m - i\varepsilon_2^2 + i2\varepsilon_m^2}{(\varepsilon_1 + 2\varepsilon_m)^2 + (\varepsilon_2)^2} \qquad Eq.11$$

Substitution of Eq. 11 into Eq. 2 and taking the dipole term only yields the widely quoted expression for nanoparticle plasmon resonances:

$$\sigma_{ext} = \frac{18\pi\varepsilon_m^{3/2}V}{\lambda}\frac{\varepsilon_2(\lambda)}{[\varepsilon_1(\lambda) + 2\varepsilon_m]^2 + \varepsilon_2(\lambda)^2} \qquad Eq.12$$

$$\sigma_{sca} = \frac{32\pi^4\varepsilon_m^2V^2}{\lambda^4}\frac{(\varepsilon_i - \varepsilon_m)^2 + (\varepsilon_2)^2}{[\varepsilon_1(\lambda) + 2\varepsilon_m]^2 + \varepsilon_2(\lambda)^2} \qquad Eq.13$$

According to Eq. 13, the extinction cross-section will be maximized when the condition $\varepsilon_1 = -2\varepsilon_m$ is fulfilled. This explains the dependence of the LSPR extinction peak on the surrounding dielectric environment.

1.1.2 Gans theory for light scattering by non-spherical particle

In cases of nonspherical nanoparticles, the extension of the Mie theory, that is, the Gans theory, is applicable. This theory provides the scattering characteristics for both oblate and prolate spheroidal nanoparticles describing the absorption cross-section for a prolate spheroid as [11]

$$\sigma_{abs} = \frac{\omega}{3c}\varepsilon_m^{3/2} V \sum_j \frac{\left(\frac{1}{P_j^2}\right)\varepsilon_2}{\left[\varepsilon_1 + \left\{\frac{1-P_j}{P_j}\right\}\varepsilon_m\right]^2 + \varepsilon_2^2} \qquad Eq.14$$

where j represents the three dimensions of the particle and P_j includes P_A, P_B, and P_C, termed depolarization factors, for each axis of the prolate spheroid particle.
The depolarization factors anisotropically alter the values of ε_1 and ε_2, and the resulting LSPR peak frequencies are represented as

$$P_A = \frac{1-e^2}{e^2}\left[\frac{1}{2e}\ln\left(\frac{1+e}{1-e}\right) - 1\right] \qquad Eq.15$$

$$P_B = P_C = \frac{1-P_A}{2} \qquad Eq.16$$

where e is the following factor, including the aspect ratio R of the particle [12]

$$e = \left[1 - \left(\frac{B}{A}\right)^2\right]^{\frac{1}{2}} = \left(1 - \frac{1}{R^2}\right)^{\frac{1}{2}} \qquad Eq.17$$

The extinction spectrum resulting from Eq.14 has two peaks, one corresponding to the transverse plasmon peak from the contributions of the x- and y-axes to the sum, and the other corresponding to the longitudinal plasmon peak from the z-axis contribution. Equation 14 also provides an intuitive understanding of the effects of aspect ratio on LSPR peak wavelength. Factor ε_m, which is 2 for spherical particles, is $\left(\frac{1-P_j}{P_j}\right)$, a quantity that increases with aspect ratio and can be much greater than 2. This leads to a red shift of the plasmon peak with increasing aspect ratio, as well as increased sensitivity to the dielectric constant of the surrounding medium [13].

1.1.3 Local Refractive Index Dependence of Plasmon Resonance Spectra

To find the functional form of the LSPR peak wavelength's dependence on the dielectric function of the medium, one can use the analytical, frequency-dependent form for ε_1 from the Drude model of the electronic structure of metals [14]:

$$\varepsilon_1 = 1 - \frac{\omega_P^2}{\omega^2 + \gamma^2} \quad Eq.18$$

where ω_p is the plasma frequency and γ is the damping parameter of the bulk metal.
For visible and near infrared frequencies, $\gamma << \omega_p$ so the above can be simplified to:

$$\varepsilon_1 = 1 - \frac{\omega_P^2}{\omega^2} \quad Eq.19$$

Using this expression for ε_1 and setting $\varepsilon_1 = -2\varepsilon_m$ (the resonance condition), one obtains the following:

$$\omega_{\max} = \frac{\omega_P}{\sqrt{2\varepsilon_m + 1}} \quad Eq.20$$

Where ω_{max} is the LSPR peak frequency. Converting from frequency to wavelength via $\lambda = 2\pi c/\omega$, and then from dielectric constant to index of refraction via $\varepsilon_m = n^2$, the Eq. 20 becomes:

$$\lambda_{\max} = \lambda_P \sqrt{2n_m^2 + 1} \quad Eq.21$$

where λ_{max} is the LSPR peak wavelength and λ_p is the wavelength corresponding to the plasma frequency of the bulk metal. Note that neither the LSPR peak frequency/energy nor wavelength is strictly linear with refractive index, but both are approximately linear over small ranges of n.

1.2 Parameters affecting nanoparticles plasmonic properties

In general, the spectral position, damping, and strength of the dipole as well as of the higher-order plasmon resonances of metal nanoparticles depend on the particle material, size, geometry, and the dielectric function of the surrounding host [15]. This section introduces several of these fundamental relationships and explain how these can impact nanoparticles optical properties.

1.2.1 Size Effect

The nanoparticle size has two different impacts on the plasmon, (i) if the nanoparticle is small enough (less than 20 nm for gold), the intrinsic effect of the particle directly affect the metal permittivity $\varepsilon(\omega, R)$ [16]; (ii) if the particle is not small enough (larger than 25 nm for gold), the extrinsic effect is enabled, where the extinction coefficient is dependent on the size r [17]. Figure 1 shows the intrinsic and extrinsic effects for gold spherical nanoparticles.

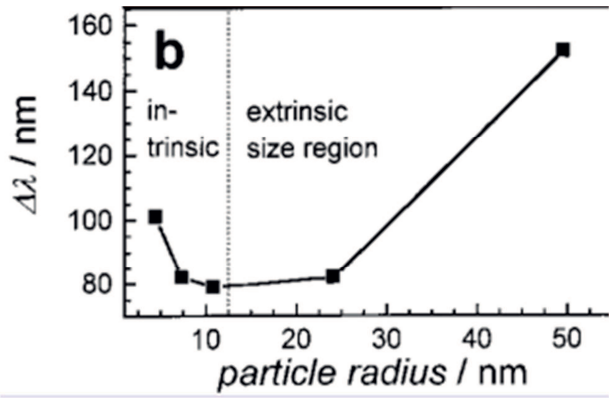

Figure 1. Size effect on the plasmon bandwidth of spherical gold nanoparticles [17].

The reason for the dipole plasmon wavelength changes with the size of nanoparticles can be found in the damping constant in the Drude model in Eq. 18 that is dependent on the particle size [18]:

$$\gamma(r) = \gamma_0 + \frac{Av_F}{r} \qquad Eq.\ 22$$

where γ_0 is the bulk damping constant, v_F is the velocity of the electrons at the Fermi energy, and A is a theory-dependent parameter that includes details of the scattering process (e.g., isotropic or diffuse scattering). Accordingly to this, when the size of the nanoparticles increase, the free electrons redistributes between the particle surface and bulk phase, leading to the plasmon wavelength red-shifts, the resonant peak broadens and extinction efficiency increases [19].

Figures 2 (a) and (b) show extinction spectrum of a nanospheres in vacuum for two different sizes of 30 and 60 nm, respectively, calculated using Mie theory [20]. For smaller nanospheres, only one peak is observed which is due to the dipole surface plasmon resonance. However, larger nanospheres present two peaks in the plasmon resonance where the first one, which occurs in the UV range, is due to the quadrupole plasmon resonance.

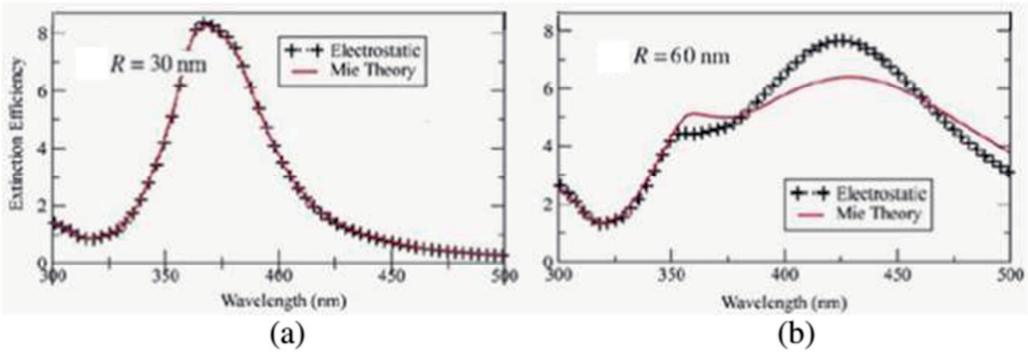

Figure 2. Extinction efficiency for a silver sphere of diameter (a)30 nm and (b) 60 nm [20]

1.2.2 Aspect Ratio Effect

Nanoparticles' aspect ratio increase results in a red shift of extinction spectra due to an greater charge separation, whereas increased symmetry results in increases in LSPR signal intensity [21]. Since the number of modes in which a given nanoparticle can be polarized determines the resonance absorption peaks, thus, nonspherical nanoparticles tend to exhibit multiple red-shifted peaks compared to nanospheres.

Deviations in aspect ratio are more influential on the spectral shift of the LSPR signal than are changes in size. For example, changing the size from 10 to 100 nm for nanospheres results in a red shift of 47 nm; in contrast, changing the aspect ratio from 2 to 3 for nanorods results in a red shift of 92 nm for a longitudinal peak [22] (see Figure 3). This example shows that changes in aspect ratio correlate with much smaller changes in the overall size of the nanoparticles.

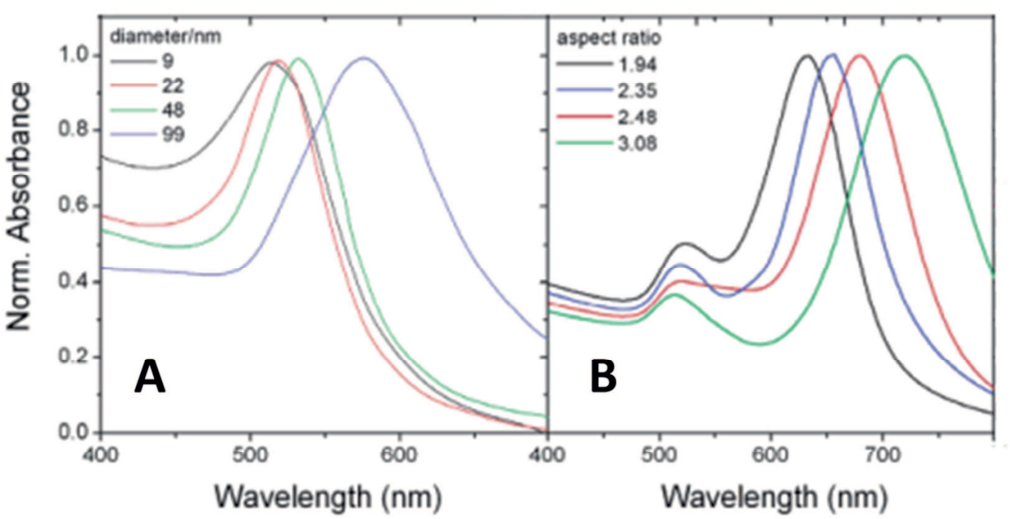

Figure 3. Experimental spectra for (A) Au spheres with different diameters, (B) Au nanorods with different aspect ratio [22].

Furthermore, the effects of the aspect ratio increasing on plasmon peak wavelength depends on the orientation of nanoparticle major axis with respect to the polarization direction. Finite-difference time-domain (FDTD) modeling of an elongated rhombus in Figure 4(A) for fixed minor axis diameter of b = 100nm, particle thickness of h = 50 nm, and various major axis diameter of a = 100-200nm, demonstrates that dipolar plasmons are enhanced by increasing the aspect ratio when the particle elongation is along the polarization direction. However, Figure 4(B) shows that quadrupole extinction cross sections become more important by increasing the aspect ratio when the particle elongation is normal to the polarization direction. This is valid for particles with similar major axis diameter and particle thickness but larger minor axis of b = 200 nm [23].

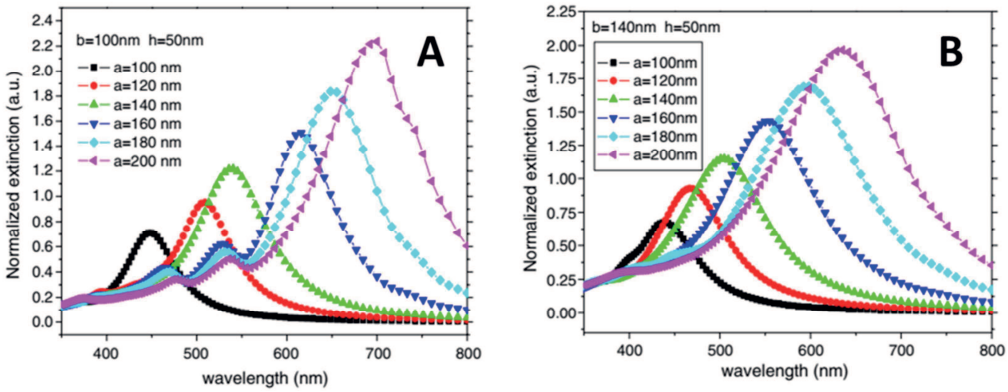

Figure 4. The effect of aspect ratio on dipolar and quadrupolar extinction cross section for elongated nanorhombuses (A) along the polarization direction, (B) normal to the polarization direction [23].

1.2.3 Material Effect

The most common metals used in LSPR applications are gold (Au) and silver (Ag) [24]. Gold is often chosen because of its chemical stability and resistance to oxidation [25], but silver has sharper resonances and higher refractive index sensitivity [26]. A comparison of gold and silver nanoparticles of similar size and shape highlights this fact. For example, for spheres 50-60 nm in diameter, the refractive index sensitivity is 60 nm/ RIU for a plasmon resonance at ~ 530 nm for gold [27] and 160 nm/RIU for a plasmon resonance at ~ 435 nm for silver [28]. As another example, for nanocubes 30-50 nm in size, the refractive index sensitivity is 83nm/RIU for a plasmon resonance at 538 nm for gold [29] and 146 nm/RIU for a plasmon resonance at 510 nm for silver [30].

The reason for the differences in plasmon resonance frequency and refractive index sensitivity lies in the dielectric functions of the two metals [31]. In particular, the resonance frequency depends on the real part of the permittivity, and resonance line width or spectrum flatness on its imaginary part. Thus, the smaller the real part of the permittivity is, the higher the plasmon frequency becomes and the higher the interband threshold is, the sharper the spectrum becomes, leading to a higher refractive index sensitivity [31]. Indeed, the real dielectric function of silver varies with wavelength more than that of gold over the visible light region, especially in the 400-600 nm region where the

plasmon resonance lies for reasonable values of the dielectric constant of the medium (Figure 5A). Moreover, the imaginary part of the dielectric function of silver is less than that of gold across the visible region, less plasmon damping occurs, resulting in higher scattering efficiency and narrower plasmon linewidths (Figure 5B).

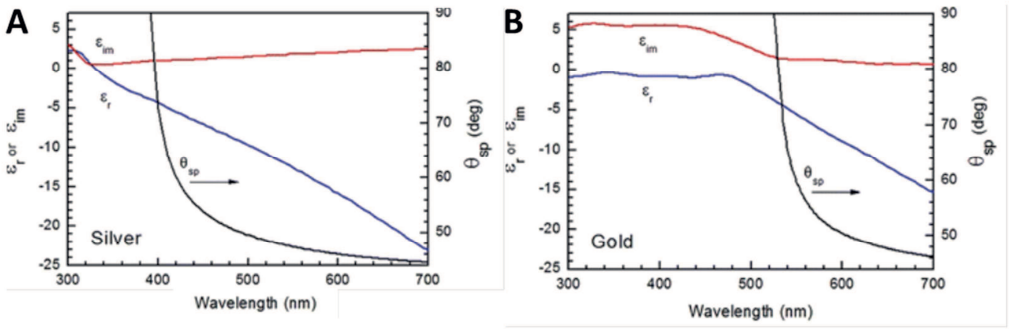

Figure 5. Real and imaginary parts of the complex dielectric functions for silver (A) and gold (B) [32].

Therefore, the use of silver nanoparticles offers a significant advantage in practical sensing applications. For example, for silver and gold nanoparticles with similar refractive index sensitivities, the silver particles are more desirable because they provide a stronger and sharper plasmon resonance curve whose peak wavelength can be more accurately determined.

1.2.4 Interparticle distance effect for nanoparticles' array

In nanoparticles' arrays, each nanoparticle with a diameter much smaller than the wavelength of the exciting light acts as an electric dipole [7]. Thus, two types of electromagnetic interactions between the particles can be distinguished, depending on the spacing *d* between adjacent nanoparticles. For particle spacings on the order of the exciting wavelength far-field dipolar interactions with a d^{-1} dependence dominate. Figures 6 shows an example of the dependence of both extinction peak position and width on the grating constant d for a regular square array of 150-nm-diameter Au nanoparticles [33]. Such variations can be explained by assuming far-field dipolar interactions—the ensemble acts effectively as a grating, leading to increased radiation damping of the collective resonances for grating constants where grating orders change from evanescent to radiative in character [34].

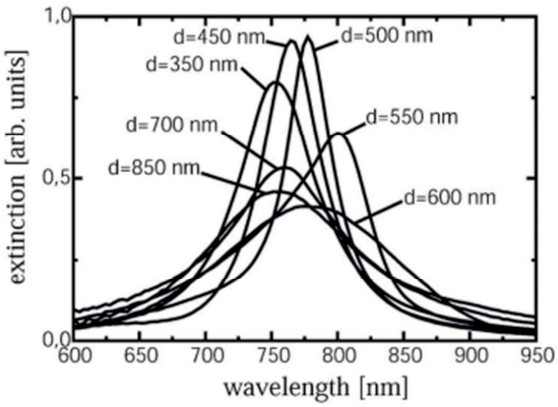

Figure 6. Measured extinction spectrum for regular two dimensional (2D) square arrays of Au nanoparticles for different interparticle distances [33].

For particle spacings much smaller than the wavelength of light, near-field dipolar interactions between adjacent particles with a distance dependence of d^{-3} dominate [35]. These strongly distance-dependent interactions lead to a splitting of the plasmon dipolar peak for regular one-dimensional arrays of metal nanoparticles as seen in Figure 7 for ordered arrays of 50-nm Au particles [33].

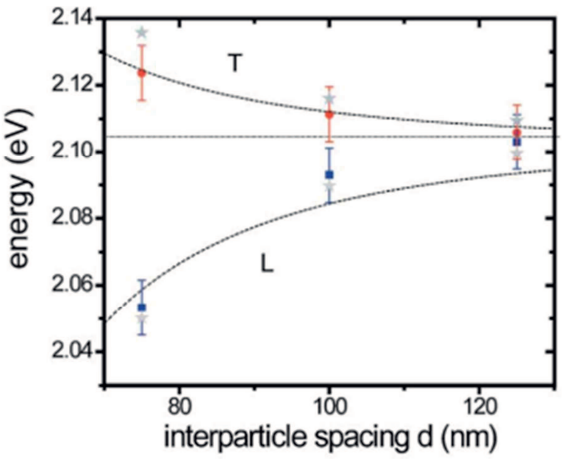

Figure 7. Measured spectral position of the collective plasmon resonances of one dimensional arrays of closely spaced Au nanoparticles for longitudinal (L)and transverse polarizations (T) [33].

Localized plasmon excitations mediated by particle interactions also occur in randomly nanostructured metallic surfaces but, in this case, for average spacing larger than 200 nm, no inter-particle coupling between neighboring nanoparticles was observed [36].

1.2.5 Substrate effects

Nanoparticles are often produced on surfaces, so it is important to understand how their interaction with the substrate influences their plasmon resonance properties [20]. Moreover, experimental findings demonstrate that LSPR frequency depends not only on the dielectric properties of the local environment that surrounds the nanoparticles but also on the substrate, on which the particles are supported [37].

Figure 9 displays a collection of extinction spectra for Ag nanoparticles fabricated with aspect ratio 4:1 (width: height) on the following substrates: fused silica (n =1.46), borosilicate glass (n =1.52), mica (n =1.6), and SF-10 (n=1.73). In Figure 8, λ_{max} systematically shifts to the red from 611 nm for nanoparticles on fused silica, the substrate with the lowest refractive index, to 634 nm for nanoparticles on SF-10, the substrate with the highest refractive index [38].

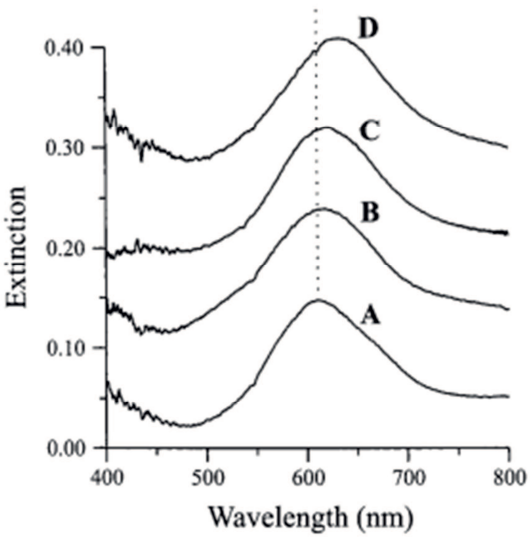

Figure 8. UV-vis extinction spectra of Ag nanoparticles on various substrates in a N_2 environment. All nanoparticles were fabricated using D = 400 nm nanospheres and d_m = 25 nm. (A) Fused silica (n =1.46); λ_{max} = 611 nm. (B) Borosilicate optical glass (n = 1.52); λ_{max} =616 nm. (C) Mica (n =1.6); λ_{max} = 622 nm. (D) SF-10 (n =1.73); λ_{max} =635 nm [38].

Furthermore, it has been demonstrated that the substrate also affects the sensing performance of the LSPR sensor, leading to a significantly decrease of bulk sensitivity with respect to the unsupported nanoparticles [39]. However no systematic correlation between the measured sensitivity factor and $n_{substrate}$ has been observed [38]. In this regard, Figure 9 shows a plot of extinction peak shift, $\Delta\lambda_{max} = \lambda_{max}(solvent) - \lambda_{max}(N_2)$ versus $n_{external}$ for each of the above mentioned Ag nanospheres on four different substrates.

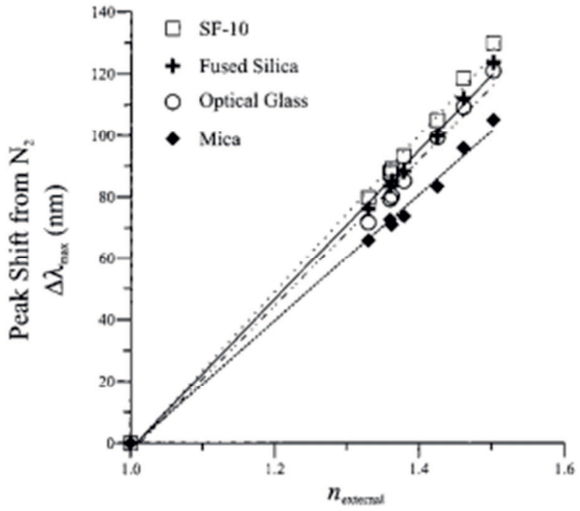

Figure 9. Figure 6. LSPR peak shift from N_2, $\Delta\lambda_{max} = \lambda_{max}(solvent) - \lambda_{max}(N_2)$ versus the refractive index of the solvent, $n_{external}$, for each of the four substrates [38].

In order to quantitatively evaluate the effect of the substrate on the refractive index sensitivity Discrete Dipole Approximation (DDA) calculation has been performed for a 10 nm sphere surrounded by a mica shell simulating the substrate (Figure 10). The results showed that as the sphere becomes more imbedded, the LSPR wavelength shifts to the red approximately linear with exposed area. Therefore, it has been concluded that the decrease of sensitivity for supported nanoparticles compared with unsupported ones can be attributed to the lower fraction of the surface area is exposed to solvent than to the substrate [38].

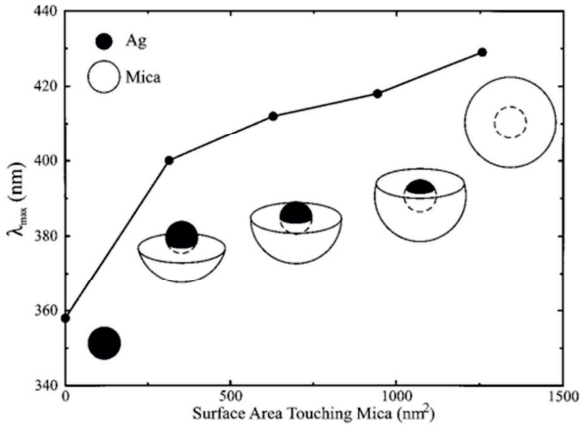

Figure 10. DDA results showing LSPR wavelength as a function of particle area in contact with substrate. The DDA calculations are for a Ag core of radius 10 nm and a partial mica shell of radius 30 nm. Degree of embedding is changed by truncating the mica shell at z = -5, 0, and 5 nm, along an axis where the origin is the center of the sphere, as depicted [38].

1.3 Hardware setup of LSPR

1.3.1 Preparation of nanostructures

Nanostructured substrates employed in the nanoplasmonic biosensors can be divided in those based on top-down or bottom up fabrication methodologies [40]. While the former group relies on lithographical patterning techniques, the latter one is based on chemically synthesized colloidal nanoparticles that are further deposited on substrates.

Both fabrication principles have advantages and disadvantages. In the case of wet chemistry methods, precise geometrical nanoparticle engineering is readily achievable leading to a fine tuning of LSPR wavelength [41], however the main drawbacks are with respect to polydispersity and reproducibility [42]. On the other side, lithographic techniques allowing uniformity in size and shape of metal nanostructures, are usually slow and high-cost, and despite high levels of resolution, typically limit the patterning area to only a few μm^2 [43].

A different approach for large-scale and low-cost creation of plasmonic nanostructures is offered by colloidal lithography techniques, such as nanospheres lithography (NSL) [44], or hole-mask colloidal lithography (HCL) [45]. Herein, we only point out the basics of the latter one fabrication method.

The basic steps of hole mask lithography are shown in Figure 11 [46].

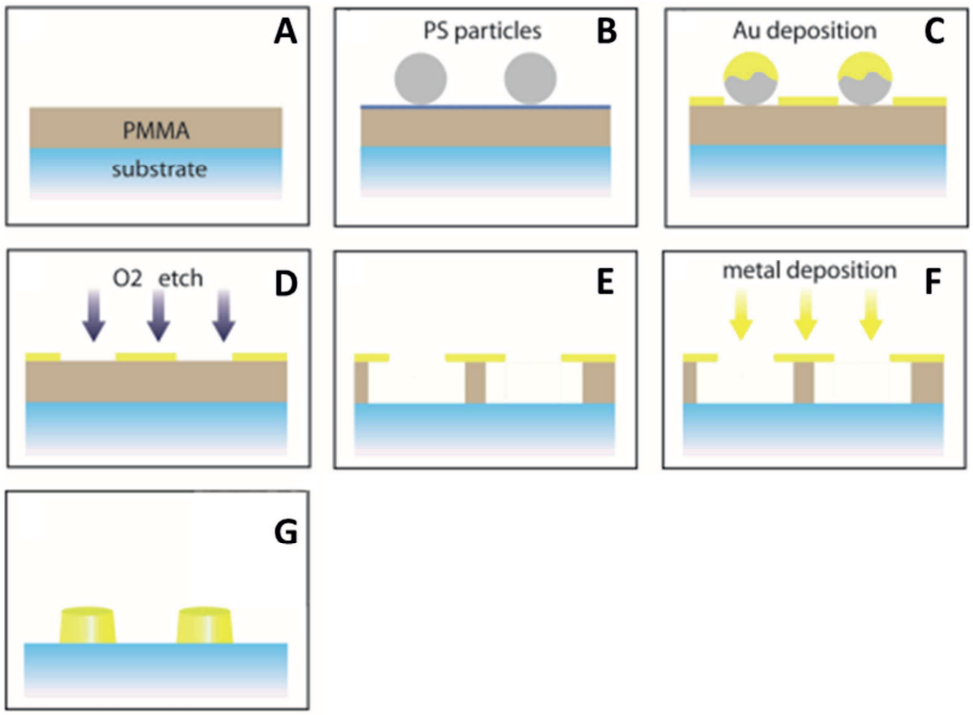

Figure 11. The steps involved in fabrication of HCL samples [46].

First a sacrificial layer of poly methyl methacrylate (PMMA) is spin coated on the surface of a piranha cleaned glass slide. Figure 11 A. The substrate is then soft-baked for 10 minutes in the oven at 180 °C. The resulting layer of PMMA depends on the weight percent and the spin speed. The substrate is then oxygen etched for 5s (plasma batch top) to decrease the hydrophobicity of the PMMA surface and allow for wetting with water. Negatively charged poly-(diallyldimethyammonium) chloride (PDDA), is applied on the surface in order to attract the positively charged polystyrene particles (PS). The final size of the nanostructure is defined by the PS particles. As shown in Figure 11 B-F, after the colloid particles have been adsorbed on the surface, a 10 nm layer of metal is evaporated on the PS covered surface to form a mask. The metal covered PS particles are then removed by tape stripping. The subsequent O_2 plasma etching will create holes in the PMMA. The metal nanostructures are formed through metal deposition inside the hole. In the simplest case of materials evaporation normal to the surface, the described procedure results in a surface structured with circular nanodisks. The HCL substrate is completed by dissolving the sacrificial layer in the final liftoff process, Figure 11 B-F. The O_2 plasma etching creates undercuts in the PMMA layers so that the liftoff step can remove the whole resist layer with ease.

Colloidal lithography, such as HCL described above, can produce homogenous substrates in cm^2 size with up to 40 % surface coverage [47]. The HCL structures are short range ordered and relies only on the colloidal particle charge repulsion for self-assembly. Therefore the surface interparticle distance is relatively fixed [48]. By introducing ions to screen the particle-particle charge repulsion, the interparticle distance can be slightly reduced [46].

The biggest disadvantage of HCL, or any other colloidal lithography technique, is the limited range of nanostructure shapes that can be produced. The shapes of the nanostructures are defined by the size and shape of the colloidal particle, which have spherical shape. However, playing with angled evaporations, angled etching, or using various shadow effects created by the mask, it is possible to produce ellipsoids, cones, crescent, rings, triangles and dimers etc [47].

1.3.2 Instrumental setup for LSPR spectroscopy

The most common optical geometries that are employed within LSPR sensors are transmission [49] and reflection [50]. These optical geometries are illustrated in Figure 12 [51].

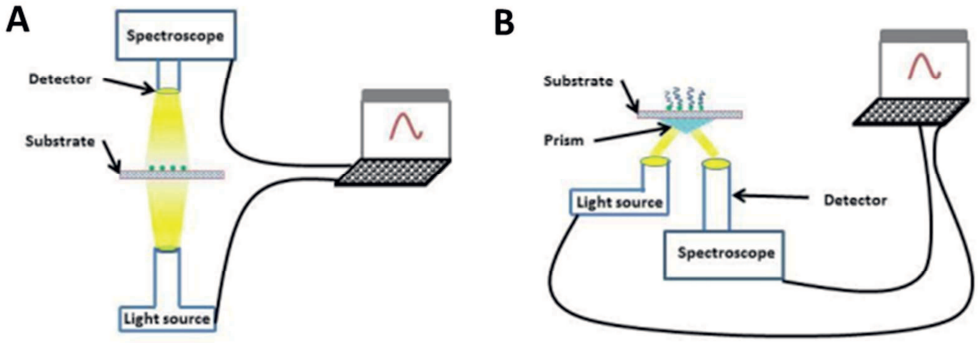

Figure 12. Diagrams of transmission (A) and reflection (B) geometries for LSPR spectroscopy measurement [51].

However, the trasmission-mode spectroscopy offers the following practical advantages:

- Instrumental requirement are small consisting of three major parts: an halogen lamp as light source exiting LSPR of the nanostructures, a measurement chamber (equipped with compatible microfluidics for measurements in liquid) holding the nanostructured substrate and spectrometer collecting the transmitted light, are all that is needed [52].
- Simple optical configuration i.e. no bulky optics are required allowing the miniaturization of the sensor devices, an aspects that expand the possibilities of LSPR-based devices to become truly integrated LOC platforms [53].
- The collinear setup rules out issues related with sample misalignment or tilt compared with reflection geometry. Furthermore, since the nanoparticles can be excited from virtually any angle, no special geometry are required [54].
- The plasmon peaks in reflection transmission are narrower and with a higher intensity than the corresponding reflection spectra, increasing the accuracy in peak determination [55].

1.4 Localized Surface Plasmon Resonance Sensing

Whereas the above section is focused on the instrumental setup necessary to perform LSPR experiments, the present one briefly discuss the principle of the most common LSPR sensing mode i.e. the wavelength-shift measurement, in which the change in the maximum of the LSPR trasmission spectra is monitored as a function of changes in the local dielectric environment caused by analyte adsorption [56]. Furthermore, we discuss about the sensing performance of refractometric LSPR biosensors and how signal analysis methods can improve the sensitivity of the techniques.

1.4.1 Localized Surface Plasmon Resonance Wavelength-Shift Sensing

LSPR refractometric sensing is based on RI changes, caused by analyte adsorption in the vicinity of the plasmonic metal particle. The sensitivity to the environment is provided by the evanescent nature of the plasmon electric field, extending from the metal particle into the surrounding medium [57]. For RI changes to produce a measurable shift in the resonance, they must occur in a region of appreciable field intensity [58]. To a good approximation the plasmon field decays exponentially with the distance from the particle's surface, and hence effective sensing is limited to a typical range of tens of nanometers, a region termed the sensing volume [59]. The common case of sensing of adsorbed analyte layers on plasmonic particles is effectively a core−shell system (metal core−dielectric shell). While a rigorous core−shell approach is more accurate, it was found that the response of an LSPR transducer to layer adsorption can be described by a simple phenomenological equation [58]

$$\Delta\lambda_{LSPR} = m\Delta n\left(1 - e^{-\frac{d}{l_d}}\right) \qquad Eq.\ 23$$

where $\Delta\lambda_{LSPR}$ is the plasmon peak shift, *m* is the refractive index sensitivity (RIS), a parameter characteristic of the specific transducer, Δ*n* is the difference in the RI between the adsorbed layer and the medium it displaced (e.g., air, water), *d* is the layer thickness, and l_d is the plasmon decay length, also a parameter characteristic of the specific transducer. The RIS can be easily determined by measuring the LSPR spectrum in bulk solvents of different RI values [60]; accordingly with the effectively infinite layer thickness approximation over a short range of RI Eq.23 can be simplifies to the linear relation $\Delta\lambda_{LSPR} = m\Delta n$, and *m* is easily extracted as the slope of $\Delta\lambda_{LSPR}$ versus Δ*n* curve [28]. It is to note that over wide RI range, the response to bulk RI change often displays a clear nonlinearity as discussed in the section 2.1.3.

An LSPR transducer is commonly coated with a recognition interface, a layer which selectively adsorbs a desired analyte, to afford specificity; the equation for this case is then [61]:

$$\Delta\lambda_{LSPR} = m\Delta n e^{-\frac{d_1}{l_d}}\left(1 - e^{-\frac{d_2}{l_d}}\right) \qquad Eq.\ 24$$

where d_1 and d_2 are the thicknesses of the recognition interface and analyte layer, respectively, and Δ*n* is assumed to be the same for both layers. Equation 24 implies that no single value of l_d will produce a maximal response but that its value must be selected based on the thicknesses d_1 and d_2. For effective sensing, the plasmon field must encompass a large enough volume to include the region of space where analyte binding takes place. However, for a relatively large field and thin analyte, adsorption of the analyte will effect an RI change in only a small fraction of the sensing volume. Because the particle's LSPR is sensitive to the RI of the entire sensing volume, this will result in only a

small change in the resonance [61]. Therefore for optimal performance, a transducer with appropriate decay length for a given application must be selected.

1.4.2 Performance quantification for refractometric LSPR biosensors

The ability with which metal nanostructures can detect RI changes is generally expressed in terms of their bulk sensitivity *m* that is, the linear dependence of resonance wavelength λ_{LSPR} on the homogeneous bulk RI changes of the dielectric environment as discussed above. Next to *m*, a second property that strongly influences the sensing performance is the ability with which these spectral shifts can be discriminated, something that is normally taken into account by considering the full-width-half-maximum (Γ) of the resonance peak. Both quantities are often combined in a generalized performance-assessing figure-of-merit (*FOM*) parameter, defined as [62]:

$$FOM = \frac{m}{\Gamma} \qquad Eq.\,25$$

Since both *m* and *FOM* depend critically on the spectral features of the metal nanoparticles employed as sensing elements, thus all the parameters affecting nanoparticles optical properties (see section 2.2), also influence the sensing performance of the LSPR sensor. In particular, in recent years, several works have focused on the effects of particle shape on the sensitivity of nanoplasmonic particles showing that nanostructures with a higher aspect ratio provide higher FOMs [63]. This effect has been demonstrated to be due to red shift of plasmon resonance frequency for elongated nanoparticles with respect to spherical ones [63]. Indeed, the gold nanospheres shows a strongly blue shifted LSPR (λ_{LSPR} < 600 nm) resulting in a spectral overlap with the interband transition of gold [64]. Therefore, the corresponding LSPR peak is wider than 100 nm leading to a low value of FOM [64]. In contrast, a much better sensing performance is obtained when rod-shaped nanostructures are considered [12]. For these particles, red-shifting of their plasmon resonance distances their LSPR from the interband transitions of the employed plasmonic material leading to narrower peak [12]. The resulting *FOM* for nanorods is of about an order of magnitude larger than those corresponding to nanospheres [65].

1.4.3 Improving the instrumental resolution of LSPR technique by using spectral data analysis algorithms

In the previous section, the sensitivity of LSPR has been presented as proportional to the magnitude of plasmon peak shift upon variations in bulk or interfacial RI variation. However, equally important is the ability to precisely and accurately measure the spectral shift that results from the sample. Therefore, it is necessary to introduce the another sensitivity parameter, i.e. called sensor resolution, which characterizes the smallest possible spectral shift that can be accurately measured [66]. This term takes into account the spectral resolution of the system and a number of noise parameters. Both quantity depends critically by the methodology used for the measuring the spectral shift in response

to a sample [67]. One simple method to monitor the spectral shift is to track the position of the extremum (i.e., minimum or maximum, depending on the measurement configuration) [67]. The total sensor response is the spectral difference between the final and initial extrema, as illustrated in Figure 13.

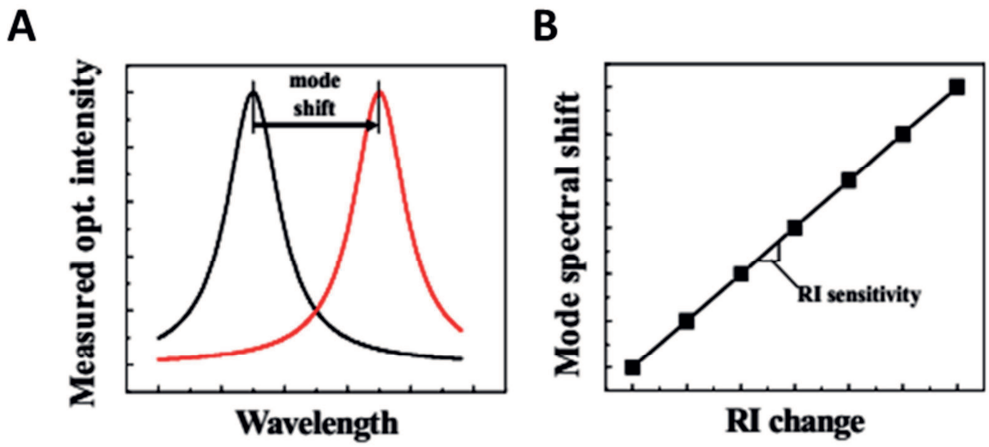

Figure 13. (A). Optical RI sensors typically utilize an optical resonance that has a resonant wavelength dependent upon the RI of the sample. When the sample RI changes, the mode shifts spectrally. (B). The RI sensitivity is determined by measuring the spectral shift of the resonant mode for known changes in sample RI.

Spectrophotometers with double-beam configuration provides high-wavelength resolution (~0.5 nm) [68] good compensation for variations in light source intensity, and typical noise levels in extinction of $\sim 1 \times 10^{-4}$ Abs; however, the data acquisition in terms of full spectra is slow (minutes for the visible region) [69]. Hence, this mode of analysis does not allow temporal variations in the peak position to be followed when recording rapid binding kinetics and is, thus, limited to temporal variations in extinction in a narrow wavelength region. In contrast, pixel array spectrophotometers with fixed gratings can easily provide full-spectrum acquisition in the millisecond range [70], but they suffer, instead, from poorer wavelength resolution (~4 nm) and generally significantly higher noise in the individual pixel values [70]. However, wavelength accuracy is of less concern when recording relative temporal variations, and since the complete spectrum is generated simultaneously in pixel array detectors, they provide the possibility of using averaging and curve-fitting procedures to reduce noise [71]. In the following, a simple and fast tracking algorithms yielding a peak position precision of $<5 \times 10^{-4}$ nm and an extinction noise level of $<5 \times 10^{-6}$ absorbance units (Abs) is briefly illustrated according to the literature [72]. This, in order to demonstrated that LSPR technique is readily able to achieve a S/N of ~2000 (equivalent to a detection limit of <0.1 ng/cm^2) for typical protein binding reactions [73].

Peak position tracking algorithm is based on calculating the centroid (center of mass) of the peak, it is evaluated on either discrete spectral data ε (λ, t) or on a high-degree polynomial fit to the data [72],

$$\varepsilon_{fit}(\lambda,t)=\sum_{i=0}^{n} p_{i+1}\lambda_i \qquad Eq.26$$

where *n* is the degree of the polynomial and *p* is a vector containing the parameters defining the polynomial. With a value of *n* = 20, 1 - R^2 was < 10^{-5} and was not improved by higher-degree polynomials.

Furthermore, it was found that the centroid method providing the lowest noise was a variant of the interpolated tracking centroid algorithm [74], in which a constant wavelength span (S) defines the region of the peak to be included in each centroid calculation. In the presented method, the wavelength span, S, is fitted to $\varepsilon_{fit}(\lambda)$ by solving the equation $\varepsilon_{fit}(\lambda)-\varepsilon_{fit}(\lambda+S)=0$, providing the left point (λ_s) of an interval of length *S*, thus defining the region of the spectrum used to estimate the center of mass. Knowing λ_s, the baseline value (ε_{base}) is determined from $\varepsilon_{base}=\varepsilon_{fit}(\lambda_s)=\varepsilon_{fit}(\lambda_s+S)=0$. Finally, the centroid ($\lambda_{centroid}$) is defined and calculated from the polynomial expression [74]

$$\lambda_{centroid}(t)=\frac{\int_{\lambda_s}^{\lambda_s+S}\lambda\left(\varepsilon_{fit}(\lambda,t)-\varepsilon_{base}\right)d\lambda}{\int_{\lambda_s}^{\lambda_s+S}\left(\varepsilon_{fit}(\lambda,t)-\varepsilon_{base}\right)d\lambda}=\frac{\sum_{i=0}^{n}\left[\frac{p_i+1}{i+2}\left((\lambda_s+S)^{i+2}+{\lambda_s}^{i+1}\right)\right]-\frac{\varepsilon_{base}S}{2}(2\lambda_s+S)}{\sum_{i=0}^{n}\left[\frac{p_i+1}{i+2}\left((\lambda_s+S)^{i+2}+{\lambda_s}^{i+1}\right)\right]-\varepsilon_{base}S} \qquad Eq.27$$

Since LSPR peaks are often asymmetric, there will be an offset between the centroid value and the actual peak position [74]. However, a detailed comparison between changes in $\lambda_{centroid}(t)$ and changes in the actual peak shift $\Delta\lambda_{peak}$, defined by the sign change of the derivative of the polynomial) revealed that these parameters are seemingly perfectly linearly related with a proportionality constant always close to 1 [74].

1.5 References

1. M. I. Stockman. Nanoplasmonic sensing and detection. Science 348 (2015) 287-288.
2. M. I. Stockman. Nanoplasmonics: The physics behind the applications. Physics Today 64 (2011) 39-44.
3. M. I. Stockman. Nanoplasmonics: past, present, and glimpse into future. Optics Express 19 (2011) 22030- 22106.
4. Y. Luo, A. I. Fernandez-Dominguez, A. Wiener, S. A. Maier, J. B. Pendry. Surface Plasmons and Nonlocality: A Simple Model. Physical Review Letters 111 (2013) 093901-5.
5. M. B. Ross, C. A. Mirkin, G. C. Schatz. Optical Properties of One-, Two-, and Three-Dimensional Arrays of Plasmonic Nanostructures. J. Phys. Chem. C 120 (2016) 816−830.
6. J. M. Pitarke, V. M. Silkin, E. V. Chulkov, P. M. Echenique. Theory of surface plasmons and surface-plasmon polaritons. Rep. Prog. Phys. 70 (2007) 1–87.
7. S. A. Maier, H. A. Atwater. Plasmonics: Localization and guiding of electromagnetic energy in metal/dielectric structures. Journal of Applied Physics 98 (2005) 011101-10.
8. W. C. Mundy, J. A. Roux, A. M. Smith. Mie scattering by spheres in an absorbing medium. J. Opt. Soc. Am. 64 (1974) 1593-1597.
9. C. F. Bohren, D. R. Huffman. Absorption and Scattering of Light by Small Particles, 2nd ed.; Wiley-Interscience: New York, 1998.
10. H. Du. Mie-scattering calculation. Applied Optics 43 (2004) 1951-1956.
11. Y. Hong, Y. Huh, D. S. Yoon, J. Yang. Nanobiosensors Based on Localized Surface Plasmon Resonance for Biomarker Detection. Journal of Nanomaterials vol. 2012, Article ID 759830, 13 pages, 2012.
12. S. Link, M. B. Mohamed, and M. A. El-Sayed. Simulation of the optical absorption spectra of gold nanorods as a function of their aspect ratio and the effect of the medium dielectric constant. Journal of Physical Chemistry B 103 (1999) 3073–3077.
13. C. Tsai, K. Chang, C. Wu, P. Lee. The aspect ratio effect on plasmonic properties and biosensing of bonding mode in gold elliptical nanoring arrays. Optics Express 21 (2013) 14090-14096.
14. K.M. Mayer, J.H. Hafner. Localized surface plasmon resonance sensors. Chem. Rev. 111 (2011) 3828–3857.
15. E. Ringe, R. P. Van Duyne, L. D. Marks. Correlated structure-optical properties studies of plasmonic nanoparticles. Journal of Physics: Conference Series 522 (2014) 012006.

16. U. Kreibig, M. Vollmer. Optical Properties of Metal Clusters; Springer: Berlin, 1995.
17. S. Link, M. A. El-Sayed. Spectral Properties and Relaxation Dynamics of Surface Plasmon Electronic Oscillations in Gold and Silver Nanodots and Nanorods. J. Phys. Chem. B 103 (1999) 8410-8426.
18. J. R. Heath. Size-dependent surface-plasmon resonances of bare silver particles. Physical Review B 40 (1989) 9982-9985.
19. X. Zhou, M. Zhang, L. Yi, Y. Fu. Investigation of Resonance Modulation of a Single Rhombic Plasmonic Nanoparticle. Plasmonics 6 (2011) 91–98.
20. K. L. Kelly, E. Coronado, L. Zhao, G. C. Schatz. The Optical Properties of Metal Nanoparticles: The Influence of Size, Shape, and Dielectric Environment. J. Phys. Chem. B 107 (2003) 668-677.
21. X. Lu, M. Rycenga, S. E. Skrabalak, B. Wiley, Y. Xia. Chemical synthesis of novel plasmonic nanoparticles. Annual Review of Physical Chemistry 60 (2009) 167–192.
22. L. M. Liz-Marzán. Tailoring surface plasmons through the morphology and assembly of metal nanoparticles. Langmuir 22 (2006) 32–41.
23. E. Petryayeva, U. J. Krull. Localized surface plasmon resonance: Nanostructures, bioassays and biosensing—A review. Analytica Chimica Acta 706 (2011) 8–24.
24. K. M. Mayer, J. H. Hafner. Localized Surface Plasmon Resonance Sensors. Chem. Rev. 111 (2011) 3828–3857.
25. F. Vigneron, V. Caps. Evolution in the chemical making of gold oxidation catalysts. C. R. Chimie 19 (2016) 192-198.
26. J. S. Sekhon, S. S. Verma. Refractive Index Sensitivity Analysis of Ag, Au, and Cu Nanoparticles. Plasmonics 6 (2011) 311–317.
27. Y. Sun, Y. Xia. Increased Sensitivity of Surface Plasmon Resonance of Gold Nanoshells Compared to That of Gold Solid Colloids in Response to Environmental Changes. Anal. Chem. 74 (2002) 5297-5305.
28. J. J. Mock, D. R. Smith, S. Schultz. Local Refractive Index Dependence of Plasmon Resonance Spectra from Individual Nanoparticles. Nano Lett. 3 (2003) 485-491.
29. H. Chen, X. Kou, Z. Yang, W. Ni, J. Wang. Shape- and Size-Dependent Refractive Index Sensitivity of Gold Nanoparticles. Langmuir 24 (2008) 5233-5237.
30. L. J. Sherry, S. Chang, G. C. Schatz, R. P. Van Duyne. Localized Surface Plasmon Resonance Spectroscopy of Single Silver Nanocubes. Nano Lett. 5 (2005) 2034-2038.
31. O. Saison-Francioso, G. Lévêque, R. Boukherroub, S. Szunerits, A. Akjouj̃. Dependence between the Refractive-Index Sensitivity of Metallic Nanoparticles and the Spectral Position of Their Localized Surface Plasmon Band: A Numerical and Analytical Study. J. Phys. Chem. C 119 (2015) 28551−28559.
32. J. R. Lakowicz, K. Ray, M. Chowdhury, H. Szmacinski, Y. Fu, J. Zhang, K.

Nowaczyk. Plasmon-controlled fluorescence: a new paradigm in fluorescence spectroscopy. Analyst 133 (2008) 1308–1346.
33. B. Lamprecht, G. Schider, R. T. Lechner, H. Ditlbacher, J. R. Krenn, A. Leitner, F. R. Aussenegg. Metal Nanoparticle Gratings: Influence of Dipolar Particle Interaction on the Plasmon Resonance. Physical Review Letters 84 (2000) 4721-4724.
34. B. Auguìe, X.M. Bendaña, W. L. Barnes. Diffractive arrays of gold nanoparticles near an interface: critical role of the substrate. Phys. Rev. B 82 (2010) 155447.
35. S. Foteinopoulou, J. P. Vigneron, C. Vandenbem. Optical near-field excitations on plasmonic nanoparticle-based structures. Optics Express 15 (2007) 4253-4267.
36. A. K. Sarychev, V. A. Shubin, V. M. Shalaev. Anderson localization of surface plasmons and nonlinear optics of metal-dielectric composites. Physical Review B 60 (1999) 16389-16408.
37. M. Valamanesh, Y. Borensztein, C. Langlois, E. Lacaze. Substrate Effect on the Plasmon Resonance of Supported Flat Silver Nanoparticles. J. Phys. Chem. C 115 (2011) 2914–2922.
38. M. D. Malinsky, K. L. Kelly, G. C. Schatz, R. P. Van Duyne. Nanosphere Lithography: Effect of Substrate on the Localized Surface Plasmon Resonance Spectrum of Silver Nanoparticles. J. Phys. Chem. B 105 (2001) 2343-2350.
39. M. A. Mahmoud, M. A. El-Sayed. Substrate Effect on the Plasmonic Sensing Ability of Hollow Nanoparticles of Different Shapes. J. Phys. Chem. B 117 (2013) 4468−4477.
40. A. Biswas, I. S. Bayer, A. S. Biris, T. Wang, E. Dervishi, F. Faupel. Advances in top–down and bottom–up surface nanofabrication: Techniques, applications & future prospects. Advances in Colloid and Interface Science 170 (2012) 2–27.
41. C. J. Murphy, T. K. Sau, A. M. Gole, C. J. Orendorff, J. Gao, L. Gou, S. E. Hunyadi, T. Li. Anisotropic Metal Nanoparticles: Synthesis, Assembly, and Optical Applications. J. Phys. Chem. B 109 (2005) 13857-13870.
42. Y. Sun, Y. Xia. Shape-Controlled Synthesis of Gold and Silver Nanoparticles. Science 298 (2002) 2176-2178.
43. J. V. Barth, G. Costantini, K. Kern. Engineering atomic and molecular nanostructures at surfaces. Nature 437 (2005) 671-679.
44. J. C. Hulteen, R. P. Van Duyne. Nanosphere lithography: A materials general fabrication process for periodic particle array surfaces. J. Vac. Sci. Technol. A 13 (1995) 1553-1558.
45. S. Cataldo, J. Zhao, F. Neubrech, B. Frank, C. Zhang, P. V. Braun, H. Giessen. Hole-Mask Colloidal Nanolithography for Large-Area Low-Cost Metamaterials and Antenna-Assisted Surface-Enhanced Infrared Absorption Substrates. ACS Nano 6 (2012) 979-985.

46. S. Chen. Miniaturized localized surface plasmon resonance biosensors. Göteborg : Chalmers University of Technology, 2013. ISBN: 978-91-7385-851-9.
47. H. Fredriksson, Y. Alaverdyan, A. Dmitriev, C. Langhammer, D. S. Sutherland, M. Zäch, B.Kasemo. Hole–Mask Colloidal Lithography. Adv. Mater. 19 (2007) 4297–4302.
48. P. Colson, C. Henrist, R. Cloots. Nanosphere Lithography: A Powerful Method for the Controlled Manufacturing of Nanomaterials. Journal of Nanomaterials 2013 (2013) Article ID 948510.
49. W.S. Liao, X. Chen, T. Yang, E.T. Castellana, J. Chen, P.S. Cremer. Benchtop chemistry for the rapid prototyping of label-free biosensors: Transmission localized surface plasmon resonance platforms. Biointerphases 4 (2009) 80–85.
50. D.K. Kim, K. Kerman, M. Saito, R.R. Sathuluri, T. Endo, S. Yamamura, Y.S. Kwon, E. Tamiya. Label-free DNA biosensor based on localized surface plasmon resonance coupled with interferometry. Anal. Chem. 79 (2007) 1855–1864.
51. J. L. Hammond, N. Bhalla, S. D. Rafiee, P. Estrela. Localized Surface Plasmon Resonance as a Biosensing Platformfor Developing Countries. Biosensors 4 (2014) 172-188.
52. K. S. McKeating, A. Aubé, J. Masson. Biosensors and nanobiosensors for therapeutic drug and response monitoring. Analyst 141 (2016) 429-449.
53. O. Tokel, F. Inci, U. Demirci. Advances in Plasmonic Technologies for Point of Care Applications. Chem. Rev. 114 (2014) 5728−5752.
54. A.B. Dahlin, N. J. Wittenberg, F. Höök, S. Oh. Promises and challenges of nanoplasmonic devices for refractometric biosensing. Nanophotonics 2 (2013) 83–101.
55. T. A. Bendikov, A. Rabinkov, T. Karakouz, A. Vaskevich, I. Rubinstein. Biological Sensing and Interface Design in Gold Island Film Based Localized Plasmon Transducers. Anal. Chem. 80 (2008) 7487−7498.
56. G. Cappi , E. Accastelli, V. Cantale, M. A. Rampi, L. Benini, C. Guiducci. Peak shift measurement of localized surface plasmon resonance by a portable electronic system. Sensors and Actuators B 176 (2013) 225–231.
57. J. Jana, M. Ganguly, T. Pal. Enlightening surface plasmon resonance effect of metal nanoparticles for practical spectroscopic application. RSC Adv. 6 (2016) 86174-86211.
58. O. Kedem, A. Vaskevich, I. Rubinstein. Critical Issues in Localized Plasmon Sensing. J. Phys. Chem. C 118 (2014) 8227–8244.
59. G. Barbillon. Determination of Evanescent Electric Field Decay Length of Metallic Nanodisks by Using Localized Surface Plasmon Spectroscopy. Journal of Materials Science and Engineering 4 (2010) 69-74.
60. M. M. Miller, A. A. Lazarides. Sensitivity of Metal Nanoparticle Surface Plasmon

Resonance to the Dielectric Environment. J. Phys. Chem. B 109 (2005) 21556-21565.

61. A. J. Haes, R. P. Van Duyne. A Nanoscale Optical Biosensor: Sensitivity and Selectivity of an Approach Based on the Localized Surface Plasmon Resonance Spectroscopy of Triangular Silver Nanoparticles. J. Am. Chem. Soc. 124 (2002) 10596-10604.
62. J. Ye, P. Van Dorpe. Improvement of Figure of Merit for Gold Nanobar Array Plasmonic Sensors. Plasmonics 6 (2011) 665–671.
63. B. Paivänränta, H. Merbold, R. Giannini, L. Buchi, S. Gorelick, C. David, J. F. Löffler, T. Feurer,Y. Ekinci. High Aspect Ratio Plasmonic Nanostructures for Sensing Applications. ACS Nano 5 (2011) 6374–6382.
64. O. Saison-Franciosò, G. Lëvéquê, A. Akjouj, Y. Pennec, B. Djafari-Rouhani, S. Szunerits, R. Boukherroub. Plasmonic Nanoparticles Array for High-Sensitivity Sensing: A Theoretical Investigation. J. Phys. Chem. C 116 (2012) 17819−17827.
65. P. K. Jain, K. Seok Lee, I. H. El-Sayed, M. A. El-Sayed. Calculated Absorption and Scattering Properties of Gold Nanoparticles of Different Size, Shape, and Composition: Applications in Biological Imaging and Biomedicine. J. Phys. Chem. B 110 (2006) 7238-7248.
66. I. M. White, X. Fan. On the performance quantification of resonant refractive index sensors. Opt Express. 16 (2008) 1020–1028.
67. J. N. Anker, W. Paige Hall, O. Lyandres, N. C. Shah, J. Zhao, R. P. Van Duyne. Biosensing with plasmonic nanosensors. Nature Materials 7 (2008) 442 – 453.
68. H. M. Strauss, E. Karabudak, S. Bhattacharyya, A. Kretzschmar, W. Wohlleben, H. Cölfen. Performance of a fast fiber based UV/Vis multiwavelength detector for the analytical ultracentrifuge. Colloid. Polym. Sci. 286 (2008) 121–128.
69. S. L. Upstone. Ultraviolet/Visible Light Absorption Spectrophotometry in Clinical Chemistry. Encyclopedia of Analytical Chemistry. PerkinElmer Ltd., Beaconsfield, UK (2000).
70. Z. Es'haghi. Photodiode Array Detection in Clinical Applications; Quantitative Analyte Assay Advantages, Limitations and Disadvantages. Photodiodes - Communications, Bio-Sensings, Measurements and High-Energy Physics. CC BY-NC-SA (2011).
71. E. U. Woehl, C.Tai, M. F. Dunn, P. F. Cook. Formation of the α-Aminoacrylate Intermediate Limits the Overall Reaction Catalyzed by O-Acetylserine Sulfhydrylase. Biochemistry 35 (1996) 4776-4783.
72. A. B. Dahlin, J. O. Tegenfeldt, F. Höök. Improving the Instrumental Resolution of Sensors Based on Localized Surface Plasmon Resonance. Anal. Chem. 78 (2006) 4416-4423.
73. J. Homola. Surface Plasmon Resonance Sensors for Detection of Chemical and Biological Species. Chem. Rev. 108 (2008) 462−493.
74. G. G. Nenninger, M. Piliarik, J. Homola. Data analysis for optical sensors based on spectroscopy of surface plasmons. Meas. Sci. Technol. 13 (2002) 2038–2046.

CHAPTER 2.

KINETICS STUDY OF ADSORPTION COMPETITION

AT HYDROPHOBIC AND HYDROPHILIC SURFACES

2.1 Introduction

2.1.1 Protein structure and function

Proteins are large biological heteropolymers (i.e. their molecular masses range from a few thousand to several hundred thousand kDa) composed by a number of amino acids [1]. Amino acids consist of three parts; an amino group (-NH_2), a carboxyl acid group (-COOH), and a side group (-R). A large variety of side groups exist, and the characteristics of an amino acid depend to a large extent on the side group. Due to the great variety of physical and chemical properties among the amino acids, including charge, hydrophobicity, and acid/base character, proteins obviously also exhibit great variation in physical and chemical characteristics [2]. Furthermore, the environment in which the amino acid is present plays a key role [3]. In particular the pH is an important parameter. For low values of the pH, that is high concentrations of H^+ ions, the amino group will acquire an extra H^+ ion, resulting in an -NH^+_3 group. On the other hand, at high values of pH the -COOH group will lose an H^+ ion becoming –COO^-. At intermediate pH values, the amino acid will typically undergo both of the above-mentioned processes, making the molecule zwitterionic. It should be noted that this process is in fact counterproductive when it comes to binding a number of amino acids together and form a protein [4]. To accomplish the latter, a C-O and a N-H bond must be broken, resulting in water as a by-product of the polymerization, since an -OH group will leave the C-atom from the carboxyl group and an H-atom the amino group. It turns out that to hold the protein together, the π-bond between the carbon atom and the last oxygen atom will be shared by the oxygen atom and the nitrogen atom from the amino group. This bond is known as an amide bond. An important consequence is the fact that the carbon, oxygen and nitrogen atoms must lie in the same plane (the amide plane), imposing a rather severe restriction on the spatial arrangement of the amino acids with respect to one another [5]. A protein can be characterized at various levels of complexity. First, the particular sequence of amino acids determines the primary structure of the protein. Second, even though the rotational freedom is reduced due to the constraint mentioned above, the bonds between the nitrogen and its other carbon neighbor as well as the bond between this and the next carbon are σ-bonds permitting a large degree of rotational freedom [6]. The structure determined by this flexibility in the chain is called the secondary structure. Two famous secondary structures are the α-helix and the β-sheet [7]. These are held together by hydrogen bonds. Another important secondary structure is the random coil. Third, the three-dimensional arrangement of the secondary structure is known as the tertiary

structure. An example would be domains of fi-helices connected by random coil structures [8]. Fourth, if several different tertiary structures are bound together, e.g. several globular domains [9] and random coil structures [10], one speaks of a quarternary structure [11]. Unlike simple homopolymers, which usually have a random coil shape with a size determined by the solvent [12], proteins have a single, distinct three dimensional structure (tertiary or quarternary) at physiological conditions, that is, at a pH close to 7.4 and a temperature about 37 °C. This shape is called the native state, and is controlled by the non-covalent interactions along the chain [13]. Going sufficiently far beyond physiological conditions, the protein will change its shape from the well-defined native state to a denatured state [14], the latter being more like a random coil. This process will drastically alter the function of the protein [15]. While different proteins exhibit many different shapes in the native state, a simple division between water soluble and water insoluble proteins proves useful. Usually water soluble proteins take a globular shape and their amino acid composition is characterized by less regularity [16]. An important example is serum albumin, while a prominent exception is fibrinogen. Proteins which are not soluble in water usually have a more complex three-dimensional structure, typically a fibrous structure, and a more regular amino acid composition, an example is collagen [17]. As was the case for amino acids, the pH value is important for the properties of the protein. The pH at which the protein is uncharged is called the isoelectric point, denoted pI [18]. At pH values below the pI the protein is positively charged, and opposite for pH values above the pI. The ion concentration in the solution in which the protein is present (the ionic strength) is also important in determining the protein properties due to the impact additional ions will have on the electrostatic interactions [19].

2.1.2 Protein-surface interactions and factors controlling protein adsorption

A good perspective for protein adsorption studies is that most of the proteins adsorb to almost all surfaces [20]. It is rarely a problem to achieve the adsorption of a protein, but rather how to prevent it [21]. This observation reflects the fact that the free energy for the protein-surface system will be at a minimum when the protein is adsorbed. Therefore, the knowledge of the protein-surface interactions would be of value in order to understanding and eventually controlling the factors relevant for protein adsorption [22].

The interactions between proteins, and between proteins and solid surfaces are mostly non covalent [23], such as hydrogen-bonding, hydrophobic, Coulomb and Van der Waals interactions.

- Hydrogen bonds.

Most of the H-bonds in proteins are between amide and carbonyl groups of the polypeptide backbone. They are short ranged (<< 0.1 nm) and have an effect on the stability of protein structure [24]. Formation of H-bonds appears not to be the main driving force for protein adsorption [25].

- Hydrophobic interaction.

This is a strong attraction between nonpolar (hydrophobic) molecules and surfaces in water [26]. For proteins the dehydration of nonpolar parts of the polypeptide in water is favorable because it leads to a decrease of the Gibbs energy of the system. This hydrophobic dehydration is considered to be the primary driving force for the folding process [27].

- Coulomb interaction.

The pure electrostatic forces between charges. Since most of the charged amino-acid residues in a protein molecule are located at the aqueous periphery, this leads to a strong electrostatic interaction with charged surfaces [28]. Usually, the protein surface is not homogeneously charged. Close to the protein isoelectric point (pI) the interaction between proteins is attractive and repulsive when remote from pI [29]. By varying the pH of the solution the charges of the surface and protein can be changed. The electrostatic interaction is an important driving force for the protein adsorption process, as indicated by many studies [30].

- Lifshitz-Van der Waals interaction.

The Lifshitz-Van der Waals (LW) interaction is a result of interactions between induced dipoles [31]. The Van der Waals force for macrobodies is long range attractive, and relatively weak. One of the most widely used models, often applied to calculate the non-covalent interaction between biological colloids in terms of Gibbs energy, is Derjaguin-Landau-VerweyOverbeek (DLVO) theory [32]. This theory has been applied to the study of protein adsorption based on the assumptions that the particles are rigid, spherical, charged objects and their interactions with each other and with the surface (electrostatic, Van der Waals and solvation forces) are pairwise and additive [33]. The assumption of rigidity is justified if the native structure of the protein is not significantly changed upon protein-surface interaction. It is not surprising that the interaction of "hard" globular protein such lysozyme with solid surfaces can be reasonable well described by the DLVO model [34], which is far less suitable for "soft" nonspherical proteins like albumin and fibrinogen [33].

Adsorption of proteins onto inorganic surfaces represents unspecific binding; in contrast to specific binding, where some sites are preferable for binding and some are not, the inorganic surface represents a continuum of possible binding sites [35]. Once on the surface, the protein can undergo several processes. Surface diffusion is a particular important process [36]. Desorption can also occur, however very often protein adsorption is in fact irreversible [37]. Relaxation processes, where the protein increases its number of bonds to the surface, typically leading to a much larger area occupied by one protein, is often observed. The adsorption may even lead to denaturation of the protein [21].

According to this framework of interactions, the main factors ruling protein adsorption can be classified as external, i.e. solution parameters and surface parameters, and internal, i.e. proteins properties.

Solution parameters are basically temperature, pH, ionic strength and buffer composition [38]. Temperature has an effect on both, the equilibrium state and the kinetics of protein adsorption [39]. The major driving force of protein adsorption is an entropy gain arising from the release of surface adsorbed water molecules and salt ions and from structural rearrangements inside the protein [40].

The amount of surface adsorbed proteins therefore generally increases at elevated temperatures [39].

The pH determines the electrostatic state of proteins. Electrostatic protein–protein repulsions are minimized at the isoelectric point allowing higher packing densities on the surface [41]. Adsorption rates are high when protein and substrate bear opposite charges since electrostatic attractions accelerate the migration towards the surface [42]. However, the total mass load is generally observed to be maximized at the isoelectric point [43].

Another parameter controlling protein adsorption processes is the concentration of dissolved ions expressed by the term ionic strength. The ionic strength basically determines the Debye length correlating with the damping distance of the electric potential of a fixed charge in an electrolyte [44]. That means the higher the ionic strength the shorter are electrostatic interactions between charged entities. The efficient screening of the electric potential of proteins reduces lateral interactions which are usually of electrostatic nature [44]. This in turn may initiate an increase in packing density, a suspension of cooperative effects, or protein– protein repulsions [43].

For more than a century it has been known that high salt concentrations promote the precipitation of colloidal substances which is known as the 'salting out' effect due to water absorption by salt ions. Ions that promote protein precipitation are called kosmotropes (e.g. SO_4^{2-}, F^-, Mg^{2+} and Ca^{2+}) ions that decelerate protein precipitation are called chaotropes (e.g. ClO^{4-}, SCN^- and NH^{4+}) [45]. It was suggested that this effect correlates with the ability to stabilize (kosmotropic effect) or destabilize (chaotropic effect) the native conformation of proteins which would influence their adsorption tendency [45].

Important surface properties that have to be considered in the study of protein adsorption include surface energy, polarity, charge, adhesion and morphology [46].

Parameters, such as surface energy, charge, and polarity can be easily tuned by choosing the appropriate chemical functionalities by surface modifications methods [46]. Regarding to surface chemistry effect on protein adsorption, it is well-known that proteins tend to adhere more strongly to nonpolar than to polar, to high surface tension than to low surface tension and to charged then to uncharged substrates. It is reported in literature [47] that non-polar surfaces destabilize proteins and thereby facilitate conformational reorientations leading to strong inter protein and protein–surface interactions. This explains the rather general experimental finding that in most cases the affinity of proteins to surfaces increases on hydrophobic substrates and decreases on hydrophilic substrates [48].

A classification of proteins with respect to their interfacial behavior can be achieved by considering properties like size, structural stability and composition [49]. To this end small and rigid proteins like Lysozyme, β-Lactoglobulin, or α-Chymotrypsin are referred to as 'hard' proteins suggesting a generally little tendency for structural alterations upon surface adsorption [50, 51, 52]. Intermediate size proteins such as the majority of the abundant (>1 mg/ mL) plasma proteins like Albumin, Transferrin, Immunoglobulins, etc. are usually able to undergo conformational reorientations upon surface contact [53]. The class of high molecular weight proteins includes polymer-like lipoproteins and

glycoproteins whose behavior is essentially dominated by the content of lipids or glycans. Lipoproteins are structurally labile and therefore show a strong affinity to hydrophobic surfaces including significant conformational reorientations [54]. By contrast, adsorption of glycoproteins on hydrophobic surfaces is hindered due to a high content of hydrophilic glycan [55].

2.1.3 Modeling protein adsorption

Generally, adsorption processes can be divided into two classes, reversible and irreversible. The first class includes adsorption processes in which relaxation mechanisms such as desorption and diffusion are present. Equilibrium statistical mechanics is capable of describing the process, and the physical systems belonging to this class are typically adsorption of smaller molecules. The most well-known isotherm belonging to this class is the Langmuir isotherm [56]. In the second class, the adsorption proceeds without the above relaxation mechanisms. Large molecules adsorbing onto a substrate typically belong to this class, since their interaction energies in the adsorption process are often larger than the thermal energy [57]. A theoretical description is more complicated because equilibrium statistical mechanics is no longer sufficient [57].

The simplest concept in an adsorption process is the fraction of the surface area covered with molecules, denoted ϑ, or the surface density, denoted Γ (e.g. in ng/cm^2). It is easy to relate ϑ to the surface density Γ, the latter being the quantity one measures; $\Gamma = \theta \frac{m}{a}$, where m is the protein mass and a is the area one protein covers, often referred to as the footprint. While m has a well-defined value (reflecting that the proteins adsorb as one entity), a may be different from the dimensions of the protein in the liquid, since a protein often increases its footprint in order to obtain a more favorable adsorbed state on the surface [58]. Sometimes the number of adsorbed particles per area, ν, is used. It is simply given as $\nu = \frac{\theta}{a}$.

A model for adsorption will typically describe the temporal evolution of Γ through a differential equation having the following general form [56]:

$$\frac{d\Gamma}{dt} = k_a c \Phi(\theta) - k_d \theta \qquad Eq.\ 28$$

In Eq. 28, k_a and k_d are the adsorption and desorption rates, respectively, c is the bulk concentration of proteins, and Φ is a function giving the ratio of the available surface area for adsorption to the total area of the substrate. Note, that often protein adsorption can be regarded as an irreversible process, which is equivalent to neglecting desorption, that is k_d = 0 [57]. Φ is known as the available area function, and obviously Φ is a function of the already covered fraction of the area, θ. Depending on model, the functional relationship ranges from simple to complicated. Often the coverage at saturation is the quantity one is most interested in. In the simplest case where the footprint is exactly

equal to the area of the one site on the substrate, it is possible to have a surface coverage of one. Considering the more realistic case where the area of the adsorbing particles does play a role, the maximal coverage for spherical particles will be 0.91, corresponding to a hexagonal close packed lattice [59]. This limit is rather artificial too, because protein adsorption often proceeds far from equilibrium, thus no relaxation mechanisms, such as desorption or surface diffusion, are present to create an equilibrium structure. Instead, lower coverages at saturation are to be expected. This limit is known as the jamming limit. The value of the jamming limit is dependent on the adsorption algorithm as well as on the shape of the adsorbing particles (spherical, ellipsoidal, triangular etc.) [60].

2.1.3.1 Diffusion limited adsorption

The simplest model for adsorption is diffusion limited adsorption. In this model the transport towards the surface is purely diffusive, and this transport is the limiting factor. If a particle reaches the surface it will adsorb irreversibly with probability one. Hence no reference to the surface properties is present in the expression for the surface density. The surface density evolves in time as [61],

$$\Gamma(t) = 2c\sqrt{\frac{Dt}{\pi}} \qquad Eq.\ 29$$

where *c* is the bulk protein concentration, and D is the diffusion constant for the protein. Normally, the adsorption process will be diffusion limited in the early stages only [62]. At later times, the process becomes kinetically limited, meaning that the limiting factor is no longer transport to the surface, but the fact that the adsorption does not take place with probability one even if the protein is at the surface [27]. It is also important to note how the concentration enters Eq. 29; going to higher concentrations will increase the adsorption rate.

2.1.3.2 The Langmuir model

Another very simple model for adsorption is the above mentioned Langmuir model [56]. Particles are assumed non-interacting, and only monolayers are permitted. Adsorption and desorption are both incorporated with rates k_a and k_d, respectively. Furthermore, all non-covered area is available to adsorption resulting in the following form of the available area function; $\Phi(\theta)=1-\theta$. The differential equation for θ (Eq. 28) becomes;

$$\frac{d\Gamma}{dt}=k_a c\Phi(\theta)-k_d\theta \qquad Eq.30$$

Using the fact that $\theta=\frac{a}{m}\Gamma$, Eq. 30 can be solved ;

$$\Gamma(t)=\frac{m}{a}\frac{ck_a}{k_d+ck_a}\left(1-e^{-\left((k_d+ck_a)\frac{a}{m}t\right)}\right) \qquad Eq.31$$

Using a as a fitting parameter, the average protein footprint can be found. The adsorption and desorption constants, k_a and k_d, are typically fitting parameters too. The Langmuir model describes reversible adsorption, and it is often used in the case of deposition of atoms or small molecules. It should be used with care when large molecules are concerned, since these often adsorb irreversibly. If an irreversible version of the Langmuir model is considered, a maximum relative coverage of one can be attained (set k_d= 0, and $t\rightarrow\infty$). Often this is not physically meaningful, because on average the adsorbing particles, especially large ones, will exclude more area than their actual size. This means that the relative saturation surface density should be less than one.

2.1.3.3 The Random Sequential Adsorption model

As an improvement over the Langmuir model the Random Sequential Adsorption (RSA) model provides a useful framework for analyzing and interpreting measurements of protein adsorption when geometrical effects play a role [63]. Again only monolayers are permitted, and the only interaction between the particles is a hard sphere repulsion. Deposition proceeds according to the following rule: (i) A position in the substrate plane is chosen at random. (ii) A particle with a certain size and shape will adsorb irreversibly provided there is sufficient space around the position. (iii) If there is not enough space, a new adsorption attempt is made somewhere else. The model describes irreversible adsorption where geometrical blocking plays a key role. For hard spheres several results exist. The jamming limit is given as θ_j = 0.547 [63] for adsorbing in two substrate dimensions (2+1 dimensions), and for low coverages ($\theta<0.3-0.4$) the function Φ has the following form [64]:

$$\Phi(\theta) = 1 - 4\theta + \frac{6\sqrt{3}}{\pi}\theta^2 + \left(\frac{40}{\sqrt{3}\pi} - \frac{176}{3\pi^2}\right)\theta^3 + \mathrm{O}(\theta^4) \qquad Eq.\,32$$

Eq. 32 is to be understood in the following way: For a low coverage, the available area is close to one. However, as the substrate starts to fill, the corrections become more and more pronounced. These corrections are embodied in the higher order powers. At some point the substrate cannot accommodate more particles, even though some non-covered area exist, and the process has reached the jamming limit. Note that even for low degrees of coverage the Langmuir result is not retrieved, a factor of 4 is present in front of the first order term, in contrast to the Langmuir model.

2.1.3.4 Comparing data models

The Langmuir and RSA models outlined above represent the simplest and most useful models for interpretation of protein adsorption data. However, to ensure an unbiased interpretation of experimental data, one should first plot $\frac{d\Gamma}{dt}$ versus Γ [65].

If the curve follows a straight line, the kinetics can be assumed to follow Langmuir kinetics to a good approximation [66]. On the other hand if the data deviates from a straight line, Langmuir kinetics can be definitely excluded, and this is typically the case for most proteins, although going to low concentrations or low ionic strengths can make the kinetics Langmuir-like for some proteins [67]. The explanation for this behavior is the fact that in these particular cases the adsorption allows sufficient reorganization or clustering on the surface, resulting in basically all non-covered area being available for adsorption, which in turn implies in $\Phi(\theta) = 1 - \theta$. The available area functions for the RSA and the Langmuir model are illustrated in Figure 20.

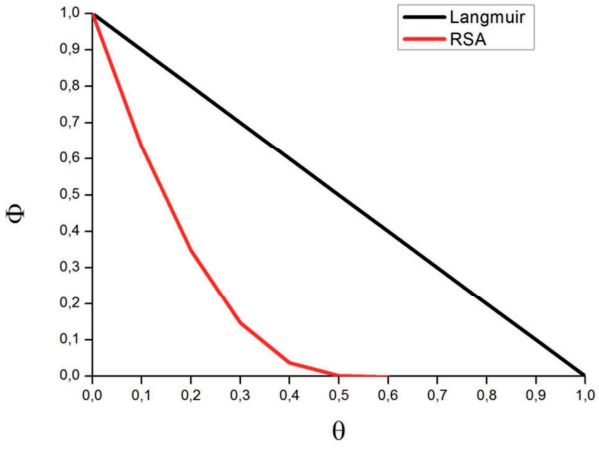

Figure 14. The available area vs. covered area for the Langmuir model and the RSA model [65].

If the curve deviates from a straight line, one should try to make a fit with Eq. 32. It is important to stress the fact that even though a reasonable fit can be obtained, this does not mean that the RSA model is the correct description.

Another aspect to be aware of is the particular form of the adsorbing particles [60]. The jamming limit of 0.547 and the expression for the available area function, Eq. 32 apply only to spherical particles. A way of obtaining information about the form of the adsorbing particles is to plot the quantity $\Gamma_j - \Gamma(t)$ versus time.

Using the following as a fitting function:

$$\Gamma_j - \Gamma(t) = kt^{-\frac{1}{d}} \qquad Eq.33$$

in the case *d*=2 the result for spherical particles can be applied. However, most importantly the jamming limit will change to a slightly lower value, about 0.535 for ellipsoidal objects with an aspect ratio about 7:1 [60].

2.1.4 Label-free detection methods for protein adsorption at solid-liquid interface

Due to its very complex nature, the study of adsorption of plasma proteins to solid surfaces has been mostly focused either on the quantitative aspects of adsorption of single proteins, or the reorganization events responsible for the biofunctionality of the adsorbed proteins [68]. Both these aspects of the protein adsorption processes are indeed very important, but it seems obvious that the adsorption processes are strongly conditioned by the inherent kinetics aspects of the whole adsorption process. Thus, important facts such as adsorption selectivity or the adoption of a specific conformation of the adsorbed proteins must be discussed in terms of the previous transport of proteins from the bulk of solution to the solid-liquid interface as well as the kinetics of their binding to the surface, clearly involving also the range and relative strength of the relevant acting surface-molecule interactions [69], and the kinetics of the protein relaxation mode after adsorption [70].

In the last 15 years essentially acoustic and optical detection techniques have been used to monitor the adsorption processes at interfaces [71]. All these techniques have specific strengths and weaknesses regarding, e.g., use of molecule labeling, ease of use, type of information gained, degree of transducer complexity, detection limits and how quantitative the obtained data is [72]. In this context, one of the most used techniques has been the quartz crystal microbalance with dissipation monitoring (QCM-D) allowing to investigate in real time the quantitative and viscoelastic aspects of the protein adsorption [73]. However, a major drawback of the techniques has been shown to concern the determined mass, as it has been shown to include significant and unpredictable amounts of water molecules associated with the adsorbed protein layer and adsorbent surfaces, i.e., the so called “wet mass” [74], thus yielding a basic uncertainty in the interpretation of the data, especially

when the matter of interest is the study of protein adsorption on substrates with different hydrophobicity [75].

At variance of this, conventional optical techniques (e.g. surface plasmon resonance (SPR), spectroscopic ellipsometry (SE), optical waveguide lightmode spectroscopy (OWLS)), based on the analysis of refractive index changes produced by the protein adsorption events and being insensitive to the solvent trapped in the protein adlayer [76], allowed the direct measurement of the real amount of protein molecules in the adsorbed layer, indicated as "dry mass". Nevertheless, the decay length of the evanescent wave associated with these techniques is at least one or two order of magnitude bigger than the protein layer thickness, limiting the depth resolution of such techniques and making the data critically influenced by bulk refractive index changes [77].

Recently, a new surface sensitive technique, i.e., localized surface plasmon resonance (LSPR), has been developed, based on the sensing properties of evanescent waves propagating just for a few nanometers from the sensing surface (5-30 nm) [78]. The LSPR technique has proved to be particularly suitable for studies aimed to determine the real adsorbed masses of biomolecule in ultrathin layers, whatever the nature of the substrate [79]. The present paper reports on the use of LSPR to determine the real kinetics, i.e., skipping the perturbing effect of different hydration contribution to the adsorbed protein mass, of single and competitive adsorption processes from protein solutions.

In particular, we report the adsorption kinetics of Human Serum Albumin (HSA) and Human Plasma Fibronectin (Fn) from single and binary solutions onto hydrophilic and hydrophobic model surfaces, obtained by functionalization of nanostructured LSPR sensor chips.

2.2 Materials and Methods

2. 2.1 Chemicals

Human serum albumin (HSA, Catalog No A3782) and plasma fibronectin (FN, Catalog No F2006) were purchased from Sigma-Aldrich and used as supplied without further purification step. A solution of HSA was prepared in phosphate buffer (PBS) at concentration 0.1 mg/mL (1.5×10^{-6} M) and FN solution was prepared at a concentration of 0.1 mg/mL (2.3×10^{-7} M). Monoclonal antibody of albumin (anti-HSA) was obtained from Sigma-Aldrich (code A6684) reacts specifically against denatured and reduced human albumin. It was employed as a solution in phosphate buffer at a final concentration of 3.0×10^{-5} M. Polyclonal rabbit antifibronectin (anti-Fn) was obtained from Sigma-Aldrich (code F3648) and was employed as a solution in phosphate buffer at a final concentration of 3.3×10^{-5} M. The employed anti-Fn belongs to the IgG_1 subclass and interacts by its Fc portions with the $^4F^1 \cdot ^5F^1$ segments within Fn.

Phosphate buffer solution (PBS) was prepared by dissolving 1 tablet (from Sigma-Aldrich) in 200 mL of ultrapure water (processed by a Millipore system with 18.2 M Ω resistivity), resulting in a solution

ionic strength of 10^{-2} M for the phosphate salts, $2.7x10^{-3}$ M for potassium chloride, and 0.137 M for sodium chloride (pH 7.4 at 25°C). The same buffer was used for all of the adsorption experiments.

2.2.2 Sensing surfaces

For the LSPR measurement the sensing surface consists of a glass slide decorated nanodisks with a random arrangement as prepared by a hole-mask colloidal lithography [80]. On top of the gold nanodisks a 3 nm chromium layer was deposited. The latter served as an adhesion layer for the subsequent deposition step of a 10 nm thick layer of SiO_2 obtained by PECVD. The schematic description of the sensor section is sketched in Figure 15 A.

The surface of the sensor chip has been characterized by Digital Image AFM in tapping mode. A Pointprobe NCH-50 silicon probe from Nanosensors is used as AFM tip.

The individual SiO_2-coated gold nanodisks has an average height and diameter of 25±5 nm and 150±5 nm respectively (see Figures 15 B and 15 C). The average interparticle pitch is estimated to be approximately 330 ± 25 nm. The root square roughness (R_q) is 6.2±0.2 nm. A glass slide contains deposited nanodisks with a random arrangement and with surface coverage of 7%.

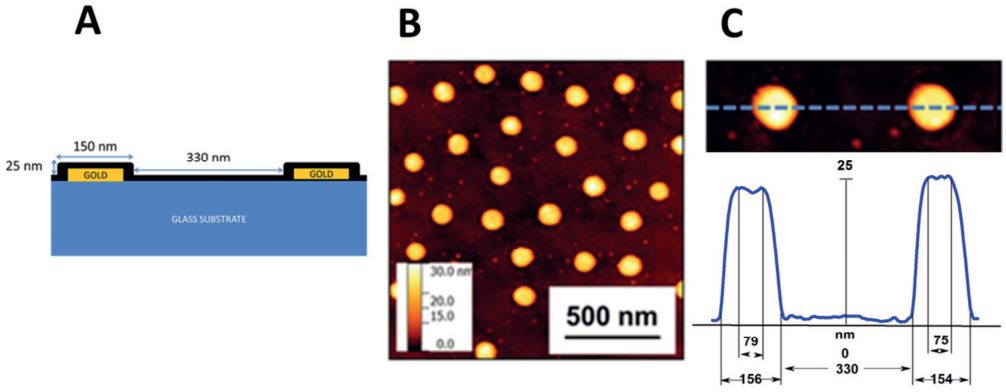

Figure 15. (A) Schematic description of LSPR sensor structure. (B) AFM image of LSPR sensor chip surface and corresponding section analysis of individual nanodisks (C).

The hydrophilic surfaces were prepared by treating the LSPR sensor surface in an UV-O_3 discharge (BioForce Nanoscience, Ames, USA) for 15 min, then rinsed with Millipore water and dried under a nitrogen flow (these samples will be henceforth indicated as Hyl-SiO_2). The hydrophobic surfaces were prepared by depositing Octadecyltrichlorosilane (henceforth indicated as OTS) on the surface of the SiO_2-coated LSPR sensor accordingly to the following procedure. The sensor surface were treated with UV-O_3 for 8 min, then rinsed with water and ethanol, and thoroughly dried under nitrogen stream. Subsequently, they were dipped into a $4x10^{-4}$ M OTS solution in hexadecane/chloroform (5/15 v/v) for 1 h at the temperature of 40 °C. The excess of OTS was removed from the sensor

surface by rinsing with mixture of hexadecane /chloroform and ethanol. Finally, the surfaces were dried with nitrogen gas.

After the deposition, the hydrophobized sensor surface was characterized by AFM (data not shown). No significant change was observed either in surface topography or R_q values with respect to untreated SiO_2 surface suggesting that the deposited OTS layer is uniform. Furthermore, the thickness of the deposited OTS layer was determined by using LSPR technique. In details, we measured the adsorption spectra of SiO_2 – coated gold nanodisk array (henceforth indicated as plasmon peak) on the surface of LSPR sensor chip before and after the OTS deposition (see Figure 16). Assuming that the deposited layer was an uniform, the plasmon peak shift (0.4 $\pm$ 0.02 nm) can be converted in optical thickness [81] according to the following equation:

$$\Delta\lambda = S\left[1 - e^{-\frac{t}{L}}\right]\left(n_{OTS} - n_{AIR}\right) \qquad Eq.\,34$$

Where S = 72 nm/RIU is the bulk refractive sensitivity of the LSPR sensor, L = 27.2 nm the decay length of the LSPR evanescent wave according to sensor specification, t is the adsorbed protein layer thickness, n_{OTS}=1.55 and n_{AIR} =1.00 are respectively the bulk refractive index for the a uniform OTS layer [82] and the air medium.

The calculated thickness (2.8$\pm$0.1 nm) is in good agreement with the value reported in literature for a OTS monolayer [83] (The reported values is the mean of three independent depositions +/− standard deviation).

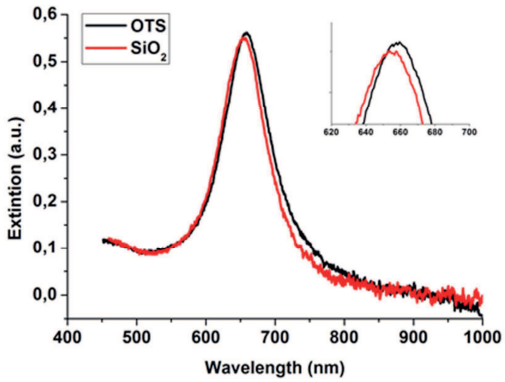

Figure 16. Adsorption spectra of SiO_2 – coated gold nanodisk array on the surface of LSPR sensor chip before and after the OTS deposition.

2.3 Result and discussion

The real-time adsorption of the protein "dry" mass was detected by means of an Insplorion XNano instrument (Insplorion AB, Göteborg, Sweden), providing the plasmonic peak shift (Δλ) as a function of adsorbed matter and time.

Fig. 17 reports the LSPR response for the adsorption of HSA and Fn, respectively, onto Hyl-SiO_2 and OTS substrates at 25°C from a 100 µg/ml protein solution prepared in 0.01 M phosphate buffer (PBS), pH 7.4.

Assuming that each adsorbed protein, at the steady state, forms an uniform adlayer on both surfaces, the LSPR response can be converted in optical thickness using Eq.34. However, in this case, we substituted the refractive index of OTS layer and air medium with the corresponding value for a uniform proteinaceous layer ($n_{protein}$=1.456) [84] and the buffer solution(n_{buffer}=1.335) as shown below

$$\Delta\lambda = S\left[1 - e^{-\frac{t}{L}}\right]\left(n_{protein} - n_{buffer}\right) \qquad Eq.35$$

The protein adlayer thickness has been further converted in dry mass (M) according to the De Feijter's equation [85],

$$M = t\frac{n_{protein} - n_{buffer}}{\frac{dn}{dc}} \qquad Eq.36$$

Where dn/dc is the refractive index increment for a concentration change assumed to be nearly constant for protein solutions, at a value of 0.18 cm^3/g [69].

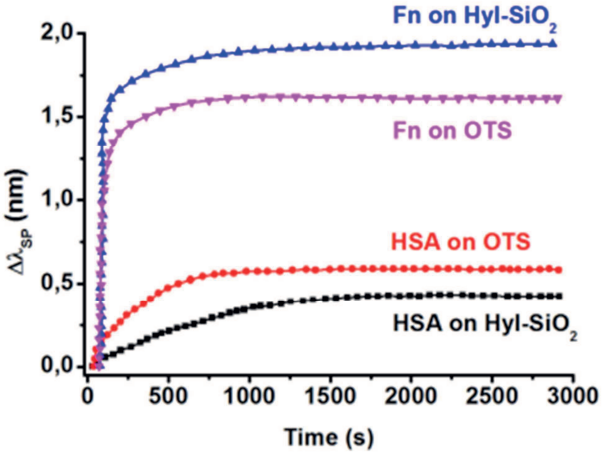

Figure 17. Single protein adsorption curves by LSPR respectively for HSA and Fn solutions (100 µg/ml, buffer PBS 0.01 M, pH = 7.4, T= 25.0 °C).

Figure 17 reports the shift of the plasmon wavelength for the HSA and Fn adsorption processes, which, converted in effective thickness by using Eq.35, shows that, for both surfaces, the adsorbed amount of Fn is higher than the one of HSA. Furthermore, while the amount of adsorbed HSA is slightly higher for OTS surfaces (with an effective thickness of the adsorbed layer t = 2.2 nm), than for Hyl-SiO_2 (t = 1.5 nm), Fn adsorption follows an opposite trend, with a higher adsorption onto Hyl-SiO_2 (t = 7.8 nm) than onto OTS (t = 5.9 nm). It is to note that the measured thickness of the adsorbed protein layers is lower than the protein native dimension both for HSA (4x4x14 nm^3) and Fn (16.5 x 9.6 x 2.5 nm^3). According to well-established literature, globular HSA predominantly undergoes a drastic denaturation process and Fn is adsorbed in a random/non-oriented fashion yielding the thickness reported above is intermediate between the two molecular shorter axes, i.e., 9.6 and 2.5 nm. In overall, these findings are in nice agreement with previous reports for albumin and fibronectin [86-89].

LSPR experiments suggest that the kinetics adsorption paths for the two proteins and the two surfaces can be simply analyzed in terms of a two-step model, including a first, an almost linear and fast step corresponding to a simple diffusion-controlled kinetic model [90], followed by a second slow adsorption step, corresponding to a simple random sequential adsorption (RSA) model [91]. In particular, the first step can be fitted in the framework of the above mentioned diffusion-controlled model by using the following equation [90]:

$$M = 2C_b\sqrt{\frac{D}{\pi}t^{\frac{1}{2}}} \qquad Eq.37$$

where M is the adsorbed mass, C_b is the protein concentration in the bulk solution and D is the diffusion coefficient of the protein from the solution to the adsorbent surfaces. According to the equation, we obtained that the very early rising adsorption steps are fitted with straight lines, one characterized by a peculiar value of the diffusion coefficient D for each protein, corresponding to the different slope of the adsorption process respectively for HSA and Fn (see Figure 18 A).

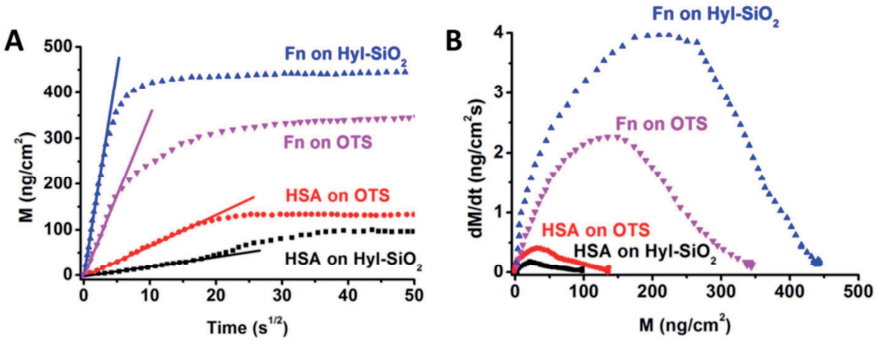

Figure 18. (A) Protein adsorbed mass (ng/cm^2) vs. square root of time ($s^{1/2}$). The straight line fit of the 1st adsorption steps is shown for each curve. (B) Rate of adsorption as a function of deposited mass density for HSA and Fn solution (100 μg/ml, buffer PBS 0.01 M, pH = 7.4, T= 25.0 °C).

It can be seen that, counterintuitively, the heavier Fn molecules adsorb with a faster diffusion-controlled kinetics, with respect to the slower kinetics of HSA adsorption. A minor effect can be seen to discriminate a slightly higher D value for HSA adsorption onto OTS, while as above indicated, Fn appears to diffuse faster to Hyl-SiO_2 surfaces.

The data of adsorbed mass at saturation and estimated diffusion coefficient are summarized in Table 1. It is to mention that, for both hydrophilic and hydrophobic surfaces, the measured D are about two or three order of magnitude lower than the bulk solution values reported, in similar conditions of pH (7.2), buffer and ionic force, for HSA (D_{bulk}= 6.4 x10^{-7} cm^2/s) [92] On the contrary, the measured D values for Fn are of the same order of the values reported in literature for this protein (D_{bulk} = 2.11x10^{-7} cm^2/s) [93].

Table 1. Adsorbed mass, Diffusion coefficients (D) and RSA affinity constant (k_a) for single and protein mixture on Hyl-SiO_2 and OTS surfaces by LSPR.

Protein	Surface	Mass (ng/cm^2)	D (cm^2/s)	k_a (cm/s)
HSA	Hyl-SiO_2	85±5[a]	(4.0±0.2[b])x10^{-10}	(1.7±0.2[c])x10^{-6}
	OTS	120±5	(3.6±0.1)x10^{-9}	(6.2±0.1)x10^{-6}
Fn	Hyl-SiO_2	430±5	(4.1±0.2)x10^{-7}	(6.6±0.3)x10^{-4}
	OTS	330±5	(9.1±0.3)x10^{-8}	(2.1±0.1)x10^{-4}
HSA + Fn	Hyl-SiO_2	450±5	(4.5±0.4)x10^{-8}	(1.1±0.1)x10^{-4}
	OTS	370±5	(7.2±0.5)x10^{-9}	(3.9±0.2)x10^{-5}

[a]Mean ± Standard deviation; experiment was performed in triplicate;

[b]Standard error of the linear regression slope; R^2>90%;

[c]Standard error of the Fit as derived from Nonlinear Least-square Fitting with Equation 38;

We suggest that the observed difference for HSA diffusion coefficient can be related with repulsive protein –surface interactions strongly reduce to the D values for the protein [94]. Indeed it should be pointed out that D represents an “effective” diffusion coefficient, reproducing the success of adsorption events, critically depending on the peculiar chemical and structural features of the adsorbent surfaces.

The second step of adsorption has been analysed according to the random sequential adsorption model (RSA) [91], based on the relationship between protein adsorption rate (dM/dt) and the protein adsorbed mass (M) shown below (see Figure 18 B):

$$\frac{dM}{dt} = mk_a C_b \left[1 + 0.812 \frac{Ma}{m\theta_\infty} + 0.4258 \left(\frac{Ma}{m\theta_\infty} \right)^2 + 0.0716 \left(\frac{Ma}{m\theta_\infty} \right)^3 \times \left(1 - \frac{Ma}{m\theta_\infty} \right)^3 \right] \qquad Eq.38$$

where m is the protein molecular weight, k_a is the adsorption rate constant, C_b is the protein concentration in the bulk solution and θ_∞=0.547 is the maximum coverage in the simplest hard spherical particle approximation, assuming a cubic packing [59].

The RSA analysis confirms the surprisingly higher efficiency of the Fn adsorption events, well represented by k_a values (in the range of 10^{-4} cm^2/s) which are about two order of magnitude higher than the ones estimated for HSA (in the range of 10^{-6} cm^2/s).

As the k_a term in the RSA model represents the effective interaction success, we may argue that the adsorption rate is controlled by the surface/protein interactions in the adopted experimental conditions. In particular, at the pH 7.4, both HSA and Fn are negatively charged, their isoelectric points being 4.7 and 5.5 [95] respectively, as well as SiO_2 and OTS surfaces at the same pH [83]. In this framework, the high ionic strength condition employed in the present experiments (0.1 M NaCl), determines an estimated Debye length lower than 0.8 nm [83], suggesting that for the smaller (and lighter) Albumin, electrostatic repulsion is significantly higher than for the larger (and heavier) Fn.

Further minor differences in k_a value are seen both for HSA adsorbed on OTS and Hyl-SiO_2 and for Fn onto Hyl-SiO_2 OTS (see Table 1), reflecting the fact that a detailed balance must be taken into account for the interaction of each protein with hydrophobic and hydrophilic surfaces.

In overall, D for the first step and k_a for the second can be assumed as the probability factors that any given protein-to-surface collision will result in an adsorption event, thus providing a “measure” of the adsorption efficiency. Moreover, for both surfaces, the affinity constants are homogeneously higher than the corresponding effective diffusion coefficient confirming that, in the present experimental conditions, the adsorption process occurs in a diffusion limited regime.

The above discussed higher efficiency of the Fn sticking process with respect to HSA suggests that this effect can be used to promote selective adsorption from complex protein mixture. Accordingly, the behaviour of a binary protein solution (HSA+Fn, 200 μg/ml) on both Hyl-SiO_2 and OTS has been studied, employing the very same experimental conditions employed for single protein solutions. As shown in Figure 19, it has been found that the protein binary solution essentially behaves as the pure Fn solution, with the heavier Fn preferentially adsorbing on both surfaces (see Table 1), also if, for both surfaces, the adsorption kinetic of Fn for the mixture is slower than the one measured for the single component solution (Figure 20), and reflected from the decrease of D and k_s (about a factor of 10).

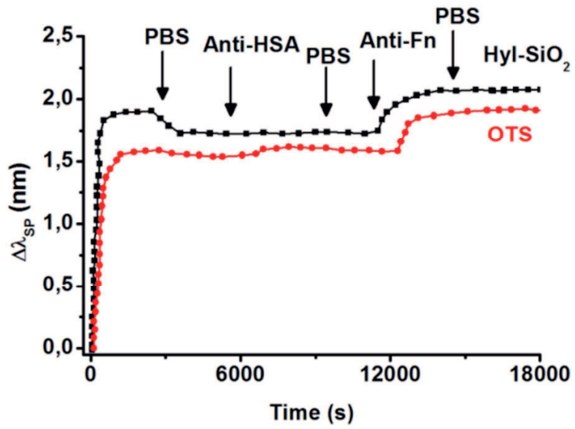

Figure 19. Competitive protein adsorption curves by LSPR for a binary solution of HSA + Fn (200 μg/ml, buffer PBS 0.01 M, pH = 7.4, T= 25.0 °C).

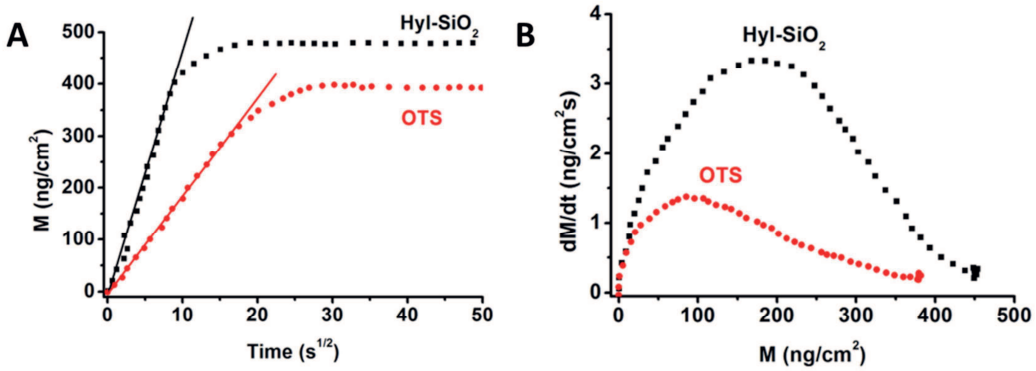

Figure 20. (A) Protein adsorbed mass (ng/cm^2) vs. square root of time (s$^{1/2}$) for the HSA and Fn mixture. The straight line fit of the 1st adsorption steps is shown for each curve. (B) Rate of adsorption as a function of deposited mass density for HSA and Fn mixture (200 μg/ml, buffer PBS 0.01 M, pH = 7.4, T= 25.0 °C).

Anyhow, the occurrence of the preferential fibronectin adsorption was further confirmed by testing the adsorbed protein layer with specific antibody conjugation. The results are reported in Figure 19, where a solution of specific HSA-antibody (Anti-HSA) is injected after the interaction of protein mixture with SiO_2 surface reaches saturation. In fact, no detectable increase of the LSPR signal is observed after the Anti-HSA addition, suggesting that is not present on Hyl-SiO_2 surfaces, while, on OTS surfaces a small response was measured after Anti-HSA injection, being completely removed during the rinsing step with buffer, suggesting that a mere unspecific adsorption occurred for the antibody molecules for hydrophobic surfaces. On the contrary, when the Fn antibody (Anti-Fn) solution was injected, a relevant adsorption step is measured on both surfaces, and no desorption was found after the buffer rinsing, suggesting that the Anti-Fn molecules are specifically conjugated. These effect suggests that a small amount of coadsorbed albumin may slow down the adsorption of Fn.

2.4 Conclusions

In summary, the dynamics of albumin and fibronectin “dry mass” adsorption from single and binary protein solutions, studied by taking profit of the capability of LSPR technique of providing the “real” protein adsorbed mass, show that surprisingly, i.e., in spite of its much higher molecular weight, fibronectin adsorbs faster and in larger amount than albumin on both hydrophilic and hydrophobic surfaces. According to the reported results, we surmise that this non-Vroman behaviour is driven by electrostatic factors, enhanced in the peculiar experimental conditions we used, i.e., pH 7.4 and relatively high ionic strength (NaCl 0.1M), disfavouring the adsorption of the smaller proteins, if the Debye length, in the peculiar conditions of the solution, is close to their radius of gyration, i.e., increasing the efficiency of the repulsive forces with surfaces of the same charge. Moreover, it turns out that the dynamics of competitive protein adsorption is in agreement with the hypothesis that the diffusion coefficients and the affinity constants obtained for single protein adsorption, remain also valid for binary solutions, i.e., there is no interfering effect of proteins in solutions, such as clustering or association.

In conclusion, the obtained results pave the way to the understanding of the behaviour of complex solutions onto hydrophilic/hydrophobic weakly charged surfaces.

2.5 References

1. J. K. Cheung, P. Shah, T. M. Truskett. Heteropolymer Collapse Theory for Protein Folding in the Pressure-Temperature Plane. Biophysical Journal 91 (2006) 2427–2435.
2. G. Singh. Chemistry of Amino-acids and Proteins. New Delhi: Discovery Publ. House, 2007, p.27.
3. M. J. Betts, R. B. Russell. Amino Acid Properties and Consequences of Substitutions. M. R. Barnes, I. C. Gray (Ed.). Bioinformatics for Geneticists. Chichester, England: Wiley, 2003.
4. P. D. Ross, S. Subramanian. Thermodynamics of Protein Association Reactions: Forces Contributing to Stability. Biochemistry 20 (1981) 3096-3102.
5. D. S. Berkholz, M. V. Shapovalov, R. L. Dunbrack, Jr., P. A. Karplus. Conformation Dependence of Backbone Geometry in Proteins. Structure 17 (2009) 1316–1325.
6. M. Diez, V. Petuya, L. A. Martínez-Cruz, A. Hernández. Insights into mechanism kinematics for protein motion simulation. BMC Bioinformatics 15 (2014) 184.
7. D. Eisenberg. The discovery of the α-helix and β-sheet, the principal structural features of proteins. PNAS 100 (2003) 11207–11210.
8. H. Lodish, A. Berk, S. L. Zipursky, et al. Molecular Cell Biology. 4th edition. New York: W. H. Freeman; 2000. Section 3.1, Hierarchical Structure of Proteins.
9. A. Poupon, J. P. Mornon. Populations of hydrophobic amino acids within protein globular domains: identification of conserved "topohydrophobic" positions. Proteins. 33 (1998) 329-342.
10. L. J Smith, K. M Fiebig, H. Schwalbe, C. M. Dobson. The concept of a random coil. Residual structure in peptides and denatured proteins. Folding and Design 1 (1996) R95-R106.
11. I. M. Klutz, N. R. Langermann, D. W. Darnall. Quaternary structure of proteins. Annual Review of Biochemistry 39 (1970) 25-62.
12. M. Möddel, M. Bachmann, W. Janke. Conformational Mechanics of Polymer Adsorption Transitions at Attractive Substrates. J. Phys. Chem. B 113 (2009) 3314–3323.
13. T. X. Hoang, L. Marsella, A. Trovato, F. Seno, J. R. Banavar, A. Maritan. Common attributes of native-state structures of proteins, disordered proteins, and amyloid. PNAS 103 (2006) 6883–6888.
14. H. Neurath, J. P. Greensteis, F. W. Putnam, J. A. Ericksox. The Chemistry Of Protein Denaturation. Chem. Rev. 34 (1944) 157–265.
15. P. A. Fields. Review: Protein function at thermal extremes: balancing stability and flexibility. Comparative Biochemistry and Physiology Part A 129 (2001) 417-431.
16. C. N. Pace, S. Treviño, E. Prabhakaran, J. M. Scholtz. Protein structure, stability and solubility in water and other solvents. Phil. Trans. R. Soc. Lond. B 359 (2004) 1225–1235.
17. M. D. Shoulders, R. T. Raines. Collagen Structure and Stability. Annu Rev Biochem. 78 (2009) 929–958.

18. N. Ul. Isoelectric points and conformation of proteins: I. Effect of urea on the behavior of some proteins in isoelectric focusing. Biochimica et Biophysica Acta (BBA) - Protein Structure 229 (1971) 567-581.
19. E. Seyrek, P. L. Dubin, C. Tribet, E. A. Gamble. Ionic Strength Dependence of Protein-Polyelectrolyte Interactions. Biomacromolecules 4 (2003) 273-282.
20. V. Hlady, J. Buijs. Protein adsorption on solid surfaces. Curr Opin Biotechnol. 7 (1996) 72–77.
21. M. Karlsson, J. Ekeroth, H. Elwing, Uno Carlsson. Reduction of Irreversible Protein Adsorption on Solid Surfaces by Protein Engineering for Increased Stability. The Journal of Biological Chemistry 280 (2005) 25558-2564.
22. J. J. Gray. The interaction of proteins with solid surfaces. Current Opinion in Structural Biology 14 (2004) 110–115.
23. R. G. Compton, G. Hancock. Applications of Kinetic Modelling. Amsterdam: Elsevier, 1999, p 135.
24. D. W. Bolen, G. D. Rose. Structure and Energetics of the Hydrogen-Bonded Backbone in Protein Folding. Annual Review of Biochemistry 77 (2008) 339-362.
25. Hubbard, Arthur T. Encyclopedia of Surface and Colloid Science, Vol.1 . New York: Marcel Dekker, 2002, pp 280-281.
26. F. Despa, R. S. Berry. The Origin of Long-Range Attraction between Hydrophobes in Water. Biophys J. 92 (2007) 373–378.
27. R. D. Tilton, C. R. Robertson, A. P. Gast. Manipulation of Hydrophobic Interactions in Protein Adsorption. Langmuir 7 (1991) 2710-2718.
28. R. A. Hartvig, M. van de Weert, J. Østergaard, L. Jorgensen, H. Jensen. Protein Adsorption at Charged Surfaces: The Role of Electrostatic Interactions and Interfacial Charge Regulation. Langmuir 27 (2011) 2634–2643.
29. J.R. Sharpe, R.L. Sammons, P.M. Marquis. Effect of pH on protein adsorption to hydroxyapatite and tricalcium phosphate ceramics. Biomaterials 18 (1997) 471-476.
30. T. Kopac, , K. Bozgeyik, J. Yener. Effect of pH and temperature on the adsorption of bovine serum albumin onto titanium dioxide. Colloids and Surfaces A: Physicochemical and Engineering Aspects 322 (2008) 19-28.
31. C. J. Van Oss, M. K. Chaudhury, R. J. Good. Interfacial Lifshitz-van der Waals and Polar Interactions in Macroscopic Systems. Chem. Rev. 88 (1988) 927-941.
32. Y.Liang, N. Hilal, P. Langston, V. Starov. Interaction forces between colloidal particles in liquid: Theory and experiment. Advances in Colloid and Interface Science 134–135 (2007) 151–166.
33. H. Wang, B. Zhang Newby. Applicability of the extended Derjaguin–Landau–Verwey–Overbeek theory on the adsorption of bovine serum albumin on solid surfaces. Biointerphases. 9 (2014) 041006.
34. D. Leckband, S. Sivasankar. Forces controlling protein interactions: theory and experiment. Colloids and Surfaces B: Biointerfaces 14 (1999) 83–97.
35. J. Shen, T. Wu, Q. Wang, H. Pan. Molecular simulation of protein adsorption and desorption on hydroxyapatite surfaces. Biomaterials 29 (2008) 513–532.

36. R. D. Tilton, A. P. Gast, C. R. Robertson. Surface diffusion of interacting proteins. Effect of concentration on the lateral mobility of adsorbed bovine serum albumin. Biophysical Journal 58 (1990) 1322-1326.
37. C. Calonder, Y. Tie, P. R. Van Tassel. History dependence of protein adsorption kinetics. PNAS 98 (2001) 10664–10669.
38. K. L. Jones, C. R. O'Melia. Protein and humic acid adsorption onto hydrophilic membrane surfaces: effects of pH and ionic strength. Journal of Membrane Science 165 (2000) 31–46.
39. I. Kiesel, M. Paulus, J. Nase, S. Tiemeyer, C. Sternemann, K. Rüster, F. J. Wirkert, K. Mende, T. Büning, M. Tolan. Temperature-Driven Adsorption and Desorption of Proteins at Solid−Liquid Interfaces. Langmuir 30 (2014) 2077−2083.
40. M. Malmsten. Protein adsorption at the solid-liquid interface. Lvov, Yuri, and Helmut Möhwald (Ed.). Protein Architecture: Interfacing Molecular Assemblies and Immobilization Biotechnology. New York: Dekker, 2000.
41. T. V. Chalikian. Volumetric Properties of Proteins. Annual Review of Biophysics and Biomolecular Structure 32 (2003) 207-235.
42. N. L. Burns. Measurements of Electro-Osmosis as a Method for Electrokinetic Surface Analysis. A. J. Milling (Ed.), Surface Characterization Methods: Principles, Techniques, and Applications. New York: Marcel Dekker, 1999, pp 138-139.
43. J. Hladílková, T. H. Callisen, M. Lund. Lateral Protein−Protein Interactions at Hydrophobic and Charged Surfaces as a Function of pH and Salt Concentration. J. Phys. Chem. B 120 (2016) 3303−3310.
44. M. Muthukumar. Communication: Charge, diffusion, and mobility of proteins through nanopores. The Journal of Chemical Physics 141(2014) 081104.
45. A. S. Parmar, M. Muschol. Hydration and Hydrodynamic Interactions of Lysozyme: Effects of Chaotropic versus Kosmotropic Ions. Biophysical Journal 97 (2009) 590–598.
46. D. R. Schmidt, H. Waldeck, W. J. Kao. Protein adsorption to biomaterials. Puleo, David A., and Rena Bizios (Ed.). Biological Interactions on Materials Surfaces: Understanding and Controlling Protein, Cell, and Tissue Responses. Dordrecht: Springer, 2009, pp 7-8.
47. W. Norde, C. E. Giacomelli. BSA structural changes during homomolecular exchange between the adsorbed and the dissolved states. J Biotechnol. 79 (2000) 259-68.
48. M. M. Ouberai, K. Xu, M. E. Welland. Effect of the interplay between protein and surface on the properties of adsorbed protein layers. Biomaterials 35 (2014) 6157–6163.
49. W. Norde, J. Lyklema. Interfacial behaviour of proteins, with special reference to immunoglobulins. A physicochemical study. Adv. Colloid Interface Sci. 179-182 (2012) 5−13.
50. H. Lei, M. Wang, Z. Tang, Y. Luan, W. Liu, B. Song, H. Chen. Control of Lysozyme Adsorption by pH on Surfaces Modified with Polyampholyte Brushes. Langmuir 30 (2014) 501–508.
51. J. T. Kim, N. Weber, G. H. Shin, Q. Huang, S. X. Liu. The study of beta-lactoglobulin adsorption on polyethersulfone thin film surface using QCM-D and AFM. J. Food Sci. 72 (2007) E214-E221.

52. T. Zoungrana, W. Norde. Thermal stability and enzymatic activity of α-chymotrypsin adsorbed on polystyrene surfaces. Colloids and Surfaces B: Biointerfaces 9 (1997) 157-167.
53. L. Xua, C. A. Siedlecki. Effects of surface wettability and contact time on protein adhesion to biomaterial surfaces. Biomaterials 28 (2007) 3273–3283.
54. M. Feng, A. Berdugo Morales, T. Beugeling, A. Bantjes, K. van der Werf, G. Gosselink, B. de Grooth, J. Greve. Adsorption of High Density Lipoproteins (HDL) on Solid Surfaces. Journal of Colloid and Interface Science 177 (1996) 364-371.
55. F. Grinnell, M. K. Feld. Fibronectin Adsorption on Hydrophilic and Hydrophobic Surfaces Detected by Antibody Binding and Analyzed during Cell Adhesion in Serum-containing Medium. The Journal of Biological Chemistry 257 (1982) 4888-4893.
56. R. A. Latour. The Langmuir isotherm: a commonly applied but misleading approach for the analysis of protein adsorption behavior. J Biomed Mater Res A. 103 (2015) 949-958.
57. P. Schaaf, J.-C. Voegel, B. Senger. Irreversible deposition/adsorption processes on solid surfaces. Ann. Phys. Fr. 23 (1998) 1-89.
58. R. Artali, A. Del Pra, E. Foresti, I. G. Lesci, N. Roveri, P. Sabatino. Adsorption of human serum albumin on the chrysotile surface: a molecular dynamics and spectroscopic investigation. J R Soc Interface 5 (2008) 273–283.
59. F. M. Richards. Areas, volumes, packing and protein structure. Annu Rev Biophys Bioeng. 6 (1977) 151-176.
60. P. Viot, G. Tarjus, S. M. Ricci, J. Talbot. Random sequential adsorption of anisotropic particles. I. Jamming limit and asymptotic behavior. J. Chem. Phys. 97 (1992) 5212-5218.
61. J. J. Ramsden. Observation of anomalous diffusion of proteins near surfaces. J. Phys. Chem. 96 (1992) 3388–3391.
62. Q. Song. Protein Adsorption in Microengraving Immunoassays. Sensors 15 (2015) 26236–26250.
63. P. Schaaf , J. Talbot. Kinetics of Random Sequential Adsorption. Physical Review Letters 62 (1989) 175-178.
64. B. J. Cowsill, P. D. Coffey, M. Yaseen, T. A. Waigh, N. J. Freeman, J. R. Lu. Measurement of the thickness of ultra-thin adsorbed globular protein layers with dual-polarisation interferometry: a comparison with neutron reflectivity. Soft Matter 7 (2011) 7223-7230.
65. N. Giamblanco, G. Zhavnerko, N. Tuccitto, A. Licciardello, G. Marletta. Coadsorption-dependent orientation of fibronectin epitopes at hydrophilic gold surfaces. Soft Matter 8 (2012) 8370-8378.
66. M. A. Brusatori, Y. Tie, P.R. Van Tassel. Protein Adsorption Kinetics under an Applied Electric Field: An Optical Waveguide Lightmode Spectroscopy Study. Langmuir 19 (2003) 5089-5097.
67. J. J. Ramsden, J. E. Prenosil. Effect of Ionic Strength on Protein Adsorption Kinetics. J. Phys. Chem., 98 (1994) 5376–5381.
68. F. Höök, J. Vörös, M. Rodahl, R. Kurrat, P. Böni, J.J. Ramsden, M. Textor, N.D. Spencer, P. Tengvall, J. Gold, B. Kasemo. A comparative study of protein adsorption on titanium oxide surfaces using in situ ellipsometry, optical waveguide lightmode spectroscopy, and quartz crystal microbalance/ dissipation, Colloids and Surfaces B: Biointerfaces 24 (2002) 155-170.

69. J. Voros. The Density and Refractive Index of Adsorbing Protein Layers, Biophysical Journal, 87 (2004) 553-561.
70. M. F. Mora , J. L. Wehmeyer, R. Synowicki, C. D. Garcia. Investigating Protein Adsorption via Spectroscopic Ellipsometry, in D.A. Puleo and R. Bizios (eds.), Biological Interactions on Materials Surfaces, Springer Science + Business Media, New York, 2009, pp.19-41
71. G. Diaconu, T. Schäfer. Study of the interactions of proteins with a solid surface using complementary acoustic and optical techniques. Biointerphases 9 (2014) 029015.
72. R. Konradi, M. Textor, E. Reimhult. Using Complementary Acoustic and Optical Techniques for Quantitative Monitoring of Biomolecular Adsorption at Interfaces. Biosensors 2 (2013) 341-376.
73. J. L. Jordan, E. J. Fernandez. QCM-D Sensitivity to Protein Adsorption Reversibility. Biotechnology and Bioengineering 101 (2008) 837-842.
74. A. Laschitsch, B. Menges, and D. Johannsmann. Simultaneous determination of optical and acoustic thicknesses of protein layers using surface plasmon resonance spectroscopy and quartz crystal microweighing. Applied Physics Letters 77 (2000) 2252-2254.
75. J. Malmström, H. Agheli, P. Kingshott, D. S. Sutherland. Viscoelastic Modeling of Highly Hydrated Laminin Layers at Homogeneous and Nanostructured Surfaces: Quantification of Protein Layer Properties Using QCM-D and SPR. Langmuir 23 (2007) 9760-9768.
76. C. R. Wittmera, J. A. Phelpsa, W. M. Saltzmanb, P. R. Van Tassel. Fibronectin Terminated Multilayer Films: Protein Adsorption and Cell Attachment Studies. Biomaterials 28 (2007) 851–860.
77. A. J. Haes, R. P. Van Duyne. A unified view of propagating and localized surface plasmon resonance biosensors. Anal Bioanal Chem 379 (2004) 920–930.
78. K. A. Willets, R. P. Van Duyne. Localized Surface Plasmon Resonance Spectroscopy and Sensing. Annu. Rev. Phys. Chem. 58 (2007) 267–297.
79. K. A. Willets, R. P. Van Duyne. Localized Surface Plasmon Resonance Spectroscopy and Sensing. Annu. Rev. Phys. Chem. 58 (2007) 267–297.
80. H. Fredriksson, Y. Alaverdyan, A. Dmitriev, C. Langhammer, D.S. Sutherland, M. Zäch, B. Kasemo, Hole–Mask Colloidal Lithography. Adv. Mater. 19 (2007) 4297–4302.
81. Jonsson, M. P; Jönsson, P; Höök, F. Simultaneous Nanoplasmonic and Quartz Crystal Microbalance Sensing: Analysis of Biomolecular Conformational Changes and Quantification of the Bound Molecular Mass. Anal. Chem. 80 (2008) 7988–7995.
82. C. T. McKee, W. A. Ducker. Refractive Index of Thin, Aqueous Films between Hydrophobic Surfaces Studied Using Evanescent Wave Atomic Force Microscopy. Langmuir 21 (2005) 12153-12159.
83. M. Bellion, L. Santen, H. Mantz, H. Hähl, A. Quinn, A. Nagel, C. Gilow, C. Weitenberg, Y. Schmitt, K. Jacobs. Protein adsorption on tailored substrates: long-range forces and conformational changes. J. Phys.: Condens. Matter 20 (2008) 404226.
84. J. Benesch , A. Askendal, P. Tengvall. Quantification of adsorbed human serum albumin at solid interfaces: a comparison between radioimmunoassay (RIA) and simple null ellipsometry. Colloids and Surfaces B: Biointerfaces 18 (2000) 71–81.

85. K. Rechendorff, M. B. Hovgaard, M. Foss, V. P. Zhdanov, F. Besenbacher. Enhancement of Protein Adsorption Induced by Surface Roughness. Langmuir 22 (2006) 10885–10888.
86. C. F. Wertz, M. M. Santore. Adsorption and Relaxation Kinetics of Albumin and Fibrinogen on Hydrophobic Surfaces: Single-Species and Competitive Behavior. Langmuir 15 (1999) 8884-8894.
87. J. B. Lhoest, E. Detrait, P. van den Bosch de Aguilar, P. Bertrand. Fibronectin adsorption, conformation, and orientation on polystyrene substrates studied by radiolabeling, XPS, and ToF SIMS. J Biomed Mater Res. 41 (1998) 95-103.
88. N. Giamblanco, M. Yaseen, G. Zhavnerko, J. R. Lu, and G. Marletta. Fibronectin Conformation Switch Induced by Coadsorption with Human Serum Albumin. Langmuir 27 (2011) 312–319.
89. U. Klueh, T. Seery, D.G. Castner, J.D. Bryers, D.L. Kreutzer. Binding and orientation of fibronectin to silanated glass surfaces using immobilized bacterial adhesin-related peptides. Biomaterials 24 (2003) 3877–3884.
90. J. J. Ramsden. Observation of Anomalous Diffusion of Proteins Near Surfaces. J. Phys. Chem. 96 (1992) 3388-3391.
91. R. Lu, Q. Li, T. H. Nguyen. Random sequential adsorption of human adenovirus 2 onto polyvinylidene fluoride surface influenced by extracellular polymeric substances. Journal of Colloid and Interface Science 466 (2016) 120–127.
92. A. E. Kamholz, B. H. Weigl, B. A. Finlayson, P. Yager. Quantitative Analysis of Molecular Interaction in a Microfluidic Channel: The T-Sensor. Anal. Chem. 71 (1999) 5340-5347.
93. M. Rocco, M. Carson, R. Hantgan, J. McDonagh, J. Hermans. Dependence of the shape of the plasma fibronectin molecule on solvent composition. Ionic strength and glycerol content. J Biol Chem 258 (1983) 14545–14549.
94. E. P. Vieira, S. Rocha, M. C. Pereira, H. Möhwald, M. A. N. Coelho. Adsorption and Diffusion of Plasma Proteins on Hydrophilic and Hydrophobic Surfaces: Effect of Trifluoroethanol on Protein Structure. Langmuir 2009, 25(17), 9879–9886.
95. M. Tagaya, T. Ikoma, N. Hanagata, T. Yoshioka, J. Tanaka. Competitive adsorption of fibronectin and albumin on hydroxyapatite nanocrystals. Sci. Technol. Adv. Mater. 12 (2011) 034411- 034416.

CHAPTER 3.

KINETIC DISCRIMINATION OF DNA SINGLE-BASE MUTATIONS

3.1 Introduction

3.1.1 Single base mutation in DNA: clinical relevance and detection methods

The diploid human genome including twenty three pairs of chromosomes is composed of 20–25 thousand genes; haploid set is estimated to be $3.2*10^9$ base pairs [1]. One member of each chromosome is received from the father, and the other member of the pair is transmitted through maternal lineage. DNA is made up of four base pairs adenine, thymine, cytosine and guanine abbreviated as A, T, C, and G, respectively. Genes consisting of DNA base pairs are located on chromosomes. A gene is a sequence of base pairs that produces a functional product including a RNA molecule or subsequently a peptide. An allele is positioned on a locus, the specific location of a gene or DNA sequence on a chromosome; so the diploid genome contains two alleles of each gene. Chromosomes 1 to 22 are called autosomes and the twenty-third pair is the sex chromosomes, i.e. X and Y [2].

Steps in the transmission of genetic information include replication (DNA makes DNA), transcription (DNA makes RNA), RNA processing (capping, splicing, tailing and RNA translocation to cytoplasm), translation (RNA makes protein), and protein processing, folding, transport and incorporation [3]. If the DNA sequence is mutated and the alteration is not repaired by the cell, subsequent replications reproduce the mutation. A variety of mechanisms can cause mutations ranging from a single nucleotide alteration to the loss, duplication or rearrangement of chromosomes [4].

Among these, single base alteration are the most common form of human sequence variation and occur approximately once every 300-1000 nucleotides [5]. If the frequency of one of these variations is lower than one percent, the variation is usually called mutation, if higher it can be classified as polymorphism [6]. It is common to refer to polymorphism as a variation in the DNA sequence that generally does not cause debilitating diseases but could underlie differences in our susceptibility to a disease [7]. A polymorphism involving only one nucleotide in the gene sequence is called single nucleotide polymorphism (SNP) and its detection in a real sample is one of the most challenging and impressive results in clinical diagnostics, being SNPs involved in many diseases and in biological metabolisms [8]. In many cases specific SNPs can be related to drug response and toxicity: if the involved gene codes for an enzyme or a transporter then the activity of the protein can be adjusted or inhibited by the variation [9]. This can turn both into a reduced capacity of the involved biological process to absorb the drug, lowering its pharmacological effect on the patient or, counter, into a too rapid metabolization of the drug leading to a loss of its efficacy [10]. For drug response, the most common SNP is found in glutathione S-transferase P1 or xereoderma pigmentosum group D enzymes

for the activity of oxaliplatin [11]. Some other SNPs are related to responses to anticancer drugs activity, as for point mutation in the Kirsten Rat Sarcoma viral oncogene homologous (KRAS) gene codon 12, 13, and 61 that has been demonstrated to be associated with the development of certain pancreatic and lung cancers [12] and their detection is critical for the selection of the appropriate type of treatment [13]. Therefore, the screening of patients' genome coupled to the mapping of specific SNPs is a target of relevance for theranostic approach aiming to the development of a personalized medicine also with tailored therapies.

Until today the most used technologies designed to reveal SNPs are based on the principle of allele-specific hybridization, relying on the ability of oligonucleotide probes to bind selectively to DNA target sequences [14]. DNA microarrays via surface are based on oligonucleotide probes immobilized on the chip surface. Typically, the DNA chips require expensive fabrication processes [15, 16]. However, the most notable limitations are associated with the employed detection method. Indeed, the highly sensitive nature of hybridization assays with single base discriminatory capabilities requires a comparably sensitive detection method to reveal the small changes in analytical signal produced by a single nucleotide mismatch, which produces difference of melting temperature (T_m), less than 3 °C [17]. DNA hybridization was conducted on sensing systems based on unnatural probes having lower binding affinity during hybridization resulting in a decline of Tm up to 15°C and inducing a high sequence specificity [18]. The discrimination of one or more mismatches was generally accomplished by adjusting the hybridization conditions such as temperature, ionic strength, formamide concentration, or other dissociation conditions of the probe and target duplex [19]. Despite significant developments obtained by using various nanomaterials-based SNP assays coupled with a number of different readout strategies, the more important limitation for SNP analysis remains the quantification of extremely low abundance SNPs in an overwhelming background of wild-type genes in clinical settings [20]. Moreover, numerous statistical models have been created to evaluate the hybridization of nucleic acid targets using end-point analysis [21]. Additionally, several authors have proposed mechanistic models of single-component hybridization combining mass transport of target and chemical interactions on the surface of the array [22]. Their efforts resulted in an emerging consensus theoretical approach, which addresses the effects of three-dimensional and two-dimensional (surface-bound) mass transport, and surface chemistry, i.e., probe interactions, probe density, and steric hindrances by introducing efficient (or apparent) rate constants or more complicated rate functional parameters. However, all of these studies use a single analyte case for building the models, which limits their applicability in interpreting multi-component mixture, while only a few reports deal with the discrimination problems in mixed DNA targets solutions [23].

In this respect, many conventional SPR-based methods have been developed for SNP sensing, aiming to set direct, label-free detection strategies [24], i.e. avoiding the use of additional biomolecules (i.e. proteins, enzyme, etc.), nanoparticles or intercalating agents to discriminate single base mismatch target. This in view of skipping the drawbacks due to enzyme and protein interference with DNA hybridization [25] or with NPs possible aggregation on the sensing surfaces, thus preventing the further use of the sensor [26].

In the last year, sensors based on localized surface plasmon resonance (LSPR), recently have been subjected to a great scientific interest as an alternative technique to the conventional optical SPR [27]. Indeed LSPR technique allows to take profit from two peculiar features of the sensor structure. In particular, at first one may take advantage from the peculiar configuration of LSPR sensors, consisting in an array of gold nanostructures deposited on a glass substrate, allowing to overcome the critical problem, affecting both SPR and OWLS technique, of the long range sensitivity to the changes in the refractive index extending far away into the solution. In fact, the gold nanostructure employed in the LSPR experiment allows to confine the sensitivity to the medium refractive index changes to 5-30 nanometers into the solution. This enhances in a peculiar way the sensitivity to the refractive index changes at the very interface between nanodisks and solution [28].

Secondly, the possibility of using uncovered gold nanostructures distributed onto a SiO_2 surface enables to take profit of the simple thiol chemistry to bind DNA to the surface. In the case of SiO_2 sensing surface of OWLS the surface modification technique are the classical and more complex ones based on [29] a variety of saccharides (such as dextran, gelatin, heparin, etc.) or biomolecules (biotin, streptavidin, etc.) via covalent coupling to silanized waveguides, for example. Different terminal functionalities, such as amine, hydroxyl or carboxyl are also available and allow the further modification of the sensor surface if required by the application.

Analogous to SPR, LSPR can be exploited for biosensing applications, as the wavelength is highly dependent on the refractive index of the surrounding media [30]. The binding on the surface of the nanostructures results in a refractive index change, causing a shift in the extinction peak wavelength, λ_{max}. However, few reports are found in the literature about the application of LSPR sensors for nucleic acids detection [29, 31].

In this work, we develop a single nucleotide mismatch detection method, relevant to KRAS-related pathologies, based on the rapid DNA hybridization process in binary solution. Our approach involves thiolated single strand oligonucleotides immobilized on the nanostructured LSPR sensors, able to reveal the refractive index changes following the DNA hybridization processes. In particular, we have explored the effect of perfect and mismatch target concentration and its time dependence on the sensing performances in a two-component system. The hybridization rate constants for 93–mer sequences are determined for PM and a single nucleotide polymorphism (SNP) mismatch, at a well-defined ionic strength. Additionally, the dynamics of the two-component system versus a single-component system are analyzed, suggesting that the intensity of the relative LSPR signal at a fixed time provides an useful metric to quantify the MM strands fraction in PM-MM binary solutions, i.e., the possibility of using the time response to reveal the presence of single base polymorphism.

3.1.2. DNA hybridization at surface:

mechanism of interaction and kinetic models

Hybridization of DNA involves the formation of a doublestranded DNA (dsDNA) complex formed by two complementary single stranded DNA (ssDNA) molecules [32]. The structural stability of this complex is a result of hydrogen bonding and base-stacking interactions. Complementary base-pairs engage in two hydrogen bonds for adenine and thymine contacts, whereas three hydrogen bonds are involved in the formation of cytosine and guanine contacts. DNA hybridization usually occurs between an oligonucleotide with a known sequence (probe) and an unknown complementary strand of nucleic acid from solution (target) [32].

Generally, nucleic acid hybridization can be performed under two major strategies, that is, hybridization of DNA or RNA targets to surface-tethered oligonucleotide probes (solid-phase hybridization) [33] and hybridization of the target nucleic acids to randomly distributed probes in solution (solution-phase hybridization) [34]. Since various technologies rely on measurements of surface hybridization to sequence DNA, to detect DNA polymorphism, for DNA mapping, and to detect DNA mutation, it is of fundamental and technological interest to understand the actual process through which two ssDNA strands hybridize [35]. So far, several attempts have been made to formulate the behavior of DNA hybridization on the solid surface; nevertheless, a comprehensive model that demonstrates this behavior has not yet been developed [36].

Classical models that describe the rate of surface hybridization based on a combination of “specific adsorption” (direct adsorption to immobilized nucleotides) and “nonspecific adsorption” (adsorption to the surface and subsequent surface transport) have been described [37]. In these models, target molecules may nonspecifically adsorb to the surface and undergo a two- dimensional search of the surface for an immobilized complement. Also, the target molecules may adsorb. Within this family, the Langmuir isotherm [38] is the simplest and the most frequently used. This adsorption model makes several assumptions:

- The total amount of target oligonucleotides in the hybridization solution is always higher than the amount of immobilized probes. Thus, the concentration of target is assumed to be constant.
- The hybridization system reaches its equilibrium.
- The adsorbate [target] covers the surface up to complete coverage as a monolayer on the substrate (adsorbent).
- There are no adsorbate - adsorbate [target-target] interactions on the surface of the host substrate.
- On the substrate all binding sites are equivalent.

Accordingly, the hybridization process can be described as a simple bimolecular binding reaction. Therefore, the hybridization process can be described by two chemical equations. A free single-

stranded target in the solution (*P*) binds to oligonucleotide probe immobilized at the surface (*T*) with rate k_a, forming the corresponding DNA hybrid (PT) [39]:

$$P + T \xrightarrow{k_a} PT \qquad Eq.39$$

This DNA hybrid dissociates to initial components with a rate k_d [40]:

$$PT \xrightarrow{k_d} P + T \qquad Eq.40$$

Let *x* be the concentration of RNA target, t the time of the reaction, k_a be the rate of forward reaction of forming the duplex and $\vartheta(t)$ be the fraction of sites occupied by probe-target duplexes. Assume:

- (Adsorption) Target DNA attaches to probes at a rate $k_a(1-\theta(t))$, proportional to the concentration of specific target DNA and the fraction of unoccupied probes;
- (Desorption) Target DNA detaches from probes at a rate $k_d\theta(t)$, proportional to the fraction of occupied probes.

Then,

$$\frac{d\theta(t)}{dt} = k_a c_0(1-\theta(t)) - k_d\theta(t) \qquad Eq.41$$

with c_0 being the concentration of the target-DNA in solution used in the experiment.
The solution with the initial condition $\theta(0) = 0$ is

$$\theta(t) = \frac{k_a c_0}{k_a c_0 + k_d}\left[1 - e^{-(k_a c_0 + k_d)t}\right] \qquad Eq.42$$

Let $y(c_0,t)$ be the generic instrumental response assumed proportional to $\theta(t)$, and let y_0 be the background signal at zero concentration, then

$$y(c_0,t) = y_0 + \frac{k_a c_0 b}{k_a c_0 + k_d}\left[1 - e^{-(k_a c_0 + k_d)t}\right] \qquad Eq.43$$

where *b* is the constant of proportionality between $y(c_0,t)$ and $\theta(t)$.
The equilibrium limit, $t \to \infty$, gives the Langmuir isotherm [41]:

$$y(c_0) = y_0 + \frac{k_a c_0 b}{k_a c_0 + k_d} \qquad Eq.44$$

Nevertheless experimental data for hybridization from single (pure) target solution has been demonstrated to be nicely fitted by the simple Langmuir model [41], real DNA sample, generally,

consisting of a mixture of targets require a more complex kinetics model. In literature, an expanded Langmuir model has been proposed to model the kinetics, i.e., the association and dissociation processes between a single type of probe at the surface and a binary mixed solution of oligonucleotide targets competing for the same binding sites, however, with different affinities [42]. Assuming the hybridization of two distinct target is simultaneous, it can be described in the following way: the total surface coverage, $\theta^{tot}(t)$, has two components, $\theta^{p}(t)$, describing probe sites occupied by the first target component (labeled p), and $\theta^{q}(t)$ describing those occupied by the second component (labeled q). Then

$$\frac{d\theta^{tot}(t)}{dt} = c_0^p k_a^p (1-\theta(t)) + c_0^q k_a^q (1-\theta(t)) - k_d^p \theta^p(t) - k_d^q \theta^q(t) \qquad Eq.\,45$$

with $\theta^{tot}(t) = \theta^{p}(t) - \theta^{q}(t)$.

The solution of this differential equation is given by

$$\theta^{tot}(t) = \frac{c_0^p k_a^p}{c_0^p k_a^p + c_0^q k_a^q + k_d^p} \times \left[1 - e^{\left\{-\left(c_0^p k_a^p + c_0^q k_a^q + k_d^p\right)t\right\}}\right] + \frac{c_0^q k_a^q}{c_0^p k_a^p + c_0^q k_a^q + k_d^d} \times \left[1 - e^{\left\{-\left(c_0^p k_a^p + c_0^q k_a^q + k_d^d\right)t\right\}}\right] \qquad Eq.\,46$$

$\theta^{tot}(t)$ is proportional to the instrumental response , $y\left(c_0^p, c_0^q, t\right)$, therefore the result of the kinetic experiments with a single probe layer and a mixed target solution can be fitted by

$$y\left(c_0^p, c_0^q, t\right) = \frac{c_0^p k_a^p b}{c_0^p k_a^p + c_0^q k_a^q + k_d^p} \times \left[1 - e^{\left\{-\left(c_0^p k_a^p + c_0^q k_a^q + k_d^p\right)t\right\}}\right] + \frac{c_0^q k_a^q b}{c_0^p k_a^p + c_0^q k_a^q + k_d^d} \times \left[1 - e^{\left\{-\left(c_0^p k_a^p + c_0^q k_a^q + k_d^d\right)t\right\}}\right] \quad Eq.\,47$$

where *b* is assumed to be the constant of proportionality between $y\left(c_0^p, c_0^q, t\right)$ and $\theta^{tot}(t)$.

3.2 Materials and methods

3.2.1 Materials

All DNA strands were obtained from Purimex (Grebenstein, Germany) in double HPLC-purified grade. Synthetic oligonucleotide sequences for probes and targets are listed in Table S1 of the supporting information. The 5'-thiol-modified probe solutions consisting of a 35-nucleotide long single strand DNA (ssDNA) sequence (henceforth indicated as probe) (-CTA-) were prepared by diluting to a final concentration of 300 nM in 0.1 M PBS and stored at 5°C. KRAS target length is chosen to be 93-mer to mimic the PCR length sequence target and in order to minimize possible secondary structure, which can lead to inhibited probe-target hybridization and diminished sensitivity of the assay as well as minimizing possible regions where the probes can bind nonspecifically [43]. The chosen targets are the perfect match (PM) (-TAG-), and the mismatch, (MM) (-GCT-) presenting the single base mutation in the central part. The pure target solutions were prepared at various concentrations ranging from 10 nM to 170 nM. The deionized water was purified using a Millipore filtration system and used in all experiments. All measurements were performed in 0.1M phosphate buffered saline (PBS, pH 7.4) at room temperature. Target solutions were thermally denatured 2 min and snap cooled 3 min, in order to obtain single-stranded targets before using for the LSPR experiments.

3.2.2 LSPR instrumentation

LSPR measurements are performed in optical transmission mode by using an Insplorion XNano instrument (Insplorion AB, Göteborg, Sweden). A detailed description of the operating principle of LSPR is reported in literature [44].

Briefly, a white light beam entered the measurement chamber, passed through the sensor chip (~4 mm^2 circular spot), and exited through a quartz glass window. The transmitted light is collected by a spectrophotometer, and data analysis is performed with the Insplorer software package (Insplorion AB). The time resolution is 1 Hz. The spectral resolution of the plasmon resonance is determined by high-order polynomial fitting, and the centroid position is calculated from the fit [45]. In this study two different types of sensor chip, both purchased from Insplorion AB, have been used. The first type consists of a glass slide decorated with gold nanodisks, prepared by hole-mask colloidal lithography [46] (see Figure. 21 A for an AFM image of the sensor surface). This method yields a partly random distribution of nanostructures on the substrate, which combined with a large particle-particle separation, eliminates both far and near field coupling between the particles so that the measured optical signal reflects the optical (LSPR) response of a single particle [47]. The second type of sensor has a further silicon oxide film (thickness ~10 nm) deposited on top of gold nanodisks by a plasma enhanced chemical vapor deposition (PECVD) technique (Insplorion AB).

The individual gold nanodisk has an average height and diameter of 24±2 nm and 118±5 nm, respectively as indicated by the data of section analysis performed by atomic force microscopy (AFM)

technique with Nanoscope IIIa controller (Digital Instrument, Veeco, USA) (see Figure 21 B). The surface coverage is 9 disks per μm^2 (~7% of total area) and the average particle pitch is 330±30 nm.
The bulk sensitivity of the gold nanodisks is 210±17 nm per refractive index unit based on a series of measurements performed using water/ethanol mixtures (data not shown). The measured sensitivity is in line with previous data by other authors [48] it was concluded that the sensitivity is sufficiently high for biosensing purposes.

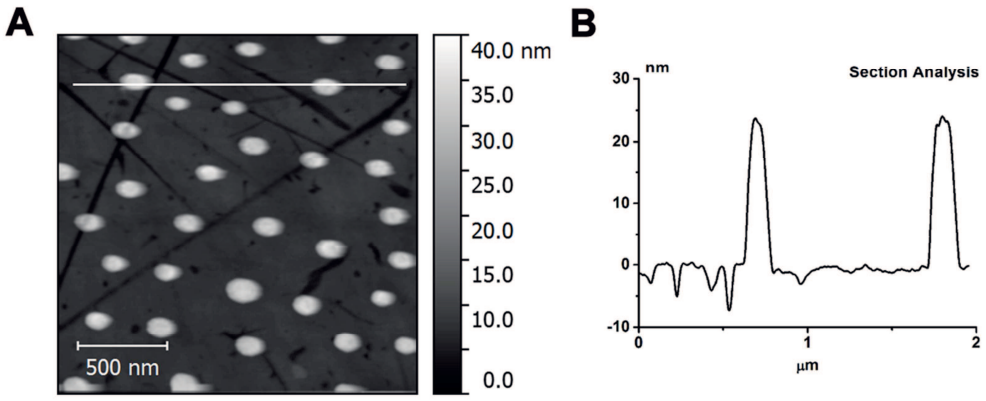

Figure 21. Atomic force microscopy image of LSPR sensor decorated with gold nanodisks acquired in tapping mode (A) and section analysis (B).

Immediately before experiment, both type of sensors are treated with UV Ozone Procleaner (BioForce Nanoscience, Ames, USA) for 15 min, then rinsed with Millipore water and dried under a nitrogen flow.
For the Au and SiO_2 sensor chips, the LSPR plasmon peak, recorded in PBS buffer solution, are found respectively at around 670 and 710 nm (data not shown). The baseline LSPR response is recorded in PBS buffer solution. After stabilization of the signal, the PBS buffer solution is replaced by the one containing thiolated ssDNA oligonucleotide. During the experiment, the liquid sample is introduced by peristaltic pump at a constant flow rate of 50 µL/min. After 7 min the pump is shouted down and the signal is recorded until baseline stabilization is obtained (20 minutes). Then, the PBS solution is again injected into the measurement cell. Finally, the hybridization process is allowed by exchanging the buffer solution with the one containing the ssDNA target strands.

3.3 Results and discussion

In order to evaluate the sensitivity and specificity of the Au nanodisk arrays as a biosensing platform, hybridization experiments of perfect (PM) and mismatched (MM) oligonucleotides target to the single stranded DNA probe immobilized onto the surface have been performed.
Therefore, at first thiolated single strands of DNA 35 nt (probe) have been immobilized onto the nanoplasmonic LSPR sensor, whose length has been chosen to reduce the unwanted nonspecific interactions [49, 50].
The stability of the immobilized probes has been tested by means of an accurate rinsing process with buffer. Finally, the respective yield and rate of the hybridization process for PM and MM targets have been monitored in situ. All data presented in the following paragraphs are the mean of three independent experiments +/− standard deviation (SD) (unless mentioned otherwise).

3.3.1 Probes immobilization onto LSPR sensor

Typical extinction spectra of ssDNA oligonucleotide-modified Au nanodisk arrays is shown in
Figure 22 A. The specific binding of ssDNA oligonucleotides caused a red shift in the LSPR resonance, due to the variation of the refractive index from that of PBS buffer (n_{PBS}=1.33) to that of the DNA layer (n_{DNA}=1.46) bound to the Au nanostructures [51].
The LSPR signal change, monitored in real-time after the ssDNA probe injection (see Figure 22B), can be used to figure out the probe immobilization kinetic. The ssDNA probe molecules are stably bound on the Au LSPR sensor surface as indicated by the negligible Δλ change measured after the rinsing step. The anchoring stability can be explained in terms of the synergic effect of the covalently bound terminal thiol and the sequence of 10 adenines adjacent to the linking group, which, according to literature, contribute to the enhancement of the strength of interaction between the ssDNA probe and Au LSPR surface [52].
In order to rule out the possible effect of aspecific interactions, the adsorption of ssDNA probe has been monitored also on SiO_2 coated sensor. In this case, no shift is detected within the experimental error, indicating that the immobilization process is basically driven by the specific formation of covalent bonds between the ssDNA probe molecules with the Au nanodisks (see Figure 22 B).

Assuming that at the steady state, ssDNA molecules forms an uniform adlayer on surface, the plasmon peak shift (1.1 $\pm$ 0.2 nm) can be converted in optical thickness [53] according to the following equation:

$$\Delta\lambda = S\left[1 - e^{-\frac{t}{L}}\right]\left(n_{DNA} - n_{buffer}\right) \qquad Eq.\ 48$$

Where S = 72 nm/RIU is the bulk refractive sensitivity of the LSPR sensor, L = 27.2 nm the decay length of the LSPR evanescent wave according to sensor specification, t is the adsorbed protein layer thickness, n_{DNA}=1.46 and n_{buffer}=1.33 are respectively the bulk refractive index for the a uniform ssDNA layer and the buffer solution [51].

The calculated thickness has been further converted in adsorbed mass (M) according to the De Feijter's equation [54],

$$M = t\frac{\left(n_{DNA} - n_{buffer}\right)}{\left(\frac{dn}{dc}\right)} \qquad Eq.\ 49$$

Where dn/dc is the refractive index increment for a concentration change assumed to be nearly constant for protein solutions, at a value of 0.175 cm^3/g [55].

In turn, from the adsorbed mass value the ssDNA surface density, normalized for the gold nanodisks' active area, has been estimated to be of 2.8 $\pm$ 0.1 x 10^{12} molecules/cm^2, which corresponds to ~ 3.5 x 10^3 molecules for each Au nanodisk.

In our condition the average [effective area]/[probe molecule] is ~35 nm^2, i.e., about seven times higher than the value calculated (~5 nm^2) for ssDNA strands of the same length under high ionic force condition [56]. This rules out the possibility that steric hindrance between DNA strands becomes a significant barrier to hybridization [57]. Furthermore, the value of association rate constant, estimated using a simple Langmuir kinetics equation [57], is 1.64 $\pm$ 0.02 x 10^4 M^{-1} s^{-1}, is higher than the one reported in literature for the immobilization of the same length ssDNA strands onto flat Au surfaces [58] (5 x 10^3 M^{-1} s^{-1}). This, in fact, suggests that the nanostructures significantly enhance the rate of DNA immobilization process.

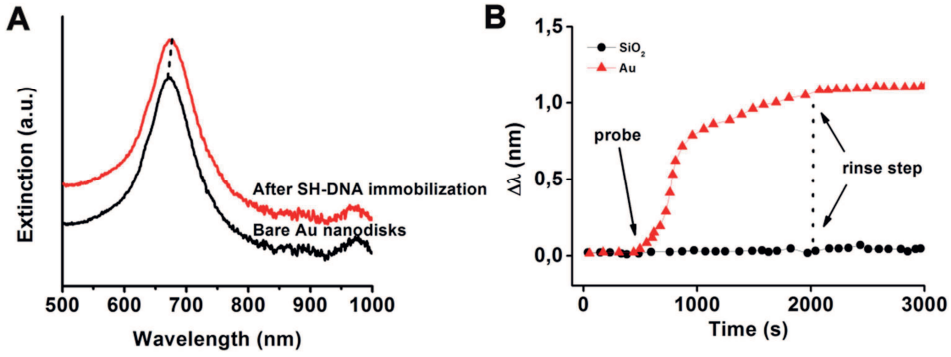

Figure 22. (A) Representative extinction spectra of the bare Au nanodisk arrays and after immobilization with thiolated ssDNA probe. (B) Plasmon peak shift curves (Δλ) following the binding of thiolated ssDNA probes, respectively on Au nanodisks and SiO_2-coated LSPR sensors.

3.3.2 Evaluation of sensor performance

Figure 23 reports the calibration curves generated reporting the plasmon peak (Figure 23 A) and peak shift (Figure 23 B) (measured at saturation) with respect to the concentration of PM and MM targets in solution. The signal increases with the target concentration reproducing a Langmuir isotherm behavior for both types of target over a concentration range from 10 nM to 170 nM.
Taking into account the three data points at low concentrations (see inset in in Figure 23 B), we obtained a regression line showing R^2 values of 0.964 and 0.941 for PM and MM target respectively. The detection limit (LOD) of the LSPR DNA sensor was calculated as three times of the standard deviation of the ordinate intercept divided by the slope of the regression line [59,60]. As a result, we found that the LOD for PM is about of 10 nmol/L, while for MM is 13 nmol/L (corresponding respectively to 40 and 52 fmol of target). This sensitivity is in the same range of the ones obtained by using fluorescence methods and PCR-based sequence recognition [14, 16].

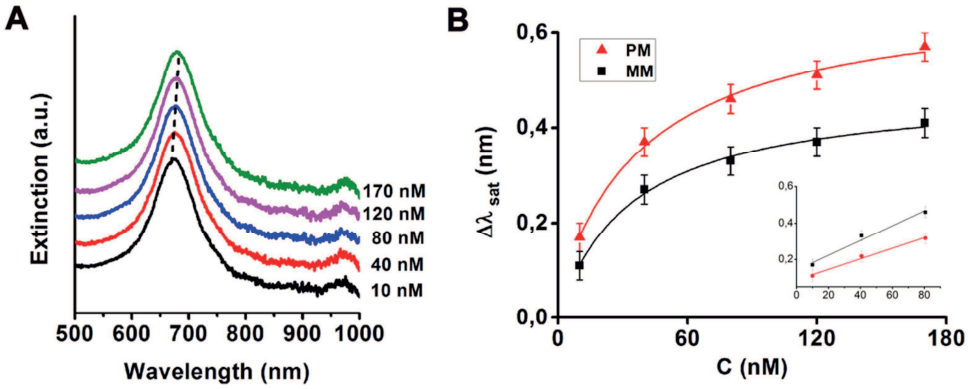

Figure 23 (A) Representative extinction spectra of the functionalized Au nanodisks after hybridizing with various concentrations of perfect match complementary DNA (PM) and single base mismatch DNA (MM). (B) Calibration curves plotting the maximum peak shift at saturation versus DNA concentrations over the full range of concentrations (main plot) and for the lower concentration point (inset), together with the fitted curves.

3.3.3 Kinetic of probe-target hybridization from single component solution

The comparison of the kinetics of the probe- perfect matching sequence (PM) and probe-single base mutated sequence (MM), where adenine (A) is replaced by cytosine (C) in the MM sequence, may be used to determine the dependence of the hybridization process on the base mispairing.
The kinetic curves, obtained exposing the ssDNA layer to a series of MM and PM solutions with concentration ranging from 10 nM to 170 nM are shown in Figure 24 A and 24 B. The shift of the plasmon peak gradually increases with time both for the probe-PM and probe-MM hybridization. The

signal reaches the steady state at shorter time for higher concentrations. In particular, for the highest concentration (170 nM) is stabilized after about 16 and 27 min respectively for PM and MM. According to the literature [61, 62], in order to evaluate the hybridization rate constant, k_a, the hybridization process was treated as an adsorption process. Since we performed the hybridization experiment under an excess of target strands compared to number of probe molecules tethered on surface, we can assume that the whole process can be treated as a pseudo-first order one [63, 64], according to the following rate equation [23]:

$$\frac{d(\Delta\lambda)}{dt} \propto \frac{dB}{dt} = k_a C(R_t - B) \qquad Eq.\,50$$

Where $\Delta\lambda$ represents the plasmon shift, and it is assumed to be directly proportional to the surface concentration of bound targets, B. *C* is the concentration of target in solution and R_t is the initial surface concentration of probes.

In our experimental condition, dissociation rate constants are negligible (no target dissociation is observed during post-hybridization buffer rinse experiments) and therefore only one variable (k_a) is considered in the fitting analysis for surface kinetic data. Moreover, if the negligibly small dissociation rate constant was considered as a second fitting parameter, then the resulting k_a value obtained from fitting analysis does not change, although it would have a larger error.

The solution of the previous equation is the following:

$$B = R_t\left[1 - e^{-(k_{obs}t)}\right] \qquad Eq.\,51$$

Where k_{obs} is the apparent rate constant, depending on the target concentration in solution according to the relationship reported below:

$$k_{obs} = Ck_a \qquad Eq.\,52$$

According to above assumptions, the peak shift as a function of time, $\Delta\lambda_t$, is proportional to the adsorbed mass at surface, i.e., to the surface concentration of bound targets, B. Accordingly, a single exponential function can be used to fit the experimental data,

$$\Delta\lambda_t \propto \left[1 - e^{-(k_{obs}t)}\right] \qquad Eq.\,53$$

Figure 24 C reports the Plot of the measured k_{obs} versus the target concentration in solution, *C*, for PM and MM sequences. As one can see, a linear relationship is obtained, as expected from literature [21], which can be used to determine the intrinsic rate constant k_a by a simple linear regression.
In particular, the value of k_a is found to be higher for PM sequences, 1.46 $\pm$ 0.06 x 10^4 M^{-1} s^{-1}, than the k_a value for MM sequences, 4.5 $\pm$ 0.2 x 10^3 M^{-1} s^{-1}. This confirms that the hybridization of fully complementary strand (PM) is a significantly faster process compared to the one of mismatched sequences (Figure 24 A e B).

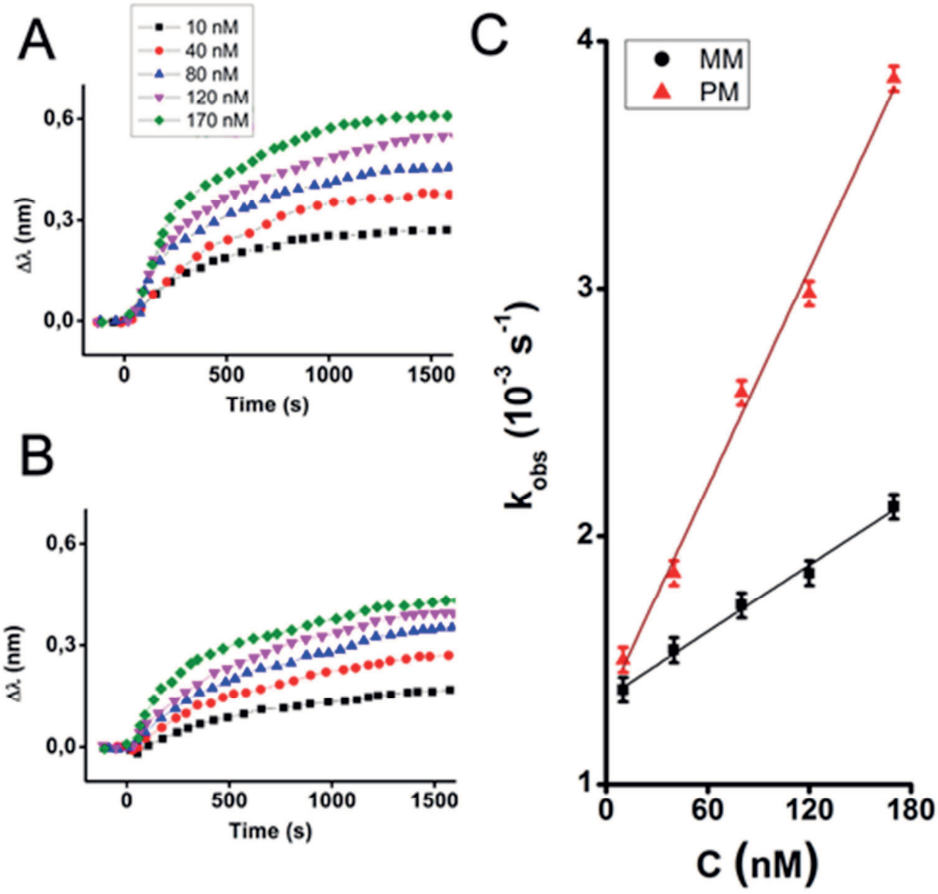

Figure 24. Kinetic analysis of PM and MM targets interacting with surface bound probe molecules. A,B: Association of PM (A) and MM (B) ssDNA with surface bound probe strands monitored as change with time in the LSPR peak wavelength ($\Delta\lambda$) for different target concentration (10, 40, 80, 120, 170 nM). C: Apparent rate constants k_{obs} from kinetic curve of $\Delta\lambda$ (t) for PM (triangle symbols) and MM (square symbols) target versus concentration (10 nM to 170 nM); solid lines are linear fits, $k_{obs} = C \cdot k_a$. Each point is the linear regression slope (± standard deviation, SD) of three independent experiments, R^2>90%;

3.3.4 Competitive PM vs. MM hybridization (binary solutions)

An important consideration for clinical translation is the ability to detect a point mutation (i.e., the single base defect) in a mixed sample [65], containing both mutant and perfect match DNA. In order to determine the capability of the present method to detect the mutation point, we investigated

various binary solutions with different mutant/perfect match molar ratio, maintaining constant the total concentration at 40 nM.

The kinetic of hybridization for a 40:60, 50:50, 60:40, 70:30 and 80:20 PM/MM target solutions are shown in Figure 25 A. After injecting the solution, the plasmon peak shift was measured at the same time for all the binary solutions, corresponding to the average time (20 min) until the equilibrium is reached between the bulk concentration and the corresponding hybridization steady state for the 40 nM reference PM concentration, taken as reference. After the reference time the experiment was stopped.

As shown in Figure 25 A, the hybridization from the two-component systems resulted in lower yield, with a lower peak shift compared to the one measured for the reference 40 nM solution of pure PM hybridization. In particular, the rate of hybridization is found to decrease with the increasing fraction of MM in the binary solution . This suggests that presence of MM target kinetically interferes with the PM hybridization process, behaving as competitor.

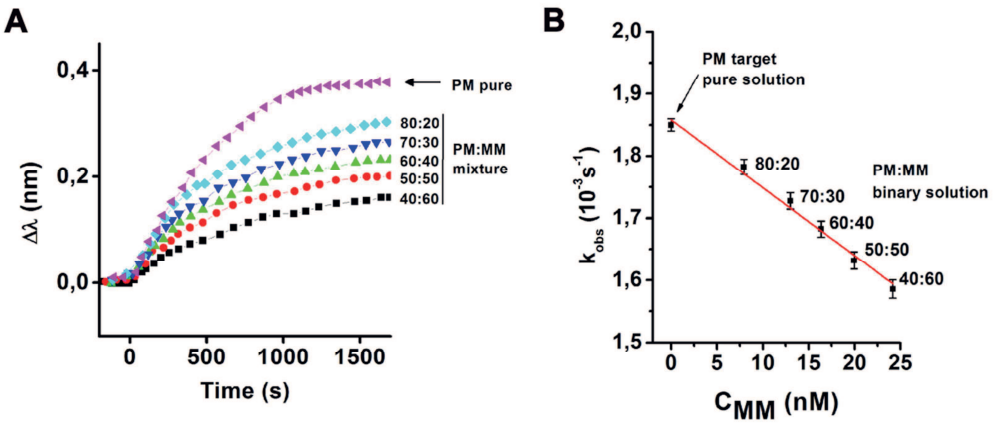

Figure 25. Kinetic analysis of two-component systems (PM and MM) interacting with surface bound probe molecules as a function of time for different molar ratio (80:20, 70:30, 60:40, 50:50 and 40:60 PM/MM ratio). Peak shift (Δλ) measured at saturation for different molar ratio compared to the PM at 40 nM. (B) Rate constants k_{obs} from kinetic curve of Δλ (t) for PM pure solution and PM: MM binary solution versus MM target concentration; red solid lines is linear fits. Each point is the linear regression slope (± standard deviation, SD) of three independent experiments, R^2>90%;

In order to clarify this effect, we have applied the rate equation developed by Bishop [23] to describe the hybridization rate for mixtures of perfect match/mismatch targets. The binary solution with PM and a MM target, can be described by a system of equations similar to those used for pure target solution (see Eq. 50). The equations have to reflect the consumption of available probe sites due to both the match and mismatch:

$$\frac{dB^m}{dt} = k_a^m C^m (R_t - B^m - B^{mis}) \qquad Eq.\,54$$

$$\frac{dB^{mis}}{dt} = k_a^{mis} C^{mis} \left(R_t - B^m - B^{mis}\right) \qquad Eq.\,55$$

where C^m corresponds to the concentration of perfectly matched target, C^{mis} corresponds to the concentration of the mismatch target, B^m is the bound concentration by the match and B^{mis} is the bound concentration by the mismatch, with the corresponding hybridization rate constants.

Since LSPR measures the rate of the overall hybridization process, we have to consider the sum of the Eq.54 and Eq.55 obtaining the following equation:

$$\frac{dB^{tot}}{dt} = \left(k_a^m C^m + k_a^{mis} C^{mis}\right)\left(R_t - B^{tot}\right) \qquad Eq.\,56$$

where B^{tot} is the sum of the concentration of B^m and B^{mis}.

Due to the fact that, in our experimental conditions, the total concentration of the binary mixture is constant (C_0), the Eq.56 can be rearranged as it contains only the concentration term of the mismatch target:

$$\frac{dB^{tot}}{dt} = \left[k_a^m C_0 - \left(k_a^m - k_a^{mis}\right)C^{mis}\right]\left(R_t - B^{tot}\right) \qquad Eq.\,57$$

Where the term $\left[k_a^m C_0 - \left(k_a^m - k_a^{mis}\right)C^{mis}\right]$ represents the apparent rate constant (k_{obs}) for the hybridization from binary solution.

In Figure 25 B the k_{obs} values obtained by the Langmuir fitting of LSPR curves reported in Figure 25 A, are plotted as a function of the mismatch target concentration in the mixture. As reference value we also reported the k_{obs} for pure perfect matched target at 40 nM. A linear equation can fit the experimental points for two component solutions indicating that the apparent rate constant decrease linearly with the increasing mismatch target concentration. Moreover, the value of the slope is found in fair agreement with the above reported difference of hybridization rate constants for perfect match and mismatch target. Accordingly, in presence of the competing MM sequences, for a given time, a higher amount of substrate molecules is required to reach half of the $\Delta\lambda$ maximum signal, with respect to the case of the uninhibited case (Figure 25 A).

On the other hand, from the solid red line in Figure 25 B, representing the apparent rate constant for the mixture, we may figure out an indication on the presence or not of mutation and we can also estimate the relative molar ratios. This finding is obviously valid under the assumptions that the two targets in the mixture adsorb each with its own value of k_a, that is, $k_a^m > k_a^{mis}$ (see Figure 24 C) and that the measurement of peak shift for the two-component systems reflects the two-components composition of the solution.

3.4 Conclusions

In summary, we have investigated the effects of single base mutation on the competitive hybridization rate between surface-bound DNA probes and DNA target strands in solution.

LSPR sensors, that when compared to other optical techniques, allows the detection of biomolecular interactions in localized sensing volume skipping the interfering effect of the bulk of solution, were used to demonstrated at first the efficient probe immobilization on gold nanodisks in a nondestructive manner and also to detect both perfect matching (PM) and mismatching (MM) targets hybridization, with a limit of detention in the range of 10 nmole/L.

Furthermore, this allowed to measure the "effective" hybridization kinetics and affinity for the various systems. Indeed, it has been found a probe-PM target hybridization faster and stronger than the one of probe-MM target interaction. In turn, the single component isotherms determined for the two DNA strands enabled the unraveling of the more complex process occurring for binary solution.

Under the assumption that both PM and MM may hybridize with the surface-anchored probes in the binary solutions, it has been shown that the MM sequences play a clear inhibition role on the hybridization rate of PM strand.

In summary, the present approach, while keeping comparable sensitivity with techniques as fluorescence or PCR-based methods, allows the single step and label-free discrimination of subtle hybridization steps, providing a valuable improvement with respect to the recent literature, either employing in silico simulations [23], or multistep processes implying manipulation of the samples to be analyzed [21].

Further studies are in progress in our laboratory to exclude the possible presence of single mutation sequences (MM) on the sensing surfaces. We feel that the results here presented may provide significant improvement in view of their application to the DNA array-based technologies.

3.5 References

1. International human genome sequencing consortium. Finishing the euchromatic sequence of the human genome. Nature 431 (2004) 931-945.
2. M. Lynch. The Origins of Genome Architecture. Sunderland, MA: Sinauer Associates, 2007, pp 43-44.

3. T. A. Kunkel, K. Bebenek. DNA Replication Fidelity. Annual Review of Biochemistry 69 (2000) 497-529.
4. R.W. Taylor, D. M. Turnbull. Mitochondrial DNA mutations in human disease. Nature Reviews Genetics 6 (2005) 389-402.
5. M. Cargill, D. Altshuler, J. Ireland, P. Sklar, K. Ardlie, N. Patil, C. R. Lane, E. P. Lim, N. Kalyanaraman, J. Nemesh, L. Ziaugra, L. Friedland, A. Rolfe, J. Warrington, R. Lipshutz, G. Q. Daley, E. S. Lander. Characterization of single-nucleotide polymorphisms in coding regions of human genes. Nature Genetics 22 (1999) 231 – 238.
6. R. Karki, D. Pandya, R. C. Elston, C. Ferlini. Defining “mutation” and “polymorphism” in the era of personal genomics. BMC Medical Genomics (2015) 8:37.
7. T. Van den Broeck, S. Joniau, L. Clinckemalie, C. Helsen, S. Prekovic, L. Spans, L. Tosco, H. Van Poppel, F. Claessens. The Role of Single Nucleotide Polymorphisms in Predicting Prostate Cancer Risk and Therapeutic Decision Making. BioMed Research International 2014 (2014) Article ID 627510.
8. X. Mao, B. D Young, Y. Lu. The Application of Single Nucleotide Polymorphism Microarrays in Cancer Research. Curr Genomics 8 (2007) 219–228.
9. J. Robert, V. L. Morvan, D. Smith, P. Pourquier, J. Bonnet. Predicting drug response and toxicity based on gene polymorphisms. Crit Rev Oncol Hematol. 54 (2005) 171-196.
10. T. Satoh. Genetic polymorphism in drug metabolism and toxicity: Linking animal research and risk assessment in man. AATEX 14 (2007) 443-445.
11. D. M. Townsend, K. D. Tew. The role of glutathione-S-transferase in anti-cancer drug resistance. Oncogene 22 (2003) 7369–7375.
12. O. Kranenburg, The KRAS oncogene: Past, present, and future. Biochimica et Biophysica Acta 1756 (2005) 81-82.
13. D. Shao, Y. Lin, J. Liu, L. Wan, Z. Liu, S. Cheng, L. Fei, R. Deng, J. Wang, X. Chen, L. Liu, X. Gu, W. Linag, P. He, J. Wang, M. Ye, J. He, A targeted next-generation sequencing method for identifying clinically relevant mutation profiles in lung adenocarcinoma. Scientific Reports 6 (2016) 22338-22347.
14. S. I. Stoeva, J.-S Lee, C.S Thaxton, C. A. Mirkin, Multiplexed DNA Detection with Biobarcoded Nanoparticle Probes. Angew. Chem. Int. Ed. 45 (2006) 3303 –3306.
15. M. A. Vlachou, K.M. Glynou, P.C. Ioannou, T.K. Christopoulos, G. Vartholomatos, Development of a three-biosensor panel for the visual detection of thrombophilia-associated mutations. Biosensors and Bioelectronics 26 (2010) 228–234.
16. E.-O. Ganbold, T. Kang, K. Lee, S.Y. Lee, S.-W. Joo, Aggregation effects of gold nanoparticles for single-base mismatch detection in influenza A (H1N1) DNA sequences using fluorescence and Raman measurements. Colloids and Surfaces B: Biointerfaces 93 (2012) 148–153.
17. Y. You, B. G. Moreira, M. A. Behlke and R. Owczarzy, Design of LNA probes that improve mismatch discrimination. Nucleic Acids Res., 34 (2006) e60-e71.

18. K.K. Jensen, H. Orum, P.E. Nielsen, B. Norden, Kinetics for hybridization of peptide nucleic acids (PNA) with DNA and RNA studied with the BIAcore technique. Biochemistry, 36 (1997) 5072–5077.
19. H. Urakawa, S. El Fantroussi, H. Smidt, J. C. Smoot, E. H. Tribou, J. J. Kelly, P. A. Noble, D. A. Stahl, Optimization of single-base-pair mismatch discrimination in oligonucleotide microarrays. Appl. Environ. Microbiol., 69 (2003) 2848–2856.
20. L.D.S. Lapitan Jr., Y. Guo, D. Zhou, Nano-enabled bioanalytical approaches to ultrasensitive detection of low abundance single nucleotide polymorphisms. Analyst 12 (2015) 3872–3887.
21. K. Tawa K, D.F. Yao, W. Knoll Matching base-pair number dependence of the kinetics of DNA-DNA hybridization studied by surface plasmon fluorescence spectroscopy. Biosensors and Bioelectronics, 21 (2005) 322–329.
22. D. A. Edwards, S.A. Jackson, Testing the validity of the effective rate constant approximation for surface reaction with transport. Applied Mathematics Letters 15 (2002) 547-552.
23. J. Bishop, S. Blair, A.M. Chagovetz, A Competitive Kinetic Model of Nucleic Acid Surface Hybridization in the Presence of Point Mutants. Biophysical Journal 90 (2006) 831–840.
24. M. L. Ermini, S. Mariani, S. Scarano, M. Minunni. Bioanalytical approaches for the detection of single nucleotide polymorphisms by Surface Plasmon Resonance biosensors. Biosensors and Bioelectronics 61 (2014) 28–37.
25. H. Šípová, J. Homola. Surface plasmon resonance sensing of nucleic acids: A review. Anal. Chim. Acta 773 (2013) 9–23.
26. R. D'Agata, G. Spoto. Artificial DNA and surface plasmon resonance. Artif. DNA PNA XNA 3 (2012) 45–52.
27. G. A. Lopez, M. C. Estevez, M. Solera, L. M. Lechuga. Recent advances in nanoplasmonic biosensors: applications and lab-on-a-chip integration. Nanophotonics, DOI: 10.1515/nanoph-2016-0101.
28. K. A. Willets, R. P. Van Duyne. Localized surface plasmon resonance spectroscopy and sensing. Annu Rev Phys Chem. 58 (2007) 267-297.
29. J. Voros, J. J. Ramsden, G. Csùcs, I. Szendrő, S.M. De Paula, M. Textor, N.D. Spencer. Optical grating coupler biosensors. Biomaterials 23 (2002) 3699–3710.
30. A. B. Dahlin, N. J. Wittenberg, F. Höök, Sang-Hyun Oh. Promises and challenges of nanoplasmonic devices for refractometric biosensing. Nanophotonics 2 (2013) 83–101.
31. S. L. Dodson, C. Caob, H. Zaribafzadeha, S. Lic, Q. Xionga, Engineering plasmonic nanorod arrays for colon cancer marker detection. Biosensor and bioelectronics 63 (2015) 472-477.
32. T. J. Schmitt, J. B. Rogers, T. A. Knotts IV. Exploring the mechanisms of DNA hybridization on a surface. J. Chem. Phys. 138 (2013) 035102.
33. Y. Gao, L. K. Wolf, M. Georgiadis. Secondary structure effects on DNA hybridization kinetics: a solution versus surface comparison. Nucleic Acids Research 34 (2006) 3370-3377.
34. H. Söderlund. DNA hybridization: comparison of liquid and solid phase formats. Ann Biol Clin 48 (1990) 489-491.

35. S. Song, H. Xu, C. Fan. Potential diagnostic applications of biosensors: current and future directions. Int J Nanomedicine. 1 (2006) 433–440.
36. J. H. Monserud, D. K. Schwartz. Mechanisms of Surface-Mediated DNA Hybridization. ACS Nano 8 (2014) 4488–4499.
37. V. Chan, D. J. Graves, S. E. McKenzie. The biophysics of DNA hybridization with immobilized oligonucleotide probes. Biophys J. 69 (1995) 2243-55.
38. P. Gong, R. Levicky. DNA surface hybridization regimes. PNAS 105 (2008) 5301–5306.
39. H. Dai, M. Meyer, S. Stepaniants, M. Ziman, R. Stoughton. Use of hybridization kinetics for differentiating specific from non-specific binding to oligonucleotide microarrays. Nucleic Acids Research. 30 (2002) e86.1 – e86.8.
40. T. E. Ouldridge, P. Šulc, F. Romano, J. P. K. Doye, A. A. Louis. DNA hybridization kinetics: zippering, internal displacement and sequence dependence. Nucleic Acids Res. 41 (2013) 8886–8895.
41. A. Halperin, A. Buhot, E. B. Zhulina. On the hybridization isotherms of DNA microarrays: the Langmuir model and its extensions. J. Phys.: Condens. Matter 18 (2006) S463–S490.
42. J. Bishop, S. Blair, A. M. Chagovetz. A Competitive Kinetic Model of Nucleic Acid Surface Hybridization in the Presence of Point Mutants. Biophysical Journal 90 (2006) 831–840.
43. J. SantaLucia Jr, D. Hicks, The Thermodynamics of DNA Structural Motifs. Annu. Rev. Biophys. Biomol. Struct. 33 (2004) 415-440.
44. E.M. Larsson, M.E.M Edvardsson, C. Langhammer, I. Zoric, B Kasemo, A combined nanoplasmonic and electrodeless quartz crystal microbalance setup. Review Of Scientific Instruments 80 (2009) 125105-125110.
45. K. Johansen, R. Stalberg, I. Lundstrom, B. Liedberg, Surface plasmon resonance: Instrumental resolution using photo diode arrays. Meas. Sci. Technol. 11 (2000) 1630–1638.
46. H. Fredriksson, Y. Alaverdyan, A. Dmitriev, C. Langhammer, D.S. Sutherland, M. Zäch, B. Kasemo, Hole–Mask Colloidal Lithography. Adv. Mater. 19 (2007) 4297–4302.
47. C. Huang, J. Ye, S. Wang, T. Stakenborg, L. Lagae, Gold nanoring as a sensitive plasmonic biosensor for on-chip DNA detection. Appl. Phys. Lett. 100 (2012) 173114-1731118.
48. B. Grunwald, G. Holst, Fibre optic refractive index microsensor based on white-light SPR excitation. Sens. Actuators A 113 (2004) 174–180.
49. K. Knez, D. Spasic, K.P.F. Janssen, J. Lammertyn, Emerging technologies for hybridization based single nucleotide polymorphism detection. Analyst, 139 (2014) 353-370.
50. S. Ikuta, K. Takagi, R.B. Wallace, K. Itakura, Dissociation kinetics of 19 base paired oligonucleotide-DNA duplexes containing different single mismatched base pairs. Nucleic Acids Res. 15 (1987) 797–811.
51. E. Özkumur, S. Ahn, A. Yalçın, C. A. Lopez, E. Çevik, R. J. Irani, C. DeLisi, M. Chiari, M. Selim Ünlü. Label-free microarray imaging for direct detection of DNA hybridization and single-nucleotide mismatches. Biosensors and Bioelectronics 25 (2010) 1789-1795.

52. M. Yang, H.C.M. Yau, H.L. Chan, Adsorption Kinetics and Ligand-Binding Properties of Thiol-Modified Double-Stranded DNA on a Gold Surface. Langmuir 14 (1998) 6121-6129.
53. Jonsson, M. P; Jönsson, P; Höök, F. Simultaneous Nanoplasmonic and Quartz Crystal Microbalance Sensing: Analysis of Biomolecular Conformational Changes and Quantification of the Bound Molecular Mass. Anal. Chem. 80 (2008) 7988–7995.
54. J.A. de Feijter, J. Benjamins, F. A. Veer. Ellipsometry as a tool to study the adsorption of synthetic and biopolymers at the air-water interface. Biopolymers. 17 (1978) 1759–1772.
55. S. Vogt, Q. Su, C. Gutiérrez-Sánchez, G. Nöll. Critical View on Electrochemical Impedance Spectroscopy Using the Ferri/Ferrocyanide Redox Couple at Gold Electrodes. Anal. Chem. 88 (2016) 4383–4390.
56. A. B. Steel, R.L. Levicky, T.M. Herne, M.J. Tarlov,. Immobilization of nucleic acids at solid surfaces: effect of oligonucleotide length on layer assembly. Biophys. J. 79 (2000) 975–981.
57. A. Halperin, A. Buhot, E.B. Zhulina, Sensitivity, Specificity, and the Hybridization Isotherms of DNA Chips. Biophys. J. 86 (2004) 718–730.
58. R. Marie, H. Jensenius, J. Thaysen, C. B. Christensen, A. Boisen. Adsorption kinetics and mechanical properties of thiol-modified DNA-oligos on gold investigated by microcantilever sensors. Ultramicroscopy 91 (2002) 29-36.
59. X. Liu, W. Tan. A Fiber-Optic Evanescent Wave DNA Biosensor Based on Novel Molecular Beacons. Anal. Chem. 71 (1999) 5054–5059.
60. P.A. E. Piunno, U. J. Krull. Fiberloptic DNA Sensor for Fluorometric Nucleic Acid Determination. Anal. Chem. 67 (1995) 2635-264.
61. T. Liebermann, W. Knoll, Surface-plasmon field-enhanced fluorescence spectroscopy, Colloid Surf. A, 171 (2000) 115-130.
62. T. Liebermann, W. Knoll, P. Sluka, R. Herrmann, Complement hybridization from solution to surface-attached probe- oligonucleotides observed by surface-plasmon-field-enhanced fluorescence spectroscopy. Colloid Surf. A 169 (2000) 337–350.
63. S.M. Schreiner, D.F. Shudy, A.L. Hatch, A. Opdahl, L.J. Whitman, D.Y. Petrovykh, Controlled and efficient hybridization achieved with DNA probes immobilized solely through preferential DNA-substrate interactions. Anal. Chem. 82 (2010) 2803–2810.
64. A. Halperin, A. Buhot, E.B. Zhulina, On the hybridization isotherms of DNA microarrays: the Langmuir model and its extensions. J. Phys.: Condens. Matter 18 (2006) S463-S490.
65. T. Naiser, O. Ehler, J. Kayser, T. Mai, W. Michel, A. Ott, Impact of point-mutations on the hybridization affinity of surface-bound DNA/DNA and RNA/DNA oligonucleotide-duplexes: Comparison of single base mismatches and base bulges. BMC Biotechnology 8 (2008) 48-70

CHAPTER 4.

INFLUENCE OF PH ON THE KINETICS OF VESICLES ADSORPTION

4.1 Introduction

4.1.1 Supported phospholipid bilayers as models for cell membrane

Cell membranes are primarily composed of a variety of lipids in the form of two asymmetric leaflets and functional proteins [1]. The membranes define a cellular boundary and provide a basic platform for tight regulation of many biological processes, including material transport, signal transduction, trafficking, pathogenic pathways, intercellular organization and response to the extracellular matrix [2].

The complexity of biological membranes has motivated the development of a wide variety of simpler model systems whose size, geometry, and composition can be tailored with great precision [3]. In this respect, phospholipid vesicle are versatile supramolecular assemblies which has been demonstrated to be useful as model systems for cell membranes [4]. Their physical properties are similar to those of native cell membranes in which the cellular interior is isolated from the external environment by lipid and protein-rich dynamic boundaries. The capacities of lipid vesicles for tuning chemical composition and embedding and encapsulating various materials have facilitated the use of the vesicles in many fields, including cell membrane-mimicking materials [5] and drug delivery [6]. Subsequently, supported lipid bilayers (SLBs) or self-assembled lipid membranes on solid substrates are model membrane platforms that provides robust artificial cell membranes in a synthetically controllable manner, recapitulates key membrane functions and allows the study of structural changes and reactions in membranes on a surface [7].

For these reasons, phospholipid bilayers have received increasing practical and scientific interest due to the wide range of biotechnological and medical applications including (1) biochips for medical diagnostics [7] and drug screening [8], (2) high electrical resistance films for biosensor design [9], (3) biomimetic photosynthesis platforms [10], and (4) biocompatible, nonfouling surfaces [11]. In order to realize such applications, which may depend critically on the model membrane's architecture, an improved understanding of the processes by which they form and the forces that guide the self-assembly of these platforms is mandatory [12].

4.1.2 Mechanisms of SLB formation

There are three general methods for the formation of supported phospholipid bilayers on planar supports for sensor applications. The first method involves the transfer of a lower leaflet of lipids from the air–water interface by the Langmuir–Blodgett technique [13] (see Figure 26 A). This is followed by the transfer of an upper leaflet by the Langmuir–Schaefer procedure, which involves horizontally dipping the substrate to create the second layer [14] (see Figure 26 B).

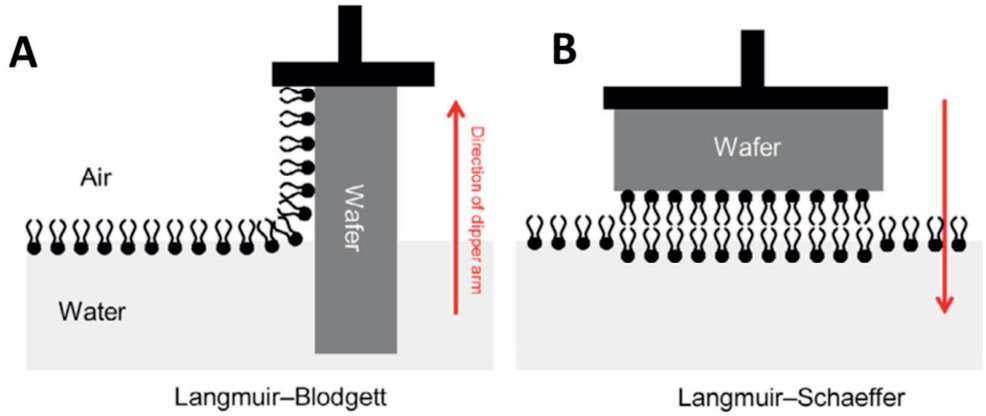

Figure 26. Schematic illustration of different modes of Langmuir film deposition: (A) Langmuir–Blodgett vertical method, (B) Langmuir–Shaefer [15].

A second method of supported bilayer formation is the adsorption and fusion of vesicles from an aqueous suspension to the substrate surface [16] (see Figure 27).

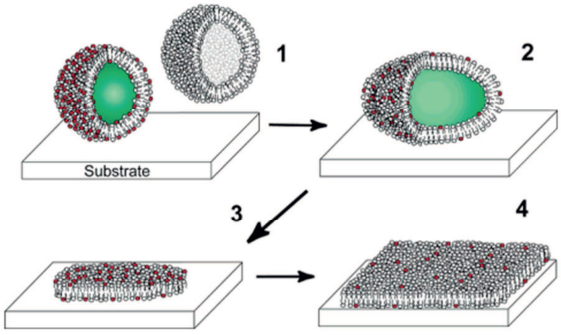

Figure 27. Four step scenario of supported bilayer formation via vesicle fusion comprising (1) vesicle adsorption, (2) fusion of vesicles at the surface to form larger vesicles, (3) rupture of the fused vesicles resulting in bilayer patches, and finally (4) merging of the patches [16].

Also, a combination of the two methods can be employed by first transferring a monolayer via the Langmuir–Blodgett technique followed by vesicle fusion to form the upper layer (see Figure 28) [17].

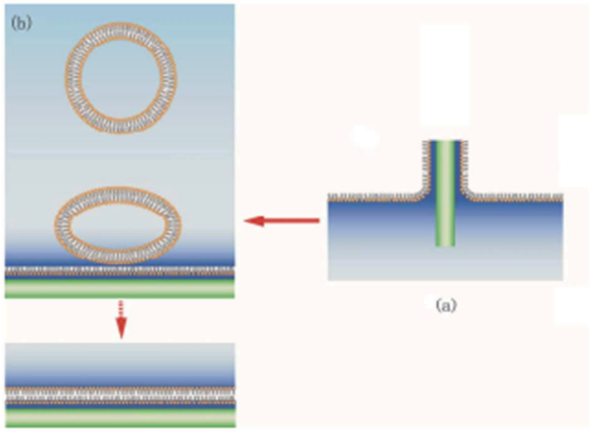

Figure 28. Schematic description of a combination of the Langmuir–Blodgett and vesicle fusion processes for the formation of supported lipid bilayers [17].

Each of the three deposition methods has its particular advantages and disadvantages.
The transfer of amphiphilic molecules from the air–water interface to a solid substrate is useful for the formation of asymmetric bilayers [18]; however, it is difficult if not impossible to incorporate transmembrane proteins into the lipid bilayer with this technique because prior to transfer portions of the proteins within the monolayer are exposed to air and can become irreversibly denatured [19].
The adsorption and fusion of small unilaminar vesicles (SUVs) is one of the easiest and most versatile means for forming solid supported phospholipid bilayers. SUVs can be prepared by a plethora of methods. The simplest involves the extrusion of multilaminar vesicles through porous polycarbonate membranes at high pressure [20, 21]. Another method is the sonication and ultracentrifugation of aqueous lipid suspensions [22].
The process of SLB formation begin with the adsorption of intact vesicles from the bulk solution onto the substrate [16]. As the vesicle surface coverage reach a critical value (henceforward denoted as critical vesicular coverage) the confinement of neighboring vesicles causes an induced stress on the vesicle responsible for its rupture [23]. The critical vesicular coverage and so the kinetic of vesicle rupture depends to several experimental factors including the vesicle composition, size, surface charge, surface roughness, surface cleanliness, solution pH, ionic strength, and the osmotic pressure of the vesicles [24, 25]. The main findings related to these subjects that will be briefly reviewed in the next paragraph.
Once a vesicle has ruptured, the resulting bilayer patch exposes an edge. These edges are energetically unfavorable and, at least from a thermodynamic perspective, it was demonstrated that they promote the interaction with adjacent lipid material, such as the rupture of surface-bound

vesicles or vesicles from solution [12]. Provided the density of adsorbed vesicles is sufficiently high, such a process can propagate in a cascade of rupture events across several neighboring vesicles and leads to the formation of extended bilayer patches. Furthermore, adjacent bilayer patches usually coalesce in order to minimize their edge length [16]. Taken together, these effects increase the size of individual bilayer patches and the overall bilayer coverage and will, in the ideal case, lead to a complete SLB. However, it has been previously observed that even after the bilayer formation some vesicles remain intact near the edge of the bilayer patch suggesting that the edge almost needs to contact a vesicle to induce its rupture [26]. This finding demonstrates that the efficiency of edge-induced processes depends critically on the spatial arrangement of vesicles and bilayer patch [27].

4.1.3 Parameters Controlling the Formation of Supported Lipid Bilayers

Which pathway of vesicle deposition will be taken is essentially determined by the interplay of bilayer-support, interbilayer, and intrabilayer interactions [28]. In principle, the relative contribution of these interactions will be susceptible to the nature of the support (its surface charge, chemical composition and roughness), the lipid vesicles (their composition, charge, size, and physical state), as well as the aqueous environment (its composition, pH and ionic strength). In the following, we will outline some essential experimental parameters that appear to control SLB formation.

- *Electrostatic Interactions*

Several studies have pointed out the influence of the charge of support and lipids as well as the ionic strength of the solution on the adsorption of vesicles [23, 29, 30]. It was observed that it is sufficient to vary the vesicle charge to change the pathways of vesicle deposition leading to different scenarios were vesicles do not adsorb, adsorb intact, and rupture spontaneously, respectively [23]. In this respect, adjustments in the pH or in the ionic strength represent the simplest way to optimize the formation of SLBs for a given surface and a given lipid composition [31].

- *Calcium Ions*

As a general trend, it was observed that calcium induce stronger vesicle-surface interaction reflecting in a lower critical coverage for the vesicle-to-bilayer transformation [32]. However, the ions do not only participate in the screening of charges, thereby modifying the electrostatic interactions, but they also directly interact, in often subtle ways, with surfaces and lipids, for example inducing different degrees of deformation of adsorbed vesicles [33]. Particularly strong effects were observed for phospholipid vesicles adsorbing on mica [34]. Often minor concentrations (mM and below) of the ion are sufficient to generate significant effects [35].

- *Solid Support*

The influence of solid substrate properties on the process of SLB formation is probably the most difficult parameter to unravel [36]. Several studies pointed out that an higher hydrophilic character is necessary to observed vesicle rupture and subsequent SLB formation [37]. Consequently, mica and silicon-based materials, such as glass, Si_3N_4, or silica, has demonstrated to be the best supporting materials for the preparation of SLBs [31]. Another thoroughly investigated surface parameter affecting the SLB formation is surface roughness. In this respect, it was observed that although vesicles generally follow support's corrugations being able to can form SLBs even on extreme rough or porous substrates, the kinetics of SLB formation and the quality, i.e. defects, of the final bilayer seem substantially affected under such conditions [38]. Moreover, it is reported in literature that even the SLB formation is susceptible to the surface preparation condition, e. g. high temperature baking, basic solutions exposure, plasma treatment, etc. [39].

4.1.4 Surface sensitive techniques for the study of SLB formation

A multitude of techniques, such as fluorescence microscopy [40], quartz-crystal microbalance with dissipation monitoring (QCM-D) [41], atomic force microscopy (AFM) [42], surface plasmon resonance (SPR) [43], and ellipsometry [44] has been used to investigate the SLB-formation process.
In particular, combined approaches with complementary technique allowed considerable advance in the field. For example, AFM and QCM-D techniques were applied to the analysis of vesicle adsorption and SLB formation on silica [23] giving access to spatially resolved structural information on the nanometer scale and overall adsorption and reorganization dynamics, respectively, the combination of both techniques has enabled the identification and characterization of several different SLB-formation pathways stressing the importance of electrostatic interactions in the SLB-formation process. Others have pointed out the complementary aspects between QCM-D and optical surface-sensitive methods, such as SPR [43] or ellipsometry: while optical methods allow measuring the dry mass of the adsorbed lipids, QCM-D provides not only the hydrated mass, but also a direct mean (the dissipation) to distinguish between different phases of the adsorbate-surface bound vesicles or bilayer patches.
Recently, a new high-surface sensitive technique so called localized surface plasmon resonance demonstrated has proven useful for tracking the kinetics of phospholipid vesicle adsorption and rupture on different substrates [45, 46]. On silicon oxide-coated nanostructures, acceleration in the time-resolved peak shift is observed when adsorbed vesicles fuse and rupture to form a supported lipid bilayer [47, 48]. This acceleration has been attributed to the fact that lipids in a supported lipid bilayer are, on average, nearer to the substrate than lipids in an adsorbed vesicle. In this contest, we used the LSPR technique in combination with QCM-D to investigate how pH affects the kinetics of interaction between vesicles and silicon oxide surfaces. In particular, in order to focus solely on the effects of pH, we fixed the other key parameters, including vesicle size, ionic strength, temperature,

lipid phase, and lipid composition. In this regard, POPC vesicles was selected because phosphocholine has a gel-fluid phase transition temperature (∼-10 °C) well below the experimentally temperature of 25 °C, thereby permitting rule out transition effects [49].

4.2 Materials and Methods

4.2.1 Substrate preparation

LSPR sensor chips (Insplorion AB, Göteborg, Sweden) with silicon oxide coating and QCM-D crystals (Q-sense AB, Gothenburg, Sweden) with silicon oxide coatings (QSX 303) were used as substrate. Immediately before any measurement, all sample were UV/ozone treated for 10 minutes followed by extensive rinsing with Milli-Q water.

4.2.2 Vesicle Preparation

1-Palmitoyl-2-oleoyl-sn-glycero-3-phosphocholine (POPC) was purchased from Avanti Polar Lipids (Alabaster, AL). For vesicle preparation, chloroform solution of POPC (10 mg/ml) was first dried using a gentle stream of nitrogen gas and subsequently allowed to dry overnight to remove traces of chloroform. The films were subsequently hydrated with Tris buffer (10 mM Tris, 150 mM NaCl, pH 7.4) at a nominal lipid concentration of 10 mg mL-1. Hydration was performed by heating the formulation three times within a 60 °C water bath (3 min) followed by vortex mixing (3 min). To increase size homogeneity of liposomes of different sizes, the vesicle formulation were extruded at room temperature with 21 cycles through 100 nm polycarbonate membranes. After extrusion, vesicle solutions were stored at 4 °C until experiment and used within 48 h.
For all subsequent experiments, the stock solutions were further diluted to a 0.1 mg/mL lipid concentration in order to follow each step of the SPB formation on a reasonable time scale (around 10 min) [50].
For preparation of the pH buffers used in this study, the original stock buffer was titrated with either sodium chloride or hydrochloric acid, and the solution pHs were measured before and after experiment to verify their stability. All aqueous solutions were prepared using high-resistivity (>18.2 MΩ cm) deionized water that had been treated with the Milli-Q filtration system (Millipore, Billerica, MA).

4.3 Results And Discussion

The formation of phospholipid bilayers were monitored in situ on SiO_2 surfaces by LSPR and QCM-D techniques using respectively an Insplorion XNano (Insplorion AB, Göteborg, Sweden) and a Q-Sense E1 (Q-sense, Goteborg, Sweden) instruments. In short, after docking the LSPR chip or mounting the QCM crystal, the measurement chamber was filled with buffer at a flow rate of 0.05 mL/min. The flow was then maintained at the same rate throughout the measurement. When a stable baseline was obtained, vesicles solution were injected into the measurement chamber. After the adsorption process approaches to equilibrium, the sensor surfaces were rinsed with buffer. The temperature was held constant at 25 °C during the experiments.

The efficacy of SLB deposition on SiO_2 sensor surfaces was assessed by performing ex situ Attenuated Total Reflectance Fourier Transform Infrared Spectroscopy (ATR-FTIR) by using an FT-IR spectrophotometer Tensor 27 (Bruker Daltonics Inc., MA, USA) equipped with a MIRacle Single Reflection Horizontal ATR Accessory (PIKE Technologies, WI, USA). As reference sample, we considered the IR transmission spectra of the POPC powder. The IR spectra for POPC adsorbed on sensor surface and for POPC powder are reported in Figure 29.

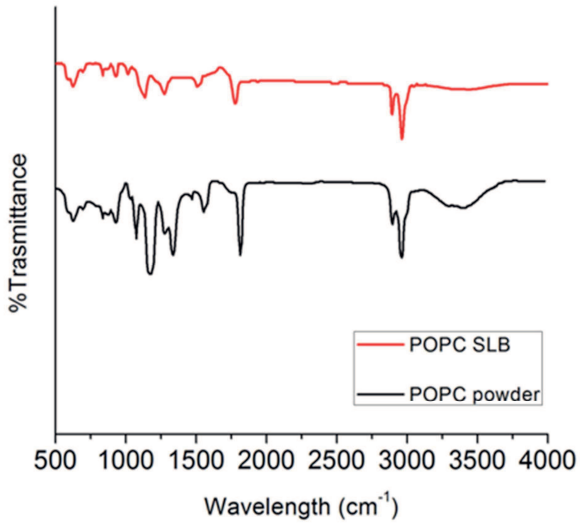

Figure 29. Infrared adsorption spectra for POPC powder (black solid line) and POPC adsorbed on SiO_2 sensor surface (red solid line).

The assignments corresponding to POPC included the CH_2 antisymmetric stretch and the CH_2 symmetric stretch at 2923 and 2853 cm^{-1}, respectively [51]. The C=O stretching vibration band of POPC was observed at about 1735 cm^{-1}[52]. The wave numbers 1463 and 1231 cm^{-1} were attributed to CH_2 scissoring, and the PO_2^- antisymmetric stretch [52]. The 1030-1090 cm^{-1} range included the PO_2^- symmetric stretch, and the CO-O-CH_2 symmetric stretch [52].

The dynamic of POPC vesicle adsorption at different pH as measured by LSPR technique are shows in Figure 30. The results show that both rate and pathway of vesicle adsorption are significantly affected by pH. In details, two different adsorption behaviors have been observed. For acidic pH, vesicles adsorption can be efficiently fitted with a simple exponential kinetic [53]. In this respect, no significant variation were observed in the corresponding time for the completion of the adsorption or in signal at saturation over the investigated acidic pH range within the experimental error of the technique. These results can be explained taking into account that both POPC vesicles and SiO_2 surface show low degree of ionization in acidic solution according to the respectively isoelectric point. So, we can conclude that, according with previous finding by [54], at acidic pH, vesicles adsorption are mainly driven by Van der Waals and steric forces that can be considered in first approximation as interaction independent of pH.

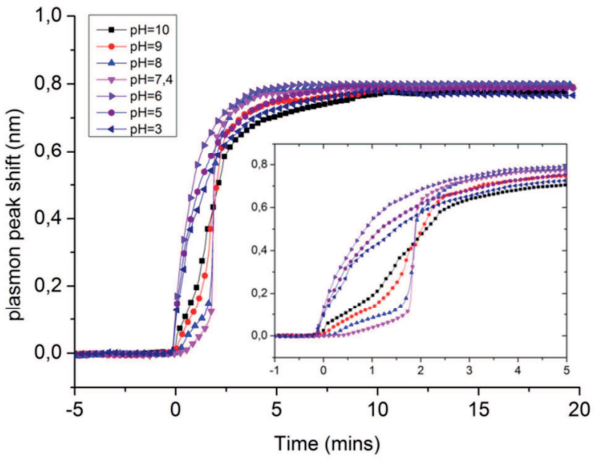

Figure 30. (Main plot) LSPR peak shift vs. time for POPC (0.10 mg/mL, 25 °C) vesicle adsorption on the SiO_2 surface as a function of the pH of the buffer: 3, 5, 6, 7.4, 8, 9, 10. (Inset) Enlarged portion of -1 to 5 minutes range showing the different adsorption kinetics as function of pH. Each curve is the mean of three independent experiments +/− standard deviation (SD) (unless mentioned otherwise).

Moving to higher pH, the vesicle adsorption behavior changes showing a two-step kinetic (see the inset in Figure 30) with an clear visible inflection point corresponding to the vesicle rupture event leading to the formation of supported lipid bilayer [48]. It is to note that as the pH increase, (between 7.4 and 10) the position of the aforementioned inflection point shifts toward longer time indicating that the adsorption is progressively slowed down. Moreover, we note that the first part of adsorption curves, i.e. before the “kink”, the peak shift increases linearly with time, in first approximation we performed a linearly fit of the adsorption curve in order to quantitative assess the effect of pH increase over the adsorption rate. Therefore, the slopes of the corresponding fitting line have been considered as a measurement of the vesicle adsorption rate and further they were plotted against pH values obtaining a linear dependence between pH values and slope of the fitting curves see Figure 31.

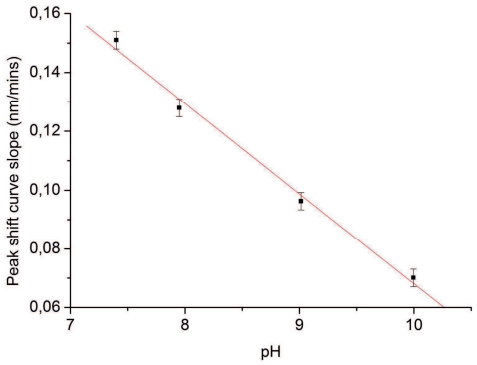

Figure 31. Peak shift curve slope as a function of pH over 7.4 -10 range for the first step of vesicle adsorption. Error bars represent standard error of the linear regression slope; R^2>90%;

These results indicates that the adsorption is driven by the electrostatic interactions. Furthermore, since the chosen vesicles are zwitterionic over the investigated pH range, while the SiO_2 surface zeta potential (ζ) decrease linearly with pH [55], over the same pH range, according to our data, surface zeta potential could be key parameter controlling the vesicle adsorption rate.

In order to verify the result obtained using LSPR, the same adsorption process has been further investigated using QCM-D technique. The corresponding adsorption curves are reported in Figure 32. Generally, QCM-D results agreed with once obtained using LSPR technique showing two different vesicle adsorption kinetic regimes for acidic and basic pH range. For a pH between 3 and 6, vesicle adsorbs without observation of the critical coverage point. On the contrary, in the case of a pH value between 7.4 and 10, a minimum in frequency could be visualized corresponding to the coverage at which adsorbed intact vesicles start to fuse and transform into a bilayer. Furthermore, for all measurements, the low values of energy dissipation indicate the formation of a stiff adlayer, suggesting that vesicles adsorption leads to the formation of the bilayer independently of pH conditions.

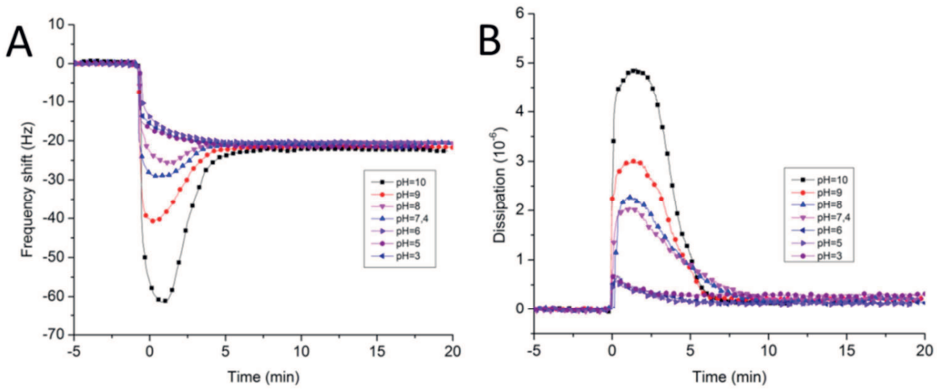

Figure 32. QCM-D frequency and dissipation response vs. time for POPC (0.10 mg/mL, 25 °C) vesicle adsorption on the SiO_2 surface as a function of the pH of the buffer: 3, 5, 6, 7.4, 8, 9, 10.

More in details, from the QCM-D traces is not possible to distinguish the first part of adsorption kinetics, i.e. before vesicle critical coverage is reached, varying the pH over 7.4-10. On the contrary, the second part of adsorption curves, i.e. as the vesicles fuse to a bilayer, show a clear dependence of pH with the time to signal reach equilibrium (i.e. 95 % of saturation frequency value) increase linearly as a function of pH values (see Figure 33).

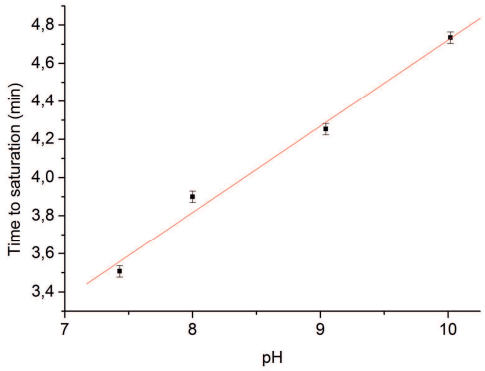

Figure 33. Time to reach saturation as a function of pH over 7.4 -10 range for vesicle adsorption measured by QCM-D

Moreover, the increase of depth of frequency minimum following the pH, indicated that an higher surface coverage is needed to start the vesicle rupture at more basic pH, suggesting that the process of bilayer formation is progressively less favored confirming the kinetic trend observed using LSPR.

4.4 Conclusions

In summary, LSPR technique in combination with QCM-D allows us to measure in situ changes in the kinetics of POPC vesicles adsorption onto SiO_2 surface as a function of pH. Our results clarify previous findings about the influence of pH onto lipid vesicles adsorption [54]. Two different adsorption regimes have been observed for acidic and basic conditions. For pH values lower than physiological limit, vesicles adsorption showed one-step exponential kinetics. Moreover, no significantly variation of the adsorption rate was observed over the investigated pH range, suggesting that the process is mainly controlled by Van der Waals interactions and steric forces. On the contrary, for alkaline pH, vesicles adsorb onto surface showing two-step kinetic consisting of a slow adhesion of intact vesicles onto surface followed by a fast vesicles rupture and fusion leading to a supported lipid bilayer. In particular, we observed that the rate of the first step slows down linearly with the increasing of pH, suggesting that the process is primarily driven by vesicle-surface electrostatic repulsion. The present findings clearly demonstrated the great potential of LSPR techniques for qualitative and quantitative investigation of adsorption kinetics useful for deeper understanding of interactions between soft matter and surfaces.

4.5 References

1. A. A. Spector, M. A. Yorek. Membrane lipid composition and cellular function. Journal of Lipid Research 26 (1985) 1015-1035.
2. J.S. O'Brien. Cell membranes—Composition: Structure: Function. Journal of Theoretical Biology. 15, (1967) doi:10.1016/0022-5193(67)90140-3.
3. K. Simons, W. L.C. Vaz. Model Systems, Lipid Rafts, and Cell Membranes. Annual Review of Biophysics and Biomolecular Structure 33 (2004) 269-295.
4. A. D. Bangham, M. W. Hill, N. G. A. Miller. Preparation and Use of Liposomes as Models of Biological Membranes. E. D. Korn (Ed.). Methods in Membrane Biology Korn, New York: Plenum Press, 1974, pp 1-68.
5. J. Song, Q. Cheng, S. Zhu, R. C. Stevens. “Smart” Materials for Biosensing Devices: Cell-Mimicking Supramolecular Assemblies and Colorimetric Detection of Pathogenic Agents. Biomedical Microdevices 4 (2002) 213-221.
6. C. J. Drummond, C. Fong. Surfactant self-assembly objects as novel drug delivery vehicles. Current Opinion in Colloid & Interface Science 4 (1999) 449–456.
7. M. Bally, K. Bailey, K. Sugihara, D. Grieshaber, J. Vörös, B. Städler. Liposome and Lipid Bilayer Arrays Towards Biosensing Applications. Small 6 (2010) 2481–2497.
8. S. Majd, M. Mayer. Hydrogel Stamping of Arrays of Supported Lipid Bilayers with Various Lipid Compositions for the Screening of Drug–Membrane and Protein– Membrane Interactions. Angew. Chem. Int. Ed. 44 (2005) 6697 –6700.
9. S. Cotrone, M. Ambrico, H. Toss, M. D. Angione, M. Magliulo, A. Mallardi, M. Berggren, G. Palazzo, G. Horowitze, T. Ligonzof, L. Torsi. Phospholipid film in electrolyte-gated organic field-effect transistors. Organic Electronics 13 (2012) 638-644.
10. M. Wang, W. Zhan. Mimicking Photosynthesis with Electrode-Supported Lipid Nanoassemblies. Acc. Chem. Res., Article ASAP DOI: 10.1021/acs.accounts.6b00420.
11. L. Zhou, G. Tan, C. Ning. Modification of biomaterials surface by mimetic cell membrane to improve biocompatibility. Front. Mater. Sci. 8 (2014) 325–331.
12. K. L. Weirich, J. N. Israelachvili, D. K. Fygenson. Bilayer Edges Catalyze Supported Lipid Bilayer Formation. Biophys J. 98 (2010) 85–92.
13. A. P. Girard-Egrot, L. J. Blum. Langmuir-Blodgett Technique for Synthesis of Biomimetic Lipid Membranes. D. K. Martin. Nanobiotechnology of Biomimetic Membranes. New York, NY: Springer, 2007.
14. G. Zhavnerkoa, G. Marletta. Developing Langmuir–Blodgett strategies towards practical devices. Materials Science and Engineering B 169 (2010) 43–48.
15. A. P. Le Brun, L. A. Clifton, S. A. Holt, P. J. Holden, J. H. Lakey. Chapter Eight – Deuterium Labeling Strategies for Creating Contrast in Structure–Function Studies of Model Bacterial Outer Membranes Using Neutron Reflectometry. Methods in Enzymology 566 (2016) 231–252.

16. R. P. Richter, R. Bérat, A. R. Brisson. Formation of Solid-Supported Lipid Bilayers: An Integrated View. Langmuir 22 (2006) 3497-3505.
17. I. P. McCabe, M. B. Forstner. Polymer Supported Lipid Bilayers. Open Journal of Biophysics 3 (2013) 59-69.
18. M. Montal, P. Mueller. Formation of Bimolecular Membranes from Lipid Monolayers and a Study of Their Electrical Properties. Proc. Nat. Acad. Sci. USA 69 (1972) 3561-3566.
19. C. Rossi, J. Chopineau. Biomimetic tethered lipid membranes designed for membrane-protein interaction studies. Eur Biophys J 36 (2007) 955–965.
20. D. D. Lasic. The mechanism of vesicle formation. Biochem. J. 256 (1988) 1-11.
21. F. Olson, C.A. Hunt, F.C. Szoka, W.J. Vail, D. Papahadjopoulos. Preparation of liposomes of defined size distribution by extrusion through polycarbonate membranes. Biochimica et Biophysica Acta (BBA) – Biomembranes 557 (1979) 9-23.
22. J.S. Dua, A. C. Rana, A. K. Bhandari. Liposome: Methods of Preparation and Applications. International Journal of Pharmaceutical Studies and Research. E-ISSN 2229-4619.
23. R. Richter, A. Mukhopadhyay, A. Brisson. Pathways of Lipid Vesicle Deposition on Solid Surfaces: A Combined QCM-D and AFM Study. Biophysical Journal 85 (2003) 3035–3047.
24. M. Stelzle, G. Weissmüller, E. Sackmann. On the application of supported bilayers as receptive layers for biosensors with electrical detection. J. Phys. Chem. 97 (1993) 2974–2981.
25. S. Gritsch, P. Nollert, F. Jahnig, E. Sackmann. Impedance spectroscopy of porin and gramicidin pores reconstituted into supported lipid bilayers on indium-tin-oxide electrodes. Langmuir 14 (1998) 3118–3125.
26. E. Reimhult, M. Zäch, F. HöökK, B. Kasemo. A Multitechnique Study of Liposome Adsorption on Au and Lipid Bilayer Formation on SiO2. Langmuir 22 (2006) 3313-3319.
27. A. M. Smith, M. Vinchurkar, N. Gronbech-Jensen, A. N. Parikh. Order at the Edge of the Bilayer: Membrane Remodeling at the Edge of a Planar Supported Bilayer Is Accompanied by a Localized Phase Change. J. Am. Chem. Soc. 132 (2010) 9320–9327.
28. T.K. Lind, M. Cárdenas. Understanding the formation of supported lipid bilayers via vesicle fusion—A case that exemplifies the need for the complementary method approach (Review). Biointerphases 11, 020801 (2016); doi: 10.1116/1.4944830.
29. M. Langner, K. Kubica. The electrostatics of lipid surfaces. Chem Phys Lipids 101 (1999) 3-35.
30. T. Cha, A. Guo, X.-Y. Zhu. Formation of Supported Phospholipid Bilayers on Molecular Surfaces: Role of Surface Charge Density and Electrostatic Interaction. Biophys J. 2006 Feb 15; 90(4): 1270–1274.
31. P. S. Cremer, S. G. Boxer. Formation and Spreading of Lipid Bilayers on Planar Glass Supports. J. Phys. Chem. B 103 (1999) 2554–2559.
32. M. Dacic, J. A. Jackman, S. Yorulmaz, V. P. Zhdanov, B. Kasemo, N. Cho. Influence of Divalent Cations on Deformation and Rupture of Adsorbed Lipid Vesicles. Langmuir 32 (2016) 6486−6495.

33. M. Karabaliev. Effects of divalent cations on the formation and structure of solid supported lipid films. Bioelectrochemistry 71 (2007) 54–59.
34. M. Beneš, D. Billy, A. Benda, H. Speijer, M. Hof, W. Th. Hermens. Surface-Dependent Transitions during Self-Assembly of Phospholipid Membranes on Mica, Silica, and Glass. Langmuir 20 (2004) 10129-10137.
35. J. Bentz, N. Diizgiineg, S. Nir. Kinetics of Divalent Cation Induced Fusion of Phosphatidylserine Vesicles: Correlation between Fusogenic Capacities and Binding Affinities. Biochemistry 22 (1983) 3320-3330.
36. R. Tero. Substrate Effects on the Formation Process, Structure and Physicochemical Properties of Supported Lipid Bilayers. Materials 5 (2012) 2658-2680.
37. R. Tero, H. Watanabe, T. Urisu. Supported phospholipid bilayer formation on hydrophilicity-controlled silicon dioxide surfaces. Phys. Chem. Chem. Phys. 8 (2006) 3885-3894.
38. J. Radler, H. Strey, E. Sackmann. Phenomenology and Kinetics of Lipid Bilayer Spreading on Hydrophilic Surfaces. Langmuir 11 (1995) 4539-4548.
39. K. J. Seu, A. P. Pandey, F. Haque, E. A. Proctor, A. E. Ribbe, J. S. Hovis. Effect of Surface Treatment on Diffusion and Domain Formation in Supported Lipid Bilayers. Biophysical Journal 92 (2007) 2445–2450.
40. J. M. Crane, L. K. Tamm. Fluorescence Microscopy to Study Domains in Supported Lipid Bilayers. A. M. Dopico (Ed.). Methods in Membrane Lipids. Totowa, NJ: Humana Press, 2007.
41. N. J. Cho, C. W. Frank, B. Kasemo, F. Höök. Quartz crystal microbalance with dissipation monitoring of supported lipid bilayers on various substrates. Nat Protoc. 5 (2010) 1096-1106.
42. M. Mingeot-Leclercq, M. Deleu, R. Brasseur, Y. F. Dufrêne. Atomic force microscopy of supported lipid bilayers. Nature Protocols 3 (2008) 1654 – 1659.
43. C. A. Keller, K. Glasmästar, V. P. Zhdanov, B. Kasemo. Formation of Supported Membranes from Vesicles. Phys. Rev. Lett. 84 (2000) 5443-5446.
44. R. P. Richter, J. L. K. Him, B. Tessier, C. Tessier, A. R. Brisson. Biophysical Journal 89 (2005) 3372-3385.
45. M. P. Jonsson, P. Jönsson, A. B. Dahlin, F. Höök. Supported lipid bilayer formation and lipid-membrane-mediated biorecognition reactions studied with a new nanoplasmonic sensor template. Nano Lett. 7 (2007) 3462−3468.
46. M. P. Jonsson, P. Jönsson, F. Höök. Simultaneous nanoplasmonic and quartz crystal microbalance sensing: analysis of biomolecular conformational changes and quantification of the bound molecular mass. Anal. Chem. 80 (2008) 7988−7995.
47. G. H. Zan, J. A. Jackman, S. –O. Kim, N.-J. Cho. Controlling lipid membrane architecture for tunable nanoplasmonic biosensing. Small 2014, 10, 4828.
48. E. M. Larsson, M. E. Edvardsson, C. Langhammer, I. Zoric, B. Kasemo. A combined nanoplasmonic and electrodeless quartz crystal microbalance setup. Rev. Sci. Instrum. 80 (2009) 125105.

49. H. Ichimori, T. Hata, H. Matsuki, S. Kaneshina. Effect of unsaturated acyl chains on the thermotropic and barotropic phase transitions of phospholipid bilayer membranes. Chem. Phys. Lipids 100 (1999) 151–164.
50. I. Reviakine, A. Brisson. Formation of Supported Phospholipid Bilayers from Unilamellar Vesicles Investigated by Atomic Force Microscopy. Langmuir 16 (2000) 1806–1815
51. J. Zhao, L. K. Tamm. FTIR and fluorescence studies of interactions of synaptic fusion proteins in polymer-supported bilayers. Langmuir 19 (2003) 1838–1846.
52. L. K. Tamm, S. A. Tatulian. Infrared spectroscopy of proteins and peptides in lipid bilayers. Quarterly Reviews of Biophysics 3 (1997) 365–429.
53. Z. Zheng, D. Stroumpoulis, A. Parra, L. Petzold, M. Tirrell. A Monte Carlo simulation study of lipid bilayer formation on hydrophilic substrates from vesicle solutions. J Chem Phys. 124 (2006) 64904.
54. B. Seantier, C. Breffa, O. Félix, G. Decher. Dissipation-Enhanced Quartz Crystal Microbalance Studies on the Experimental Parameters Controlling the Formation of Supported Lipid Bilayers. J. Phys. Chem. B 109 (2005) 21755-21765.
55. N. K. Penta, P. R. D. Veera, S. V. Babu. Charge Density and pH Effects on Polycation Adsorption on Poly-Si, SiO2, and Si3N4 Films and Impact on Removal During Chemical Mechanical Polishing. ACS Appl. Mater. Interfaces 3 (2011) 4126–4132.

CHAPTER 5.

PRELIMINARY EXPERIMENTS ON PH-INDUCED REVERSIBLE STRETCHING-CONTRACTING MODES IN STIMULI-RESPONSIVE PEPTABIOTICS.

5.1 Introduction

5.1.1 pH-responsive polymers

Stimuli-responsive polymers are defined as polymers that undergo relatively large and abrupt, physical or chemical changes in response to small external changes in the environmental conditions [1]. These polymer systems might recognize a stimulus as a signal, judge the magnitude of this signal, and then change their chain conformation in direct response [2]. At macromolecular level, polymer chains can be altered in different ways, including change in hydrophilic-to-hydrophobic balance, conformation, solubility, degradation, and bond cleavage, and these, in turn, will cause detectable behavioral changes to self-assembled structures [3]. Generally, the location of responsive moieties or functional includes, but not are limited to: side chains on one of the blocks, chain end-groups, of junctions between blocks [4].

There are many different stimuli to modulate the response of polymer systems. These stimuli could be classified as either physical or chemical stimuli. Physical stimuli (light, temperature, ultrasound, magnetic, mechanical, electrical) usually modify chain dynamics, i.e. they affect the level of various energy sources and alter molecular at critical onset points [5]. Chemical stimuli (solvent, ionic strength, electrochemical, pH) modulate molecular interactions, whether between polymer and solvent molecules, or between polymer chains [6]. In the following, the most studied class of pH responsive polymeric system has been briefly reviewed.

Polymers containing ionizable functional groups that respond to change in pH are called pH-sensitive polymers [7]. By generating the charge along the polymer backbone, the electrostatic repulsion results in an increase in the hydrodynamic volume of the polymer [8]. Consequently, changes in the environmental pH thus lead to conformational changes of the soluble polymers and a change in the swelling behavior of the hydrogels when ionizable groups are linked to the polymer structure [9]. pH-responsive polymer can be classified in polyacids and polybasic. Polyacids bearing the carboxylic group with pk_a's of around 5–6, are the most representative weak polyacids [10]. Among polyacids, poly(acrylic acid) (PAAc) [11] and poly(methacrylic acid) (PMAAc) [12] have been most frequently reported as pH responsive polyacids. Their carboxylic pendant groups accept protons at low pH, while releasing them at high pH. Therefore, they are transformed into polyelectrolytes at high pH with

electrostatic repulsion forces between the molecular chains (see Figure 34). Typical polybases are poly(N,N0-diethyl aminoethyl methacrylate) (PDEAEMA) [13] and Poly(4 or 2-vinylpyridine) (PVP) [14]. PDEAEMA homopolymer undergoes an abrupt precipitation above pH 7.5 due to the deprotonation of amino groups, followed by hydrophobic molecular interactions between the aliphatic substituents at the end of the amine group [13] (see Figure 34). Similarly, PVP undergoes a phase transition under pH 5 owing to deprotonation of pyridine groups [14].

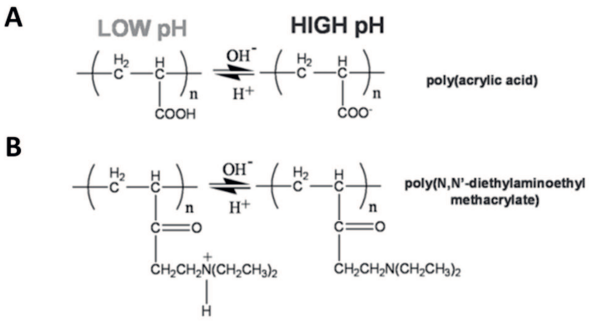

Figure 34. Example of a weak polyacid (A), that exhibits a collapsed conformation a low pH and an expanded state at high pH; an example of a weak polybase (B) is also shown when an opposite behavior is observed [15].

Besides synthetic non-biodegradable polymers, such as the ones shown in Figure 34, natural-based polyelectrolytes especially polysaccharides show pH responsive phase transition. Two examples of this class of molecules are Alginate and Chitosan. Alginate is an acidic polysaccharide bearing carboxylic groups, whose pk_a is at 3–4 (see Figure 35 A) [16]. Chitosan is the N-deacetylated derivative of chitin and is shown as a copolymer consisting of 2-acetamido-2-deoxy-b-D-glucopyranose and 2-amido-2-deoxy-b-D-glucopyranose (see Figure 35 B). The amine groups in chitosan gain protons at low pH and release them at high pH. Therefore, this biopolymer shows precipitation over pH 6–6.2 due to high hydrogen bonding strength between –OH groups and uncharged amine groups in chitosan chains [17].

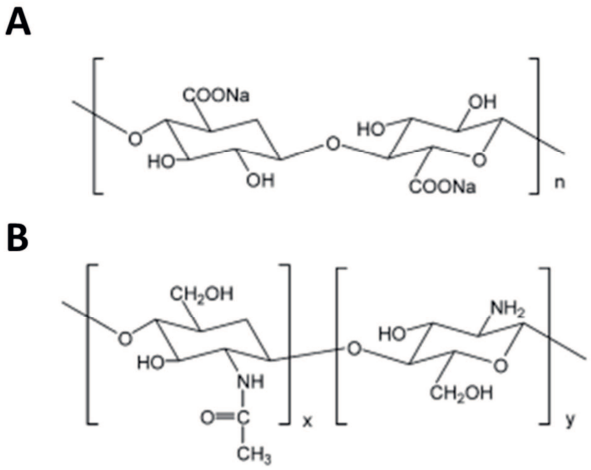

Figure 35. (A) Sodium alginate and (B) chitosan [18].

Another class of pH-responsive biopolymer frequently investigated are synthetic polypeptides [19]. They are unique among polymeric materials. Their structure is stabilized via hydrogen bond formation, as well as hydrophobic and electrostatic interactions [20]. Various types of synthetic proteins with precisely folded three-dimensional structures have been designed and synthesized [21]. In addition, ionizable polypeptides undergo a helix-coil structure transition [22]; this transition may be useful to aid in the design and synthesis of stimuli-responsive materials [22]. The most used ionizable pendant group include cysteine (pk_a=8.4), aspartic acid (pk_a=3.9), glutamic acid (pk_a=4.1), histidine (pk_a=6.0), lysine (pk_a=10.5), or arginine (pk_a=12.5) [18].

Adjusting the appropriate critical pH (pH*), at which reversible conformational changes (usually followed by phase transitions) of polymer chains occur, is an important factor for the pH responsive polymer-based application [23]. The intrinsic pk_a values of an ionizable moiety should be adopted as a first consideration in the selection of a proper pH-responsive polymer for the desired application [18]. If the ranges of pH sensitivity are focused around physiological pH or below, poly(glutamic acid) and poly (histidine) are the most available candidates as pH responsive polypeptides [24, 25]. On the contrary, poly(L-lysine) undergoes a pH-responsive phase transition, its pk_a is too high to use in biomedical applications requiring its transition near physiological pH. However, the conformational transition, which occurs at pH*, does not exactly occur at the pk_a [18]. This transition is indeed governed by the balance between electrostatic repulsion and hydrophobic interactions [23]. Consequently, the characterization pH-responsive behavior of novel synthetized peptide has to be investigated experimentally.

5.1.2 Peptabolids: from antimicrobial agent to novel functional materials

Peptaibols are secondary metabolites with molecular weights in the range of 500 – 2200 Da [26]. They are composed of five (peptaibolin) to 20 (e.g., atroviridin, alamethicin, suzukacillin, paracelsin, polysporin) [27] amino acids, and contain non-proteinogenic amino acid residues like a-aminoisobutyric acid (Aib), occurring in high proportions and representing characteristic building blocks of the structure. The N-terminal residues of peptaibols are usually acetylated [28], and an amino alcohol (phenylalaninol, valinol, leucinol, isoleucinol, or tryptophanol) is linked by a peptide bond at the C-terminal end [29]. The three-dimensional (3D) structure of peptaibols is characterized predominantly by one type of a helical motif, including α-helix, 3_{10}-helix, and β-bend ribbon spiral [30]. The original name 'peptaibol' has been constructed from the names of the three characteristic components: peptide, Aib, and amino alcohol [31].
Peptaibols show interesting physico-chemical properties, including the formation of pores in bilayer lipid membranes [32], and a wide spectrum of biological activities, including antibacterial [33], antifungal [34], and antiviral effects [35], immunosuppressive [33] and neuroleptic properties [36], as well as elicitation of plant-systemic resistance [37]. The beginning of peptaibol research dates back to the late 1960s, when the first members of this peptide family alamethicin (ALM), have been isolated from the fungus trichoderma viride [31]. ALM consists of 19 amino acids and 1 amino alcohol [31]. Two native forms occur, the R_f30 form with a Glu residue at position 18 and the R_f50 form in which this Glu is replaced by Gln, making the peptide electrically neutral [38]. The 20 amino acids sequence for R_f30 is [39]:

Ac – Aib – L-Pro – Aib – L- Ala – Aib – L-Ala – L-Gln – Aib – L-Val – Aib – L-Gly – L-Leu – Aib – L-Pro – L-Val – Aib – Aib – L-Glu – L-Gln – L-Phl

Alamethicin contains the non-proteogenic amino acid 1-amino isobutyric acid (Aib, or α-methylalanina) [40] and the preponderance of this rather unusual amino acid is the reason for the peptide name [31].
The Aib residues restrict the conformational space so that an α-helical peptide structures is preferred [40]. Due to the fact that Aib is achiral, left- and right-handed helical conformation are likely, however the presence of L-amino acids confers preference for the right-handed helices [31]. The central Gly-X-X-Pro motif forms a molecular hinge between the two α-helical segments to the left and to the right (see Figure 36) [41].

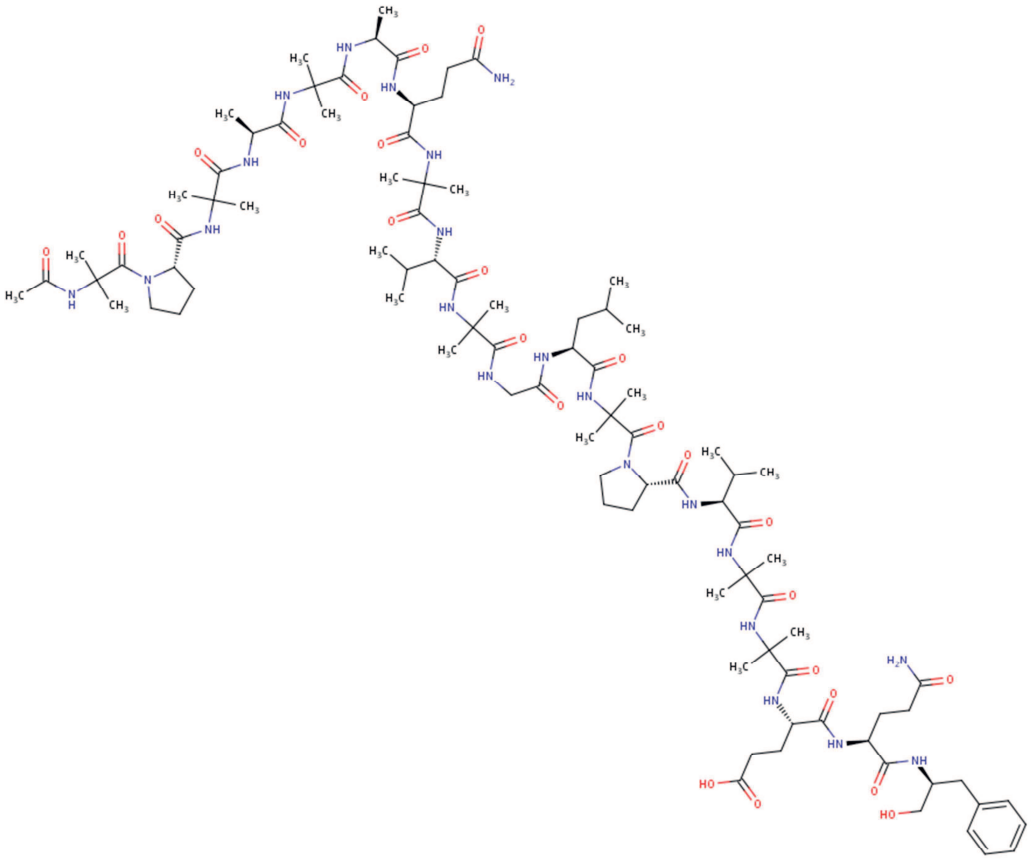

Figure 36. Alamethicin [RCSB Protein Data Bank]

Alamethicin is amphiphilic because its hydrophilic group are at the C-terminus or delineate a narrow longitudinal hydrophilic sector (residues Gln7, Gln11, Gln18, and exposed backbone of Aib10 and Gly11 because of the kink) [42]. The majority of the amino acid residues, including N-terminus, are of hydrophobic nature [43].

Peptaibols naturally occur as mixtures of isoforms, and more than 250 sequences are actually known [28]. They are divided into three subclasses, which are (i) the long sequence peptaibols with 18–20 amino acid residues, e.g. alamethicins, (ii) the short-sequence peptaibols with 11–16 residues exemplified by harzianins [44] or zervamicins [45], and (iii) the lipopeptaibols [46] with 7 or 11 residues, the N terminus of which is acylated by a short fatty acid chain such as octanoic acid instead of acetic acid represented by TrichoginA IV.

Trichogin GA IV (TCG) is an amphipathic peptide that consists of a sequence of 10 amino acid residues with three nonproteogenic helicogenic α-aminoisobutyric acid (Aib) residues, the 1,2 amino alcohol leucinol at the C-terminus, and a lipophilic n-octanoyl group at the N-terminus [47].
The primary structure of the N- and C-blocked 10-amino acid peptide trichogin GA IV is as follows [47]:

1 10
n-Oct-Aib-Gly-Leu-Aib-Gly-Gly-Leu-Aib-Gly-Ile-Lol

Like most lipopeptaibols, TCG exhibits remarkably valuable properties, such as well-developed helicity, amphiphilicity, stability to proteolytic degradation, and short main-chain length [48]. These properties render them intriguing lead compounds in the search of candidates as novel, potent antibacterial agents [48].
In the last years, synthetic peptides are emerging as versatile materials whose function can be programmed to perform specific tasks via chemical functionalization. In this respect, the preliminary result here reported, demonstrated that two novel TCG analogs, i.e. Lipoic-[$Lys^{2,5,6,9}$]- TCG and Lipoic-{[$Lys^{2,5,6,9}$]-TCG]}$_2$-Lol in which, respectively, four and eight Lysines positive charged residues have been introduced, are able to reversibly switch its conformation between two, well-defined, different helical conformations in response to pH variations. In particular, it is shown that these peptides can contract and stretch in response to a short range of pH variation. The peptides were anchored to the gold surfaces through a N-terminal lipoic acid moiety. The loading and the conformational switching properties of the surface-bound peptides were investigated in situ in real time by means of Localized Surface Plasmon Resonance. The result clearly suggested that TCG analogs can be promising candidate as building blocks for the preparation novel functional materials.

5.2 Materials and Methods

5.2.1 Chemicals and Peptides

All chemicals were purchased from Sigma-Aldrich (St. Louis, MO) and used without further purification except when mentioned specifically. Lipoic- TCG -OMe, Lipoic-[$Lys^{2,5,6,9}$]- TCG and Lipoic-{[$Lys^{2,5,6,9}$]-TCG]}$_2$-Lol were provided by Dr. Marta De Zotti (Department of Chemistry, University of Padua, Italy) (see Figure 37). All peptide sample solution (1 mM) were prepared dissolving the peptide lyophilized with ethanol. Phosphate buffer stock solution (PBS) was prepared by dissolving 1 tablet in 200 mL of ultrapure water (processed by a Millipore system with 18.2 M Ω resistivity), resulting in a solution ionic strength of 10^{-2} M for the phosphate salts, $2.7x10^{-3}$ M for potassium chloride, and 0.137 M for sodium chloride (pH 7.4 at 25°C). PBS solutions adjusted to pH 3 or 11 were prepared by titrating aliquots from the same stock (pH 7.4) using 0.1N HCl or NaOH solutions.

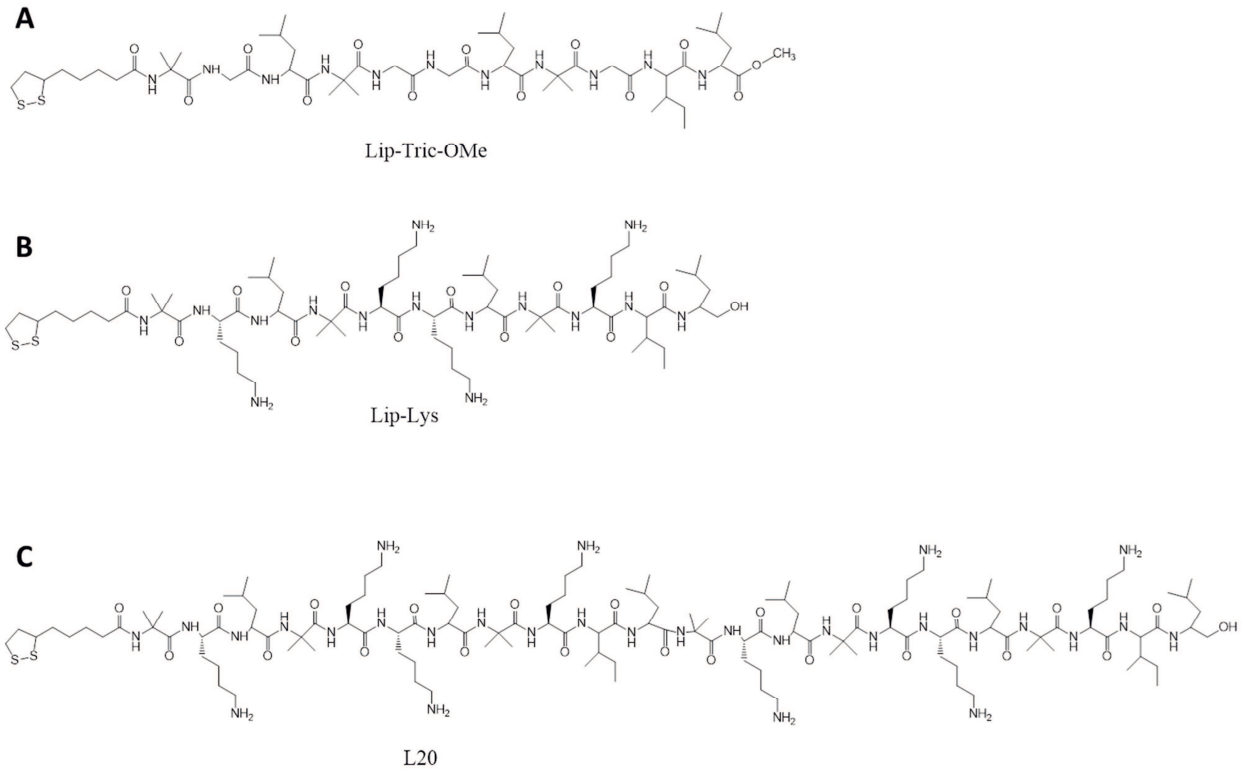

Figure 37. Structures of the peptides (A) Lip-Tric-OMe, (B) Lip-Lys and (C) L20.

5.2.2 Functionalization of the gold nanoparticle array

LSPR sensor chips (Insplorion AB, Göteborg, Sweden) consisting of a glass slide decorated with gold nanodisks [49] were used as substrate. Immediately before any measurement, all sample were UV/ozone treated for 10 minutes followed by extensive rinsing with ethanol. The sensor chip were immersed for 18 h in a 1 mM ethanol solution of peptide in order to anchor the peptide to the gold nanodisks surface. After incubation the sensor chip were gently rinsed with ethanol and dried in a stream of nitrogen.

5.2.3 LSPR measurements

The dry thickness of the grafted peptide layers was measured using an Insplorion XNano instrument (Insplorion AB, Göteborg, Sweden). A detailed description of the experimental apparatus is reported elsewhere [50]. In details, we measured the adsorption spectra of gold nanodisk array (henceforth indicated as plasmon peak) on the surface of LSPR sensor chip before and after the peptide grafting (see Figure 38).

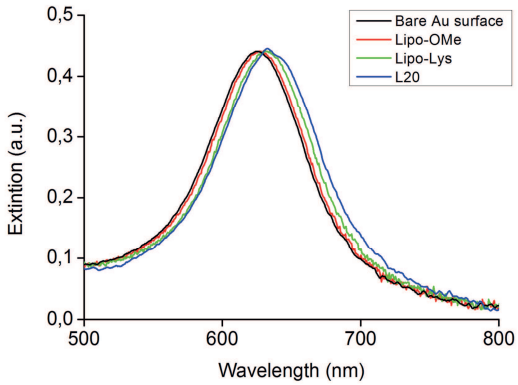

Figure 38. Adsorption spectra of gold nanodisk array on the surface of LSPR sensor chip before and after the peptide grafting.

Assuming that the grafted layer were uniform, the peak shift values (see Table 2) were converted in optical thickness according to the following equation [51]:

$$\Delta\lambda = S\left[1 - e^{-\frac{t}{L}}\right]\left(n_{peptide} - n_{AIR}\right) \qquad Eq.58$$

where S = 210 nm/RIU is the bulk refractive sensitivity of the LSPR sensor (previously determined (ref)), L = 27.2 nm the decay length of the LSPR evanescent wave according to sensor specification, t is the adlayer thickness, $n_{peptide}$=1.46 and n_{AIR} =1.00 are respectively the refractive index used for proteinaceous layer [52] and the air medium.

Table 2. LSPR peak shift and optical thickness for the peptide grafted on the gold nanodisks surface. (The reported values is the mean of three independent depositions +/− standard deviation).

Peptide	Peak shift (nm)	Dry Thickness (nm)
Lip-OMe	3.0±0.2	1.3±0.2
Lip-Lys	3.5±0.1	1.8±0.1
L20	6.0±0.1	3.1±0.1

The same LSPR instrument equipped with microfluidic flow cell was then utilized to quantify in real time and in situ the pH-induced swelling and collapse of the peptide layers. In details, the acid buffer (pH 3) was infused into the LSPR cell at a constant velocity of 0.05 ml/min for 20 min. Subsequently, the solution was exchanged to the basic buffer and thereafter back to acidic buffer, completing one cycle of peptide swelling/collapse. For each type of peptide, up to six cycles were performed. For

measurements of the swollen thicknesses of the peptide layer the, we measured the plasmon peak shift following the acid to basic buffer exchange. Then this value was converted in optical thickness according to Eq. 58. However, in this case, we substituted the refractive index of air medium with the corresponding value for PBS solution with 50 mM potassium phosphate (n_{buffer}=1.335).

5.3 Result and Discussion

The pH switching behavior of three Trichogin GA IV analogs peptides anchored to the surface of gold nanodisk array sensor chip was investigated using LSPR technique. In Figure 39 are reported the spectral position of the plasmon peak wavelength as a function of time and pH of the solution in contact with the sensor.

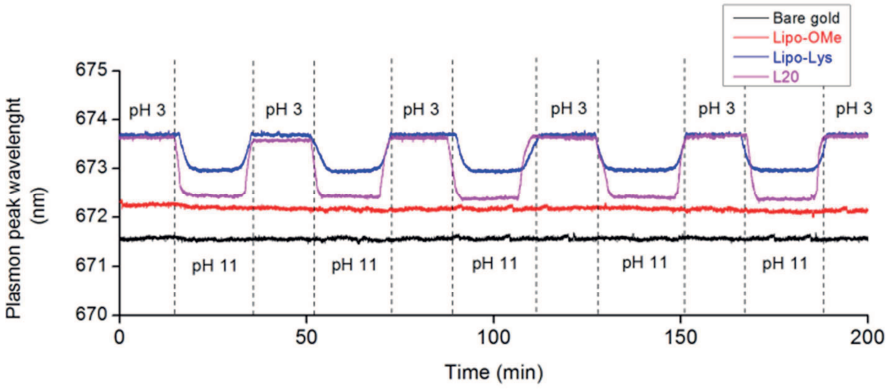

Figure 39. Change in plasmon peak wavelength over time when pH of buffer flow is changed from acidic pH (3) to basic pH (11).

From Figure 39 it is evident that both peptides bearing Lysine residues, i.e. Lipo –Lys and L20, are pH sensitive. When they are exposed to basic solution (pH 11), a steep decrease in plasmon peak wavelength is measured. The peak position returns to almost the same level as the one before basic solution is injected if the pH 11 buffer is replaced by the pH 3 buffer. Therefore, this indicate that observe process is totally reversible. Even after many cycles no hysteresis was observed. The response time of the peptide layers upon changing the pH is fast. The peptide brush reached the equilibrium swollen/collapsed within 1 min and was stable in the following 20 min. We attribute the fast response to the peculiar structure of the LSPR sensor consisting in gold nanodisk with an interparticle pitch larger compared to the nanodisk diameters. So that this structure facilitates the diffusion of H_3O^+ or (OH^-) toward the peptide layer. On the contrary, the LSPR curve for the bare gold nanodisk and for Lipo-OMe shown to be insensitive to pH changes. This last finding rules out that the observed pH responsive behavior being due to bulk refractive index changes related with the buffer or linked with the response of the peptide backbone. Consequently, we interpreted the LSPR curve for Lipo –Lys and L20 as a collapse of the peptide layer, leading to a decreased refractive index near the gold nanostructure a subsequent blue shift of the plasmon peak. A similar response has been reported Poly(acrylic acid) (PAA)polymer brushes collapsing due to exposition to basic pH solution, and it was

interpreted as mainly a thickness related effect. Here, we see a decrease in the peak shift upon increase of pH and thus interpret this as mainly a layer thickness effect. Furthermore, it is to note that for L20, i.e. Trichogin GA IV dimer analog, the peak shift measured exchanging the solution from pH 3 to 11 (2.4±0.1 nm) is almost twice that for Lipo-Lys , i.e. Trichogin GA IV analogs, (1.1±0.1 nm). These values converted in thickness are respectively 4.5±0.1 nm and 2.0±0.1 nm, so this suggests that the response in thickness depend on the number of lysine lateral chain.

From a mechanistic point of view, the pH dependent swelling/collapse behavior observed for the peptide layers has been interpreted as a consequence of the degree of dissociation of the amino moieties in the lysine lateral chains. In acidic medium (pH 3), the amino group are fully protonated, so peptide is forced to assume an extended conformation in order to minimize the electrostatic repulsion between the positively charged side chains. With the increase in pH, the amino group are neutral, and therefore the peptide is in a collapsed state (see Figure 40).

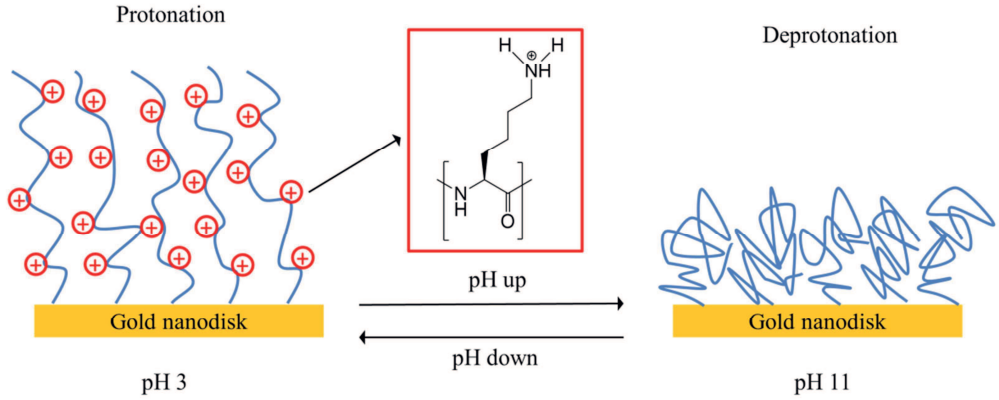

Figure 40. Reversible conformation change of Lipo-Lys (or L20) at different pH. At low pH, primary amine groups are protonated and the peptide chain are extended (left) because of electrostatic repulsion force. At high pH, the ionizable groups are deprotonated and the electrostatic repulsion force disappear within the peptide chain. That cause the collapse of the peptide chain (right).

5.4 Conclusions

Synthetic polypeptides, consisting of amino acids bearing ionizable pendant groups, behave as pH-responsive systems offering the possibility of achieving rapid and reversible switching between conformations, which can be induced locally, making them ideal candidates for miniaturized devices with fast response times [31]. Here, we reports preliminary result obtained from the study of stimuli-responsive smart surfaces, formed by gold substrates decorated with trichogin GA IV and two of its positively-charged analogs, i.e. Lipo-Lys and L20, in which four and eight Lysines positive charged residues have been introduced respectively. The peptides were anchored to the surfaces gold nanodisks of an LSPR sensor chip through a N-terminal lipoic acid moiety. The surface-bound peptides exhibit reversible and rapid switching between conformations and can withstand several cycles of swelling and collapsing with no significant loss from the surfaces. The swelling factors, i.e. difference maximum thickness-minimum thickness, determined for the L20 peptide is almost twice than that for Lipo-Lys, suggesting that it can be tune by varying the number of Lysine residues introduced in the peptide backbone. Furthermore, LSPR technique was successfully used to follow gold-tethered peptides conformational changes. Indeed, peptide chains collapsing and extension due to pH caused clear change in the plasmon peak wavelength. The results shown here clearly demonstrated the potential of the LSPR technique in the field of stimuli-responsive, smart or switchable interfaces.

5.5 References

1. B. Jeong, A. Gutowska. Lessons from nature: stimuliresponsive polymers and their biomedical applications. TRENDS in Biotechnology 20 (2002) 305-311.

2. J.-K. Chen, C.-J. Chang. Fabrications and Applications of Stimulus-Responsive Polymer Films and Patterns on Surfaces: A Review. Materials 7 (2014) 805-875.

3. W. B. Liechty, D. R. Kryscio, B. V. Slaughter, N. A. Peppas. Polymers for Drug Delivery Systems. Annu Rev Chem Biomol Eng. 1 (2010) 149–173.

4. E. Cabane, X. Zhang, K. Langowska, C. G. Palivan, W. Meier. Stimuli-Responsive Polymers and Their Applications in Nanomedicine. Biointerphases 7 (2012) 9.

5. M. A. Cohen Stuart, W. T. S. Huck, J. Genzer, M. Müller, C. Ober, M. Stamm, G. B. Sukhorukov, I. Szleifer, V. V. Tsukruk, Marek Urban, F. Winnik, S. Zauscher, I. Luzinov, S. Minko. Emerging applications of stimuli-responsive polymer materials. Nature Materials 9 (2010) 101-113.

6. C. de las Heras Alarcón, S. Pennadam, C. Alexander. Stimuli responsive polymers for biomedical applications. Chem. Soc. Rev. 34 (2005) 276–285.

7. S. Dai, P. Ravib, K. C. Tam. pH-Responsive polymers: synthesis, properties and applications. Soft Matter, 4 (2008) 435-449.

8. S. R. Tonge, B. J. Tighe. Responsive hydrophobically associating polymers: a review of structure and properties. Adv Drug Deliv Rev 53 (2001) 109–122.

9. H. Almeida, M. H. Amaral, P. Lobão. Temperature and pH stimuli-responsive polymers and their applications in controlled and self-regulated drug delivery. Journal of Applied Pharmaceutical Science 2 (2012) 01-10.

10. S.F. Medeirosa, A.M. Santosa, H. Fessib, A. Elaissarib. Stimuli-responsive magnetic particles for biomedical applications. International Journal of Pharmaceutics 403 (2011) 139–161.

11. O. E. Philippova, D. Hourdet, R. Audebert, A. R. Khokhlov. pH-Responsive Gels of Hydrophobically Modified Poly(acrylic acid). Macromolecules 30 (1997) 8278-8285.

12. V. Kozlovskaya , E. Kharlampieva , M. L. Mansfield, S. A. Sukhishvili. Poly(methacrylic acid) Hydrogel Films and Capsules: Response to pH and Ionic Strength, and Encapsulation of Macromolecule. Chem. Mater. 18 (2006) 328–336.

13. J.-T. Sun, C.-Y. Hong, C.-Y. Pan. Fabrication of PDEAEMA-Coated Mesoporous Silica Nanoparticles and pH-Responsive Controlled Release. J. Phys. Chem. C 114 (2010) 12481–12486.

14. T. J. Martin, K. Procházka , P. Munk , S. E. Webber. pH-Dependent Micellization of Poly(2-vinylpyridine)-block-poly(ethylene oxide). Macromolecules 29 (1996) 6071–6073.

15. J. F. Mano. Stimuli-Responsive Polymeric Systems for Biomedical Applications. ADVANCED ENGINEERING MATERIALS 10 (2008) 515-527.

16. J. H. Kim, S. B. Lee, S. J. Kim, Y. M. Lee. Rapid temperature/pH response of porous alginate-g-poly(N-isopropylacrylamide) hydrogels. Polymer 43 (2002) 7549-7558.

17. J. Mao, S. Kondu, H.-F. Ji, M. J. McShane. Study of the Near-Neutral pH-Sensitivity of Chitosan/Gelatin Hydrogels by Turbidimetry and Microcantilever Deflection. Biotechnol Bioeng. 95 (2006) 333–341.

18. E. S. Gil, S. M. Hudson. Stimuli-reponsive polymers and their bioconjugates. Prog. Polym. Sci. 29 (2004) 1173–1222.

19. S. Chaterji, I. K. Kwon, K. Park. Smart Polymeric Gels: Redefining the Limits of Biomedical Devices. Prog Polym Sci. 2007 Aug; 32(8-9): 1083–1122.

20. M. A. Quadir, S. W. Morton, Z. J. Deng, K. E. Shopsowitz, R. P. Murphy, T. H. Epps, P. T. Hammond. PEG–Polypeptide Block Copolymers as pH-Responsive Endosome-Solubilizing Drug Nanocarriers. Mol Pharm. 11 (2014) 2420–2430.

21. Y. Ito, Y. Ochiai, Y. S. Park, Y. Imanishi. pH-Sensitive Gating by Conformational Change of a Polypeptide Brush Grafted onto a Porous Polymer Membrane. J. Am. Chem. Soc. 119 (1997) 1619-1623.

22. L. Franco, L. J. del Valle, J. Puiggalì. Smart systems related to polypeptide sequences. AIMS Materials Science 3 (2016) 289-323.

23. S. K. Filippov, L. Starovoytova, C. Koňak, M. Hrubý, H. Mackova, G. Karlsson, P. Štěpánek. pH Sensitive Polymer Nanoparticles: Effect of Hydrophobicity on Self-Assembly. Langmuir 26 (2010) 14450–14457.

24. G. H. Gao, Y. Li, D. S. Lee. Environmental pH-sensitive polymeric micelles for cancer diagnosis and targeted therapy. Journal of Controlled Release 169 (2013) 180–184.

25. R. P. Johnson, S. Uthaman, J. V. John, H. R. Lee, S. J. Lee, H. Park, I.-K. Park, H. Suh, I. Kim. Poly(PEGA)-b-poly(L-lysine)-b-poly(L-histidine) Hybrid Vesicles for Tumoral pH-Triggered Intracellular Delivery of Doxorubicin Hydrochloride. ACS Appl. Mater. Interfaces 7 (2015) 21770−21779.

26. T. Marik, C. Várszegi, L. Kredics, C. Vágvölgyi, A. Szekeres. Mass spectrometric investigation of alamethicin. Acta Biologica Szegediensis 57 (2013)109-112.

27. A. Szekeres, B. Leitgeb, L. Kredics, Z. Antal, L. Hatvani, L. Manczinger, C. Vágvölgyi. Peptaibols and related peptaibiotics of Trichoderma. A review. Acta Microbiol Immunol Hung. 52 (2005) 137-68.

28. A. Wiest, D. Grzegorski, B.-W. Xu, C. Goulard, S. Rebuffat, D. J. Ebbole, B. Bodo, C. Kenerley. Identification of Peptaibols from Trichoderma virens and Cloning of a Peptaibol Synthetase. The Journal of Biological Chemistry 277 (2002) 20862-20868.

29. T. Marik, A. Szekeres, C. Várszegi, D. Czifra, C. Vágvölgyi, L. Kredics. Rapid bioactivity-based pre-screening method for the detection of peptaibiotic-producing Trichoderma strains. Acta Biologica Szegediensis 57 (2013) 1-7.

30. M. Crisma, F. Formaggio, A. Moretto, C. Toniolo. Peptide helices based on alpha-amino acids. Biopolymers 84 (2006) 3-12.

31. B. Leitgeb, A. Szekeres, L. Manczinger, C. Vágvölgyi, L. Kredics. The History of Alamethicin: A Review of the Most Extensively Studied Peptaibol. CHEMISTRY & BIODIVERSITY 4 (2007) 1027-1051.

32. S. Rebuffat, H. Duclohier, C. Auvin-Guette, G. Molle, G. Spach, B. Bodo. Membrane-modifying properties of the pore-forming peptaibols saturnisporin SA IV and harzianin HA V. FEMS Microbiol Immunol. 5 (1992) 151-160.

33. S. Ayers, B. M. Ehrmann, A. F. Adcock, D. J. Kroll, E. J. Carcache de Blanco, Q. Shen, S. M. Swanson, J. O. Falkinham, M. C. Wani, S. M. Mitchell, C. J. Pearce, N. H. Oberliesa. Peptaibols from Two Unidentified Fungi of the Order Hypocreales with Cytotoxic, Antibiotic, and Anthelmintic Activities. J Pept Sci. 18 (2012) 500–510.

34. D. Ishiyama, T. Satou, H. Senda, T. Fujimaki, R. Honda, S. Kanazawa. Heptaibin, a novel antifungal peptaibol antibiotic from Emericellopsis sp. BAUA8289. J Antibiot (Tokyo). 53 (2000) 728-732.

35. B.-S. Yun, I.-D. Yoo, Y. H. Kim, Y.-S. Kim, S.-J. Lee, K.-S. Kim, W.-H. Yeo. Peptaivirins A and B, two new antiviral peptaibols against TMV infection. Tetrahedron Letters 41 (2000) 1429-1431.

36. T. V. Ovchinnikova, N. G. Levitskaya, O. G. Voskresenskaya, Z. A. Yakimenko, A. A. Tagaev, A. Y. Ovchinnikova, A. N. Murashev, A. A. Kamenskii. Neuroleptic Properties of the Ion-Channel-Forming Peptaibol Zervamicin: Locomotor Activity and Behavioral Effects. Chemistry & Biodiversity 4 (2007) 1374-1387.

37. R. Hermosa, A. Viterbo, I. Chet, E. Monte. Plant-beneficial effects of Trichoderma and of its Genes. Microbiology 158 (2012) 17–25.

38. D. S. Cafiso. Alamethicin: A Peptide Model for Voltage Gating and Protein-Membrane Interactions. Annual Review of Biophysics and Biomolecular Structure 23 (1994) 141-165.

39. D. R. Martin, R. J. P. Williams. Chemical Nature and Sequence of Alamethicin. Biochem. J. 153 (1976) 181-190.

40. R. Mahalakshmi, P. Balaram. Non-protein amino acids in the design of secondary s tructure scaffolds. Methods Mol Biol. 340 (2006) 71-94.

41. R. O. Fox Jr, F. M. Richards. A voltage-gated ion channel model inferred from the crystal structure of alamethicin at 1.5-Å resolution. Nature 300 (1982) 325 – 330.

42. J. Bürck, S. Roth, P. Wadhwani, S. Afonin, N. Kanithasen, E. Strandberg, A. S. Ulrich. Conformation and Membrane Orientation of Amphiphilic Helical Peptides by Oriented Circular Dichroism. Biophys J. 95 (2008) 3872–3881.

43. U. P. Fringeli, M. Fringeli. Pore formation in lipid membranes by alamethicin. Proc. Natl. Acad. Sci. USA 76 (1979) 3852-3856.

44. M. Lucaciu, S. Rebuffat, C. Goulard, H. Duclohier, G. Molle, B. Bodo. Interaction of the 14-residue peptaibols, harzianins HC, with lipid bilayers: permeability modifications and conductance properties. Biochim Biophys Acta. 1323 (1997) 85-96.

45. S. Agarwalla, I. R. Mellor, M. S. Sansom, I. L. Karle, J. L. Flippen-Anderson, K. Uma, K. Krishna, M. Sukumar, P. Balaram. Zervamicins, a structurally characterised peptide model for membrane ion channels. Biochem Biophys Res Commun. 186 (1992) 8-15.

46. C. Toniolo, M. Crisma, F. Formaggio, C. Peggion, R.F. Epand, R.M. Epand. Lipopeptaibols, a novel family of membrane active, antimicrobial peptides. Cellular and Molecular Life Sciences CMLS 58 (2001) 1179-1188.

47. M. De Zotti, B. Biondi, F. Formaggio, C. Toniolo, L. Stella, Y. Park, K.-S. Hahmd. Trichogin GA IV: an antibacterial and protease-resistant peptide. J. Pept. Sci. 15 (2009) 615–619.

48. B. Mojsoska, H. Jenssen. Peptides and Peptidomimetics for Antimicrobial Drug Design. Pharmaceuticals (Basel). 8 (2015) 366–415.

49. A. Rapisarda, N. Giamblanco, G.Marletta. Kinetic discrimination of DNA single-base mutations by localized surface plasmon resonance. Journal of Colloid and Interface Science 487 (2017) 141–148.

50. J. A. Jackman, V. P. Zhdanov, N.-J. Cho. Nanoplasmonic Biosensing for Soft Matter Adsorption: Kinetics of Lipid Vesicle Attachment and Shape Deformation. Langmuir 30 (2014) 9494−950.

51. Jonsson, M. P; Jönsson, P; Höök, F. Simultaneous Nanoplasmonic and Quartz Crystal Microbalance Sensing: Analysis of Biomolecular Conformational Changes and Quantification of the Bound Molecular Mass. Anal. Chem. 80 (2008) 7988–7995.

52. J. Benesch , A. Askendal, P. Tengvall. Quantification of adsorbed human serum albumin at solid interfaces: a comparison between radioimmunoassay (RIA) and simple null ellipsometry. Colloids and Surfaces B: Biointerfaces 18 (2000) 71–81.

CONCLUSIONS

The research developed in this PhD dissertation shows the versatility and efficiency of the use of localized surface plasmon resonance (LSPR) spectroscopy to investigate the interaction of relevant classes of biomolecules, e.g. peptides, proteins, lipids and DNA strands, at solid-liquid interfaces, with an emphasis on deciphering kinetics and pathways of dynamic adsorption processes.

The main advantages of the LSPR technique consists of an extremely short penetration depth of the evanescent wave propagating about 5−30 nm into the dielectric medium surrounding the metal nanoparticles. Consequently, the sensitivity of the plasmon frequency to refractive index changes ranges over a length scale comparable to the dimensions of most of relevant biomacromolecules, offering a better resolution in the detection of these analytes at interface skipping interfering effects from the bulk of solution.

Nevertheless LSPR spectroscopy can address questions such as specificity of an interaction, kinetics, affinity, and concentrations of selected molecules present in a sample of interest, up to now most publications in the field concern with lipid vesicles adsorption kinetics.

The results displayed and analyzed in the previous chapters, which are summarized and highlighted in the following conclusions, expanded our comprehension of relevant aspects for the biointerfaces science that could pave the way towards the interpretation of the complexity of the biomolecular adsorption phenomena.

- Kinetics study of competitive protein adsorption at hydrophobic and hydrophilic surfaces

The study of the adsorption kinetics of single and binary solution of Fibronectin and Albumin proteins onto hydrophilic and hydrophobic silicon oxide surfaces reveals non Vroman behavior at short adsorption time (i.e. 1 hour) with heavier Fibronectin adsorbing faster and in larger amount than lighter Albumin on both surfaces. It is suggested that in the peculiar experimental conditions we used, i.e., pH 7.4 and relatively high ionic strength (NaCl 0.1M), the adsorption process is driven by electrostatic forces disfavoring the adsorption of the smaller proteins having a radius of gyration comparable to the Debye screening length, i.e., increasing the efficiency of the repulsive forces with surfaces of the same charge. Moreover, our results shows that the dynamics of competitive protein adsorption can be envisioned from the diffusion coefficients and the affinity constants obtained for single protein adsorption. This finding suggests that the binary proteins solution behaves ideal without protein-protein interactions leading to interfering effect such as clustering or association.

- Kinetic discrimination of DNA single-base mutations by localized surface plasmon resonance

The effect of point mutation on the hybridization rate for ssDNA target solution interacting with surface anchored ssDNA probes was investigated in both competitive (mixture of targets) and non-competitive (pure target) conditions. It has been found that the presence of a single base mismatch in a 93-mer sequence is enough for observing significant difference in both hybridization rate and affinity, as demonstrated by the lower limit of detection determined for the complementary DNA strand with respect to the mutated one. Moreover, it has been shown that the mismatch sequences play a clear inhibition role on the hybridization rate of perfect match strand from a binary mixture of targets. This enables to develop a method for revealing and quantifying the mismatch target in a mixed sample with perfect match measuring the decrease in the overall hybridization rate.

- Influence of pH on the kinetics of phospholipid vesicles adsorption studied by LSPR technique

The study of the dynamics for POPC vesicles adsorption on silicon oxide surfaces shown that the formation of the supported lipid bilayer is strongly affected by buffer pH. In particular, below physiologic pH, vesicle adsorption has been accounted by a single-exponential function. This finding according to the literature indicates that the incoming vesicles rupture upon contact with a surface before a critical surface coverage is reached. Moreover, no significant variation in the adsorption rate is measured over the investigated range of pH (3- 6), suggesting that the vesicles-surface interaction is driven by Van der Waals and steric forces. On the contrary, above the physiological pH, vesicles adsorption follows a two-step mechanism, in which the first step is slow, corresponding to the adhesion of intact vesicles with surface, and the second one is fast, consisting to the vesicle rupture following by the fusion of the bilayer patches. Furthermore, it is observed that the rate of first step is linearly dependent on the pH over the range (7.4-10). Since POPC vesicles are zwitterionic over the investigated pH range, the observed effect may be due to the increased negative charge of surface, indicating the process is modulated by electrostatic vesicle-surface repulsion.

- Preliminary experiments on pH-induced reversible stretching-contracting modes in stimuli-responsive peptabiotics.

Preliminary study on the pH-responsive behavior of Trichogin GA IV analogs bearing lysine groups reveals that these system are able of rapid and reversible switching between extend and collapsed conformations. The proposed mechanism for the pH-response was that the peptide assumes an extended conformation to minimize the electrostatic repulsion forces that arise upon protonation of lysine group at low pH. Moreover, it has been found that the swelling factor determined for the L20 peptide, i.e. Trichogin dimer, is almost twice with respect to that for the Lipo-Lys peptide, i.e. Trichogin monomer. This finding suggested the possibility to modulate the swelling factor controlling the degree of polymerization of the polypeptide. However, in order to verify the results of this

preliminary study further experiments are in progress in our lab. In this respect, the planned analysis of novel Trichogin GA IV analogs with an higher degree of polymerization will make possible to improve our knowledge of the phenomenon and validate some of the hypothesis formulated.

APPENDIX 1.

COMPLEMENTARY EXPERIMENTAL TECHNIQUES

A.1 Quartz Crystal Microbalance with dissipation monitoring (QCM-D)

A.1.1 Fundamental principles of the QCM-D technique

QCM-D is a well-established technique for the simultaneous monitoring of mass load (in ng/cm^2 range) and energy dissipation obtained from change in the resonant frequency and the damping of a vibrating sensor [1].

The QCM-D setup consists of a thin AT-cut piezoelectric quartz crystal sandwiched between two gold electrodes evaporated on its two faces [2]. When an AC-voltage is applied over the electrodes, the crystal can be made to oscillate in a shear mode, i.e. perpendicular to the applied electric field [3]. Resonance will occurs when the thickness of the plate (t_q) is an odd integer (n) of half-wavelength of the induced wave according to the following equation [4]

$$t_q = n\frac{\lambda}{2} \qquad Eq.\,59$$

The resonant frequency, f, is then given by:

$$f = n\frac{v_q}{2t_q} = nf_0 \qquad Eq.\,60$$

where v_q is the wave velocity in the quartz plate [5].

Resonance is also observed at so-called overtones of the fundamental resonant frequency, which respond to changes in mass in a manner similar to the fundamental frequency. Only odd-numbered overtones can be produced, yielding overtone resonances at, e.g., 15, 25, 35, … MHz for a 5 MHz crystal [6].

The width of the crystal resonance is very narrow, which gives an extremely well-defined resonant frequency and the ability to measure changes in the resonant frequency very precisely [7]. Since the resonant frequency is determined by the total oscillating mass, which also includes all mass that is coupled to the surface, it can be used to measure the mass adsorbed on the surface in real time without need for any labels [8].

An increase in mass (Δm) bound to the quartz surface causes the crystal oscillation frequency to decrease, obtaining a negative shift in the resonance frequency (-Δf) [9]. A good approximation for the mass adsorbed to the sensor surfaces is the Sauerbrey relation [10]:

$$\Delta m = -k\Delta f \qquad Eq.61$$

where k is the mass sensitivity of the crystal (~18 ng/(Hz ×cm^2 for a typically used 4.95 MHz crystal [11]).

The Sauerbrey relation concludes that the change in resonance frequency is proportional to the change in the adsorbed mass. It holds if the adsorbed layer is rigid, if the added mass is small compared to the weight of the crystal, if there is no slip in the metal/layer interface, and if the layer is homogeneously distributed on the surface [12].
An acoustic sensor operated in liquid will lose the mechanical energy stored in the oscillation at a much higher rate than when operated in gas or vacuum, since molecules in the liquid environment move with the oscillating surface [13]. The magnitude of these losses depends on the density and viscosity of the liquid [13]. The extinction depth of the shear wave is given by [14]

$$\delta = \sqrt{\frac{\eta}{n\pi f\rho}} \qquad Eq.62$$

where η is the viscosity and ρ the density of the medium.
For a 4.95 MHz crystal in water this yields δ ~ 250 nm for the fundamental resonance frequency [15], and as can be seen form equation 31 the extinction depth will decrease approximately as the inverse square root of the overtone number, n. (see Figure 41).

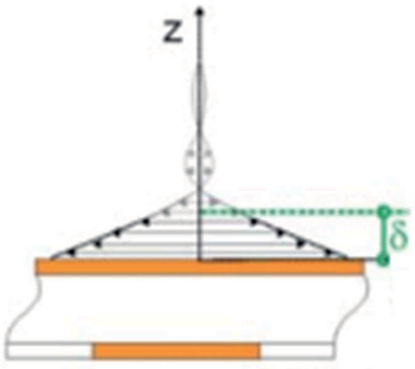

Figure 41. QCM shear wave penetration depth [16].

However, when the adsorbed film is hydrated (and or soft) the Sauerbrey equation is less accurate and underestimates the deposited hydrated mass per unit area [17]. As a soft film (viscoelastic) does not completely couple to the oscillation of the quartz crystal and will show a damping or dissipation effect [17]. Monitoring dissipation enables qualitative analysis of the structural properties of adsorbed molecular layers [18] (see next paragraph for further details).
Dissipation (D) is defined by [19]

$$D = \frac{E_{lost}}{2\pi E_{stored}} \qquad Eq.63$$

where E_{lost} is the energy lost (dissipated) during one oscillation cycle and E_{stored} is the total energy stored in the oscillator.
The technique to measure the dissipation factor is based on the fact that when the driving power to a piezoelectric crystal oscillator is switched off, the voltage over the crystal, A(t), decays as an exponentially damped sinusoidal with time, t [19]

$$A(t) = A_0 e^{\frac{t}{\tau}} \sin(2\pi f t + \varphi) \qquad Eq.64$$

where A_0 is the amplitude of oscillation before switching off the driving power, t is the decay time constant, f the frequency and f is the phase angle. The decay time constant is related to the dissipation factor [19]:

$$D = \frac{1}{\pi f \tau} \qquad Eq.65$$

A.1.2 QCM-D data analysis

For a typical biomolecules adsorption experiment, QCM-D data vs. time will shows that the adsorption causes an initial rapid frequency decrease (mass increase) followed by a slower frequency decrease as the surface coverage saturates [9]. The D-shifts are positive and display kinetics similar (but not identical) to the f-shifts (Figure 42) [20]. The frequency (Δf) and dissipation shift (ΔD) plotted are calculated as the difference between the value at each instant of time and the initial value f_0, D_0 acquired when the crystal is surrounding of aqueous solution that contains no adsorbent molecules [21]. Therefore, the data plotted shows only the changes due to the presence of adsorbed molecules on the surface and does not consider shift in frequency and dissipation induced by the fluid surrounding the crystal, such as liquid trapped in cavities or porous of the surface, that increase the mass value, and the loss of energy induced by the liquid during the oscillation of the crystal [22].

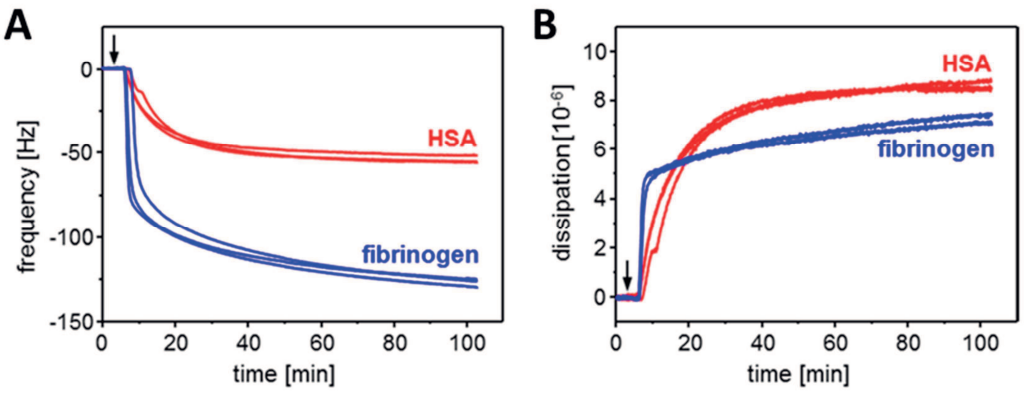

Figure 42. Frequency and dissipation shift for human serum albumin (HSA) (red curves) and fibrinogen (blue curves) proteins adsorption. Samples contained 250 µg/mL protein in PBS.[23]

An important consideration is that the device measure a response proportional to the total mass added on the sensor surface [24]. The total mass is in most cases not proportional to the actual number of adsorbed molecules, since biomolecules are in aqueous solution, it is possible to have a significantly increase in weight due to the bond water and, moreover, water trapped between the adsorbed molecules may be sensed as an additional mass [25]. This obscures the true mass adsorption kinetics even for simple adsorption processes, but can, when properly understood and addressed with complementary measurements, lead to greater understanding of the adsorption process and the properties of adsorbed thin films [26]. Furthermore, the amount of water influences the viscoelasticity of the adlayer and consequently the dissipation; in particular a high quantity of water induces a higher loss of energy [27].

Generally, since Δf and ΔD show different time dependencies, a useful and revealing way of exploring Δf -ΔD relationship is to plot ΔD vs. Δf (called the D-f plots) [28] as shown in Figure 43, where time is eliminated as an explicit parameter. This plot is useful to evaluate the structural properties of the adlayer because it relates how much dissipation is caused per unit of frequency change (mass) [29]. Changes via slope suggest structural alterations within the adsorbed layer as the adsorption proceeds [29]. In other words, this plots gives an estimate of how new mass added affects the structure on the surface: the higher the ΔD/Δf slope, the higher the dissipation per unit added mass, signaling an increasing water content in the protein film forming a less rigid protein layer.

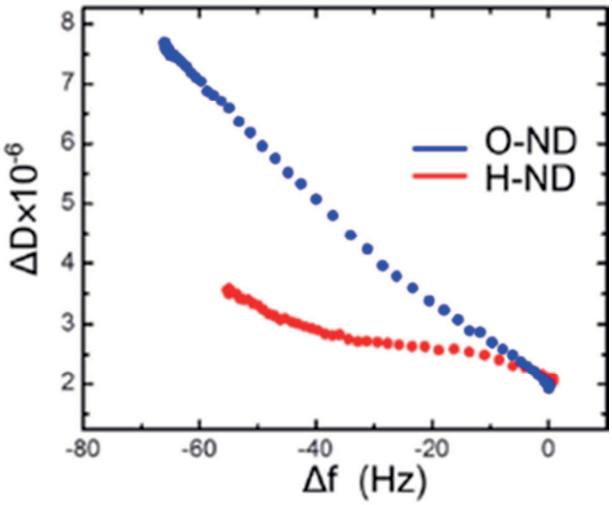

Figure 43. Dissipation vs. frequency plot for bovine serum albumin (BSA) adsorption on positively (hydrogen-terminated) and negatively (oxygen-terminated) charged diamond surfaces [30].

A.2 Attenuated total reflection (ATR) Fourier transform infrared (FTIR) spectroscopy

A.2.1 Fundamental principles of ATR-FT-IR

Infrared Spectrum (IR) is mainly used to study molecular structure and composition in substances and thus is also called molecular spectrum [31]. When the sample is exposed to infrared light with continuously changing frequency, the molecule absorbs irradiation of certain frequencies and is subject to vibration or rotation, thus to cause the change of dipole moment. The molecule's transition from normal state to excited state weakens the intensity of the corresponding transmitted light in the absorption region, generating absorption IR spectra [32].

Surface IR spectroscopy was widely used for biosensors, first, to monitor the preparation of biosensors starting by the very preliminary surface functionalization step, often the formation of self-assembled monolayers (SAMs), and second, to investigate the attachment of biomolecules or receptors to the surfaces, and finally, as a transduction technique for biorecognition and binding events [33].

Various IR spectroscopy modes of operation are used for biosensors, including the simplest transmission mode [34]. Yet, for the sensitive detection of adsorbed small molecules, the use of surface-enhancement mechanisms is mandatory [33]. Among these modes, the most commonly used is: Attenuated Total Reflection InfraRed (ATR-IR) Spectroscopy [35].

The ATR-IR uses the phenomenon of a complete reflection during the transition of IR radiation from an optically denser medium (prism) to thinner medium (sample) [35]. A sample is placed on the IR-transparent prism surface with a refractive index being always higher than that of the sample (Figure 44) [36].

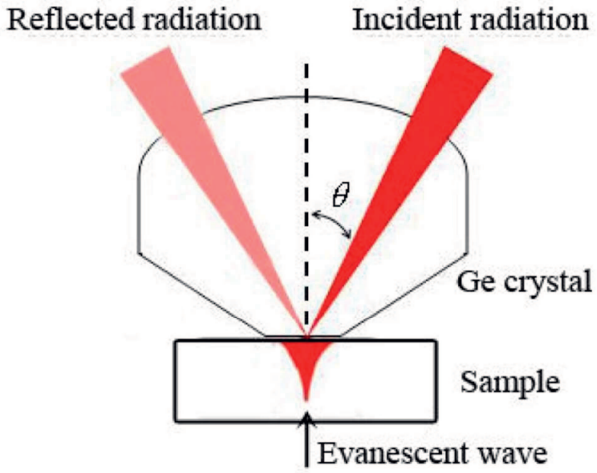

Figure 44. Graphical Representation of ATR phenomenon [36].

The radiation beam is directed by one of the prism wall to the prism-sample interface at angle θ higher than the limiting. Under these conditions, a complete reflection occurs at the internal prism side and the beam reflected comes out through the second prism wall, where the beam intensity and absorption spectrum are recorded. During the total internal reflection in the optically thinner medium (sample) is formed an electromagnetic wave, so-called evanescent wave that fulfills the condition of the continuity of electromagnetic field vectors at the interface of media with various wave refractive indices, n_1 and n_2 [36]. The evanescent wave penetration depth (d_p) in sample depends on the IR radiation wavelength (λ), incident angle, (θ), prism refractive index, (n_1), and sample refractive index in relation to the prism ($n_{2,1}$) and is expressed by the following equation [37]

$$d_p = \frac{\lambda}{\left(2\pi n_1 \left[\sin^2\theta - n_{21}{}^2\right]^{\frac{1}{2}}\right)} \qquad Eq.66$$

Along the path of IR evanescent wave the sample selectively absorbs energy to decrease the intensity of radiation. The weakened wave returns to the prism and then to an IR detector. There the system generates an FTIR-ATR absorption spectrum characteristic of the given sample. The FTIR-ATR absorption spectrum slightly differs from that obtained by the transmission method. The differences concern the intensity and frequency of absorption peaks characteristic of chemical groups in view of the phenomenon of reflection, e.g. Goos Hänchen's displacement [38]. Thus it is necessary to take corrective action that can be realized automatically [39].

The penetration depth of IR beam can be controlled within some range by selecting an appropriate prism (selection of the refractive index) and the incident angle of beam [40]. The commonly used prisms are made of diamond, germanium, silicon and ZnSe, whose refractive indices are equal to 2.4, 4.0, 3.4 and 2.4, respectively, and the beam penetration depths: 2.03 µm, 0.67 µm, 0.84 µm and 2.03 µm, respectively, at ν = 1000 cm^{-1} [41].
During testing sub-micrometric coating, the beam penetrates a higher depth than the coating depth and also passes to the substrate, on which the coating is deposited. The absorption spectrum then constitutes a superposition of the spectrum of coating material and substrate. In such cases, qualitative analysis is carried out, which takes into account the absorption spectrum of substrate [42].

A.2.2 ATR-FTIR information

ATR-FT-IR spectroscopy enables the chemical identification of surface adsorbed species by the assignment of their diagnostic IR bands [31]. Indeed, wave number position, number of wave peaks of infrared absorption band and the intensity of absorption band indicate the characteristics of the molecular structure, and thus can be used to identify the structural composure of the unknown objects or its chemical groups [32].
Moreover, infrared absorbance measurements performed in ATR-FTIR mode can be used to determine the thickness of thin film adsorbed adjacent to the ATR crystal according to the following method [43].
For the individual functional group in the depth direction, the relationship of its concentration profile *C(z)* and ATR absorbance *A*, can be written as [44]

$$A = \frac{n_{21} E_0^2 \varepsilon}{\cos\theta} \int_0^\infty C(z) e^{\left(-\frac{2z}{d_p}\right)} dz \qquad Eq.\,67$$

where A is the integrated absorbance, ε is the integrated molar absorptivity (measured by transmission experiments and using Beer's law), *z* is the distance from the IRE surface (cm) and *C(z)* is the concentration as a function of distance from the IRE (mol l^{-1}).
In order to resolve C(x) it is necessary to assume a specific function form of C(x). According to the literature [45], it is convenient to use a step functions as C(x) for modeling the concentration profiles of the adlayer as shown below

$$C(x) = \begin{cases} Mx & when\ x \le d_0 \\ N(x - d_0) & when\ x > d_0 \end{cases} \qquad Eq.\,68$$

where *x* is the distance from the outmost surface in the depth direction, d_0 is defined as the thickness of even polymer coating; *M*, *N* is constant, which is independent of *x*.

Adding Eq. 68 to Eq. 67, we obtain,

$$A=\frac{n_{21}E_0^2\varepsilon}{\cos\theta}\left(\frac{Md_p}{2}-Md_0e^{-\frac{2d_0}{d_p}}-Me^{-\frac{2d_0}{d_p}}\frac{d_p}{2}-d_0Ne^{-\frac{2d_0}{d_p}}+N\frac{d_p}{2}\right) \qquad Eq.69$$

Equation 69 is a multiparameter function, which brings some difficulty in calculating and measurement. Therefore, to obtain a resolvable equation associated with feasible measurement, two assumptions are proposed as follows:

Assumption 1: being relative to d_p, d_0 is so low that it could be ignored when calculating d_p/d_0; that is $d_p/d_0 \approx 1$, $e^{-\frac{2d_p}{d_0}} \approx 1$; as a result, Eq. 70 is derived from Eq. 69 [46]

$$A=\frac{n_{21}E_0^2\varepsilon}{\cos\theta}\left[N\frac{d_p}{2}-(M+N)d_0\right] \qquad Eq.70$$

Assumption 2: the coating is completely transparent to the frequency selected for the analysis, that is, no absorption and therefore M =0. This assumption could be satisfied experimentally, by using a special group that is only contained in the bulk substrate. This group and one of its characteristic frequencies are named by us as the reference group (RG) and the reference frequency (RF), respectively. Ideally, RF should not be overlapped by any part of the absorption frequencies of the coating. As a result, Eq. 70 could be simplified as Eq. 71 [46]

$$A=\frac{n_{21}E_0^2\varepsilon}{\cos\theta}\frac{N(d_p-2d_0)}{2} \qquad Eq.71$$

For a blank substrate, d_0=0, the adsorption area of RG near RF is named as A_0

$$A_0=\frac{n_{21}E_0^2\varepsilon}{\cos\theta}N\frac{d_p}{2} \qquad Eq.72$$

Dividing Eq. 71 by Eq.72, we obtain Eq. 73

$$\frac{A}{A_0}=1-\frac{2}{d_p}d_0 \qquad Eq.73$$

In this equation, d_0 is a constant, and d_p could be calculated through Eq. 66 under a given frequency and incidence angle, while A and A_0 are obtained respectively from the spectra at every incidence angle. When we define $2/d_p$ as x, and A/A_0 as y, a theoretical linear equation could be obtained as

$y = 1 - xd_0$, where the slope is d_0. Therefore, for a sample, through changing the incidence angle, a series of A/A_0, associated with d_p could be obtained, and if Eq. 73 is tenable, a linear correlation should be presented after plotting A/A_0 versus $2/d_p$. Thus, d_0 as the slope of the line could be obtained [47].

The principal benefit of ATR sampling comes from the very thin sampling pathlength and depth of penetration of the IR beam into the sample [48]. The drawback of ATR technique is a relatively low sensitivity and susceptibility to the effect of environmental conditions, which makes it necessary to calibrate the IR spectrum [39].

A.3 Atomic Force Microscopy (AFM)

A.3.1 Basic principles of AFM

The AFM is a conceptually simple apparatus [49]. A sharp probing tip is attached to situated at the apex of a flexible cantilever-type spring that is often a diving board or V-shaped, usually made of silicon. The AFM utilizes a piezoelectric scanner that moves the sample in 3 dimensions by a sub-nanometer amount when a voltage is applied (Figure 45). To form an image, the tip is brought close to the sample and raster-scanned over the surface, causing the cantilever to be deflected due to probe-sample interactions. A line-by-line image of the sample is taken by scanning digitizing the deflection of the lever or the z-movement of the scanner as a function of the lateral position x, y, which is itself detected using laser light reflected off the back surface of the cantilever onto a position-sensitive photodiode detector [50].

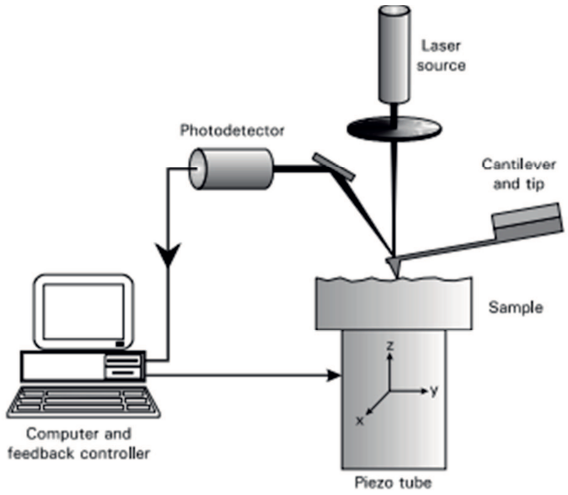

Figure 45. Schematic representation of the main components of an atomic force microscope (AFM) [50].

Typical spring constants are between 0.001 to 100 N/m and motions from microns to ≈ 0.1 Å are measured by the deflection sensor [51]. Typical forces between probing tip and sample range from 10^{-11} to 10^{-6} N [52]. Therefore, non-destructive imaging is possible with these small forces. Two force

regimes are distinguished: Contact and non-contact mode. When the microscope is operated in non-contact mode at tip-sample separations of 10 to 100 nm, forces, such as van der Waals, electrostatic, magnetic or capillary forces, can be sensed and give information about surface topography, distributions of charges, magnetic domain wall structure or liquid film distribution [53]. At smaller separations of the order of A the probing tip is in contact with the sample. In this mode, ionic repulsion forces allow the surface topography to be traced with high resolution [53]. Under best conditions atomic resolution is achieved. In addition, frictional forces and elastic or plastic deformations can be detected under appropriate conditions [54].

A.3.2 Modes of operation

Among the different ways to operate with AFM the results presented in this thesis have been measured in contact, also called dc-modes, and tapping mode, also called ac-modes [55]. In the static mode, the cantilever-type spring bends in response to the force F which acts on the probing tip until the static equilibrium is established. As derived from Hooke's law, the deflection z_t of a cantilever is proportional to the force $F = c_B z_t$ where the proportional constant is the spring constant c_B. A beam with constant cross section has a spring constant which is given by [56]

$$c_B = \frac{3EI}{l^3} \qquad Eq.\,74$$

where *E* is the Young's modulus, *l* the length and *I* the moment of inertia. For a rectangular beam of width *b* and thickness *d* the moment of inertia *I* is given by [57]

$$I = \frac{bd^3}{12} \qquad Eq.\,75$$

With the dimensions l x 10 x 100 µm^2 of a rectangular Si-cantilever (E=1.69.10^{-11}N/m^2) a spring constant of c_B = 0.42 N/ m is derived. In the static, mode typical forces between 10^{-10} to 10^{-6} N are measured [52].

While scanning the surface, variation of the deflection are measured by laser beam shift and feed beck to scanner, whose readjust height of the sample relative to the probing tip to keep deflection constant. Consequently, the force applied on the sample held constant. This mode is called equiforce mode, is the most common mode [58].

In the dynamic mode the lever is oscillating close to its resonance frequency. A distance-dependence force (F_z) shifts the resonance curves. The equation of motion of the rectangular beam is given by [57]

$$\frac{\partial \Psi^4}{\partial x^4} + \frac{\mu}{EI}\frac{\partial \Psi^2}{\partial x^2} = F(x,z) \qquad Eq.\,76$$

where $\mu = \frac{m}{l}$ is the mass density. With the Ansatz $\Psi = Y(x)T(t)$ the differential equation can be separated. The time dependent part is described by a harmonic equation $T + \omega^2 T = 0$. The nth Eigenfrequency is given by [59]

$$f_n = \frac{(\kappa_n l)^2}{2\pi l^2}\sqrt{\frac{EI}{\mu}} = \frac{(\kappa_n l)^2}{2\sqrt{3}\pi}\sqrt{\frac{c_B}{m}} \qquad Eq.\,77$$

where $f_n = 2\pi\omega$, and κ_n, depends on the space dependent part and therefore also depends on the force acting on the tip.

In first approximation only the force gradient $F' = \frac{\partial F}{\partial z}$ influences the resonance frequency. An effective spring constant is defined by [54]

$$c_{eff} = c_B - F' \qquad Eq.\,78$$

A repulsive force (F' < 0) stabilizes the spring and increases the resonance frequency, whereas an attractive force destabilizes the spring and lowers the resonance frequency [60]

$$f_1 \approx 0.32\sqrt{\frac{c_{eff}}{m}} = 0.32\sqrt{\frac{c_B - F'}{m}} \qquad Eq.\,79$$

In the ac-mode the feedback loop either asserts constant amplitude (slope detection) or keeps the frequency constant (FM-detection) [57]. Both methods have the same physical content: The resonance curve is fixed to a certain position during the whole scan and profiles of constant gradient are measured. In the ac-mode, force gradients between 10^{-5} and 10^{1} N/m are measured. With a simple force law of the form $F(z) = const \times z^{-n}$ the corresponding forces at a distance of z = 10 nm range is between l0^{-13} to 10^{-7} N [52].

A.3.3 Information obtained from AFM

Since AFM has been develop in the late eighties, it has been used as high resolution imaging (nanoscale range), on a variety of substrate and biomolecules including metals, polymers, protein or even cells [61]. More specifically, in study of adsorption process, force microscopy allows to correlate the average (i.e. macroscopic) film properties measured by using mean-field biosensor techniques, e.g. LSPR or QCM-D, to molecular states of the film [62]. However, this technique, has a low time-resolution, are technically demanding and time-consuming risk influencing the sample by the interaction with the AFM tip and are limited in probing areas for which statistics are low and fluctuations could become important [63].

A.4 References

1. M. Rodahl, F. Höök, C. Fredriksson, C. A. Keller, A. Krozer, P. Brzezinski, M. Voinova, B. Kasemo. Simultaneous frequency and dissipation factor QCM measurements of biomolecular adsorption and cell adhesion. Faraday Discuss. 107 (1997) 229-246.
2. J. Wang, M. D. Ward, R.C. Ebersole, R. P. Foss. Piezoelectric pH Sensors: AT-Cut Quartz Resonators with Amphoteric Polymer Films. Anal. Chem. 65 (1993) 2553-2562.
3. G. Liu, G. Zhang. "Basic Principles of QCM-D." Qcm-d Studies on Polymer Behavior at Interfaces. Heidelberg: Springer Verlag, 2013.
4. F. Höök. Development of a novel QCM technique for protein adsorption studies. Chalmers University of Technology and Göteborg University, Sweden; 1997. Thesis.
5. Z. Lin, M. D. Ward. The Role of Longitudinal Waves in Quartz Crystal Microbalance Applications in Liquids. Anal. Chem. 67 (1995) 685-693.
6. T. P. McNamara, C. F. Blanford. A sensitivity metric and software to guide the analysis of soft films measured by a quartz crystal microbalance. Analyst 141 (2016) 2911-2919.
7. V. E. Bottom. Introduction to Quartz Crystal Unit Design, Van Nostrand Reinhold Company, 1982.
8. Ö. Ertekin, S. Öztürk, Z. Z. Öztürk. Label Free QCM Immunobiosensor for AFB1 Detection Using Monoclonal IgA Antibody as Recognition Element. Sensors 16 (2016) 1274.
9. R. Heeb, R. M. Bielecki, S. Lee, N. D. Spencer. Room-Temperature, Aqueous-Phase Fabrication of Poly(methacrylic acid) Brushes by UV-LED-Induced, Controlled Radical Polymerization with High Selectivity for Surface-Bound Species. Macromolecules 42 (2009) 9124–9132.
10. B. D. Vogt, E. K. Lin, W. Wu, C. C. White. Effect of Film Thickness on the Validity of the Sauerbrey Equation for Hydrated Polyelectrolyte Films. J. Phys. Chem. B 108 (2004) 12685-12690.
11. Z. Zhao, X. Ji, R. Dimova, R. Lipowsky, Y. Liu. Viscoelasticity of Poly(ethylene glycol) Solutions on Supported Lipid Bilayers via Quartz Crystal Microbalance with Dissipation. Macromolecules 48 (2015) 1824−1831.
12. D.Buttry, “Applications of the QCM to Electrochemistry”, in A Series of Advances in Electroanalytical Chemistry, edited by Allen Bard, Marcel Dekker, 1991, p. 23-33.
13. M. V. Voinova. On Mass Loading and Dissipation Measured with Acoustic Wave Sensors: A Review. Journal of Sensors 2009 (2009) Article ID 943125, 13 pages.
14. G. Ohlsson, P. Axelsson, J. Henry, S. Petronis, S. Svedhem, B. Kasemo. A miniaturized flow reaction chamber for use in combination with QCM-D sensing. Microfluid Nanofluid 9 (2010) 705–716.
15. I. Reviakine, D. Johannsmann, R. P. Richter. Hearing What You Cannot See and Visualizing What You Hear: Interpreting Quartz Crystal Microbalance Data from Solvated Interfaces. Anal. Chem. 83 (2011) 8838–8848.

16. K. A. Melzak, S. Moreno-Flores, A. E. Lopez, J. L. Toca-Herrera. Why size and speed matter: frequency dependence and the mechanical properties of biomolecules. Soft Matter7 (2011) 332–342
17. R. Lucklum, C. Behling, P. Hauptmann. Role of Mass Accumulation and Viscoelastic Film Properties for the Response of Acoustic-Wave-Based Chemical Sensors. Anal. Chem. 71 (1999) 2488-2496.
18. E. Reimhult, C. Larsson, B. Kasemo, F. Höök. Simultaneous Surface Plasmon Resonance and Quartz Crystal Microbalance with Dissipation Monitoring Measurements of Biomolecular Adsorption Events Involving Structural Transformations and Variations in Coupled Water. Anal. Chem. 76 (2004) 7211-7220.
19. M. C. Dixon. Quartz Crystal Microbalance with Dissipation Monitoring: Enabling Real-Time Characterization of Biological Materials and Their Interactions. Journal of Biomolecular Techniques 19 (2008) 151–158.
20. F. Höök, M. Rodahl, B. Kasemo, P. Brzezinsk. Structural changes in hemoglobin during adsorption to solid surfaces: Effects of pH, ionic strength, and ligand binding. Proc. Natl. Acad. Sci. USA 95 (1998) 12271–12276.
21. B. P. Binks. Modern Characterization Methods of Surfactant Systems. Marcel Dekker Inc. New York, NY (1999) 488-489.
22. M. Yang, M. Thompson, W. C. Duncan-Hewitt. Interfacial properties and the response of the thickness-shear-mode acoustic wave sensor in liquids. Langmuir 9 (1993) 802–811.
23. S. Hohmann, S. Kögel, Y. Brunner, B. Schmieg, C. Ewald, F. Kirschhöfer, G. Brenner-Weiß, K. Länge. Surface Acoustic Wave (SAW) Resonators for Monitoring Conditioning Film Formation.
24. J.L. Arlett, E.B. Myers, M. L. Roukes. Comparative advantages of mechanical biosensors. Nat Nanotechnol. 6 (2011) doi:10.1038/nnano.2011.44. Sensors 15 (2015) 11873-11888.
25. B. Schuster, U. B. Sleytr. Relevance of glycosylation of S-layer proteins for cell surface properties. Acta Biomaterialia 19 (2015) 149–157.
26. J. Vörös. The Density and Refractive Index of Adsorbing Protein Layers. Biophysical Journal 87 (2004) 553–561.
27. A. Kunze, F. Zhao, A. Marel, S. Svedhem, B. Kasemo. Ion-mediated changes of supported lipid bilayers and their coupling to the substrate. A case of bilayer slip? Soft Matter 7 (2011) 8582-8591.
28. N. Tymchenko, E. Nilebäck, M. V. Voinova, J. Gold, B. Kasemo, S. Svedhem. Reversible Changes in Cell Morphology due to Cytoskeletal Rearrangements Measured in Real-Time by QCM-D. Biointerphases 7 (2012) 43.
29. J. Song, W. E. Krause, O. J. Rojas. Adsorption of polyalkyl glycol ethers and triblock nonionic polymers on PET. Journal of Colloid and Interface Science 420 (2014) 174–181.
30. M. Aramesh, O. Shimoni, K. Ostrikov, S. Prawera, J. Cervenkaa. Surface charge effects in protein adsorption on nanodiamonds. Nanoscale 7 (2015) 5726-5736.

31. A. Barth. Infrared spectroscopy of proteins. Biochimica et Biophysica Acta 1767 (2007) 1073–1101.
32. D. Shikha, R. Awasthi. Application of I.R. Spectroscopy & Mass Spectrometry in Structural Elucidation of Drugs. International Journal of Advanced Research in Chemical Science 2 (2015) 38-45.
33. R. Aroca. Surface-Enhanced Infrared Spectroscopy. Surface Enhanced Vibrational Spectroscopy. Hoboken, NJ: Wiley, 2006.
34. W. Suëtaka, J. T. Yates. Surface Infrared and Raman Spectroscopy: Methods and Applications. New York: Plenum Press, 1995.
35. J. Schmitt, H. Flemming. FTIR-spectroscopy in microbial and material analysis. International Biodeterioration & Biodegradation 41 (1998) 1-11.
36. J. Yin, Y. Xia. Chemical visualization of individual chondrocytes in articular cartilage by attenuated-total-reflection Fourier Transform Infrared Microimaging. Biomedical Optics Express 2 (2011) 937-945.
37. T. Buffeteau, B. Desbat, D. Eyquem. Attenuated total reflection Fourier transform infrared microspectroscopy: Theory and application to polymer samples. Vibrational Spectroscopy l 1 (1996) 29-37.
38. K. K. Chittur. FTIR/ATR for protein adsorption to biomaterial surfaces. Biomaterials 19 (1998) 357—369.
39. J. Grdadolnik. Atr-Ftir Spectroscopy: Its Advantages and Limitations. Acta Chim. Slov. 2002, 49, 631−642.
40. V. Offermann, P. Grosse, M. Feuerbacher, G. Dittmar. Experimental aspects of attenuated total reflectance spectroscopy in the infrared. Vibrational Spectroscopy 8 (1995) 135-140.
41. A. R. Hind, S. K. Bhargava, A. McKinnon. At the solid-liquid interface: FTIR-ATR- the tool of choice. Advances in Colloid and Interface Science 93 (2001) 91 -114.
42. S. Belfer, R. Fainchtain, Y. Purinson, O. Kedem. Surface characterization by FTIR-ATR spectroscopy of polyethersulfone membranes-unmodified, modified and protein fouled. Journal of Membrane Science 172 (2000) 113–124.
43. S. R. Kane, P. D. Ashby, L. A. Pruitt. ATR-FTIR as a Thickness Measurement Technique for Hydrated Polymer-on-Polymer Coatings. Journal of Biomedical Materials Research Part B: Applied Biomaterials 91B (2009) 613-620.
44. K. Ohta, R. Iwamoto. Lower limit of the thickness of the measurable surface layer by Fourier transform infrared attenuated total reflection spectrometry. Anal. Chem. 57 (1985) 2491-2499.
45. D. J. Carlsson, D. M. Wiles. Surface studies by attenuated total reflection Spectroscopy. I. Corona treatment of polypropylene. Can. J. Chem. 48 (1970) 2397-2406.
46. P. Yang, X. Meng, Z. Zhang, B. Jing, J. Yuan, W. Yang. Thickness Measurement of Nanoscale Polymer Layer on Polymer Substrates by Attenuated Total Reflection Infrared Spectroscopy. Anal. Chem. 77 (2005) 1068-1074.

47. K. K. Chittur. FTIR/ATR for protein adsorption to biomaterial surfaces. Biomaterials 19 (1998) 357—369.
48. L. Barbeş, C. Rădulescu, C. Stihi. Atr-Ftir Spectrometry Characterisation of Polymeric Materials. Romanian Reports in Physics 66 (2014) 765–777.
49. A. A. G. Requicha, S. Meltzer, F. P. Terán Arce, J. H. Makaliwe, H. Sikén, S. Hsieh, D. Lewis, B. E. Koel, M. E. Thompson. Manipulation of Nanoscale Components with the AFM: Principles and Applications. IEEE international Conference on Nanotechnology, Maui (2001).
50. F. L. Leite, L. H. C. Mattoso, O. N. Oliveira Jr, P. S. P. Herrmann Jr. The atomic force spectroscopy as a tool to investigate surface forces: basic principles and applications. A. Méndez-Vila, J. Díaz. (Ed.). Modern research and education topics in microscopy. Badajoz: Formatex, 2007. p. 747-757.
51. Rogers, Ben, Jesse Adams, and Sumita Pennathur. Nanotechnology: Understanding Small Systems. Boca Raton: CRC Press, 2011. p.175-176.
52. A. Noy, D.V. Vezenov, C.M. Lieber. Chemical Force Microscopy. Annu. Rev. Mater. Sci. 27 (1997) 381–421.
53. N. A. Burnham, R. J. Colton, H. M. Pollock. Interpretation of force curves in force microscopy. Nanotechnology 4 (1993) 64-80.
54. H. Butt, B. Cappella, M. Kappl. Force measurements with the atomic force microscope: Technique, interpretation and applications. Surface Science Reports 59 (2005) 1–152.
55. L. Olsson, N. Lin, V. Yakimov, R. Erlandsson. A method for in situ characterization of tip shape in ac-mode atomic force microscopy using electrostatic interaction. Journal of Applied Physics 84 (1998) 4060-4064.
56. J. P. Cleveland, S. Manne, D. Bocek, P. K. Hansma. A nondestructive method for determining the spring constant of cantilevers for scanning force microscopy. Rev. Sci. Instrum. 64 (1993) 403-405.
57. E. Meyer. Atomic Force Microscopy. Progress in Surface Science 41 (1992) 3-49.
58. N. Venkataramani. Scanning Probe Method. A Tool to Characterize Materials. Proceedings of Solid State Physics Symposium 41 (1998) 79-82.
59. F.Elmer, M. Dreier. Eigenfrequencies of a rectangular atomic force microscope cantilever in a medium. J. Appl. Phys. 81 (1997) 7709.
60. L. Heim, M. Kappl, H.Butt. Tilt of Atomic Force Microscope Cantilevers: Effect on Spring Constant and Adhesion Measurements. Langmuir 20 (2004) 2760-2764.
61. R. Garcia, A. W. Knoll, E. Riedo. Advanced scanning probe lithography. Nature Nanotechnology 9 (2014) 577–587.
62. O. Svensson, J.Sotres, A. Barrantes. Investigating protein interactions at solid surfaces- in situ-non labeling techniques. J. M. Ruso, Á. Piñeiro (Ed.). Proteins in Solution and at Interfaces: Methods and Applications in Biotechnology and Materials Science. Hoboken, NJ: John Wiley & Sons, 2013.

63. P. Milhiet, C. Le Grimellec. Observing the Nanoscale Organization of Model Biological Membranes by Atomic Force Microscopy. Y. Dufrêne (Ed.). Life at the Nanoscale: Atomic Force Microscopy of Live Cells. Singapore: Pan Stanford Publishing, 2011, pp.14-17.

APPENDIX 2:

A. Rapisarda, N. Giamblanco, G. Marletta. Kinetic Discrimination of DNA single-base mutations by Localized Surface Plasmon Resonance. Journal of Colloid and Interface Science 487 (2017) 141-148.

Journal of Colloid and Interface Science 487 (2017) 141–148

Contents lists available at ScienceDirect

Journal of Colloid and Interface Science

journal homepage: www.elsevier.com/locate/jcis

Regular Article

Kinetic discrimination of DNA single-base mutations by localized surface plasmon resonance

Antonino Rapisarda, Nicoletta Giamblanco *, Giovanni Marletta

Laboratory for Molecular Surfaces and Nanotechnology (LAMSUN), Department of Chemical Science, University of Catania and CSGI, Italy

GRAPHICAL ABSTRACT

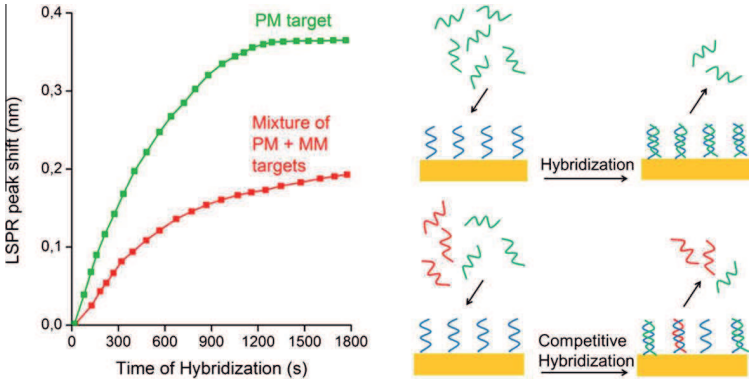

ARTICLE INFO

Article history:
Received 17 August 2016
Revised 12 October 2016
Accepted 13 October 2016
Available online 14 October 2016

Keywords:
Localized surface plasmon resonance
DNA hybridization kinetic
Single base mutation detection
KRAS

ABSTRACT

Clinical application of DNA microarrays used for screening of single nucleotide polymorphisms (SNPs) are very important for diagnosis of diseases and appropriate treatment of patients. In this paper localized surface plasmon resonance (LSPR) technique has been used to study the DNA hybridization process for binary solutions of respectively perfectly matching (PM) and single base mismatching (MM) 93-mer ssDNA from KRAS codon 12. 5′-thiol modified 35-mer ssDNA has been linked to the Au nanodisks array as probe with a surface coverage of $2.8 \pm 0.1 \times 10^{12}/cm^2$. Probe's binding properties was investigated in details, obtaining a sensitivity down to 10 nM and 13 nM, respectively for PM and MM, showing that the hybridization process occurs at a lower rate for MM with respect to PM target. The competitive hybridization is accounted for by an inhibition model, where the non-complementary sequences kinetically hinder the hybridization of the perfect matching sequences, owing to their above mentioned affinity constant differences for the same probe. Accordingly, the single nucleotide polymorphisms can therefore be revealed in a single step and label free mode with high sensitivity and specificity by LSPR measurements.

1. Introduction

Single base polymorphisms (SNPs) are the most abundant and common form of genetic variation [1] and are prevalent in clinical issues [2]. For instance, point mutation in the Kirsten Rat Sarcoma viral oncogene homologous (KRAS) gene codon 12, 13, and 61 are associated with the development of certain pancreatic and lung cancers [3] and their detection is critical for the selection of the appropriate type of treatment [4].

Until today the most used technologies designed to reveal SNPs are based on the principle of allele-specific hybridization, relying

* Corresponding author.
E-mail address: n.giamblanco@unict.it (N. Giamblanco).

http://dx.doi.org/10.1016/j.jcis.2016.10.026
0021-9797/

on the ability of oligonucleotide probes to bind selectively to DNA target sequences [5]. DNA microarrays via surface are based on oligonucleotide probes immobilized on the chip surface. Typically, the DNA chips require expensive fabrication processes [6,7]. However, the most notable limitations are associated with the employed detection method. Indeed, the highly sensitive nature of hybridization assays with single base discriminatory capabilities requires a comparably sensitive detection method to reveal the small changes in analytical signal produced by a single nucleotide mismatch, which produces difference of melting temperature (T_m), less than 3 °C [8]. DNA hybridization was conducted on sensing systems based on unnatural probes having lower binding affinity during hybridization resulting in a decline of T_m up to 15 °C and inducing a high sequence specificity [9]. The discrimination of one or more mismatches was generally accomplished by adjusting the hybridization conditions such as temperature, ionic strength, formamide concentration, or other dissociation conditions of the probe and target duplex [10]. Despite significant developments obtained by using various nanomaterials-based SNP assays coupled with a number of different readout strategies, the more important limitation for SNP analysis remains the quantification of extremely low abundance SNPs in an overwhelming background of wild-type genes in clinical settings [11].

Moreover, numerous statistical models have been created to evaluate the hybridization of nucleic acid targets using end-point analysis [12]. Additionally, several authors have proposed mechanistic models of single-component hybridization combining mass transport of target and chemical interactions on the surface of the array [13]. Their efforts resulted in an emerging consensus theoretical approach, which addresses the effects of three-dimensional and two-dimensional (surface-bound) mass transport, and surface chemistry, i.e., probe interactions, probe density, and steric hindrances by introducing efficient (or apparent) rate constants or more complicated rate functional parameters. However, all of these studies use a single analyte case for building the models, which limits their applicability in interpreting multi-component mixture, while only a few reports deal with the discrimination problems in mixed DNA targets solutions [14].

In this respect, many conventional SPR-based methods have been developed for SNP sensing, aiming to set direct, label-free detection strategies [15], i.e. avoiding the use of additional biomolecules (i.e. proteins, enzyme, etc.), nanoparticles or intercalating agents to discriminate single base mismatch target. This in view of skipping the drawbacks due to enzyme and protein interference with DNA hybridization [16] or with NPs possible aggregation on the sensing surfaces, thus preventing the further use of the sensor [17].

In the last year, sensors based on localized surface plasmon resonance (LSPR), recently have been subjected to a great scientific interest as an alternative technique to the conventional optical SPR [18]. Indeed LSPR technique allows to take profit from two peculiar features of the sensor structure. In particular, at first one may take advantage from the peculiar configuration of LSPR sensors, consisting in an array of gold nanostructures deposited on a glass substrate, allowing to overcome the critical problem, affecting both SPR and OWLS technique, of the long range sensitivity to the changes in the refractive index extending far away into the solution. In fact, the gold nanostructure employed in the LSPR experiment allows to confine the sensitivity to the medium refractive index changes to 5–30 nm into the solution. This enhances in a peculiar way the sensitivity to the refractive index changes at the very interface between nanodisks and solution [19].

Secondly, the possibility of using uncovered gold nanostructures distributed onto a SiO_2 surface enables to take profit of the simple thiol chemistry to bind DNA to the surface. In the case of SiO_2 sensing surface of OWLS the surface modification technique are the classical and more complex ones based on [20] a variety of saccharides (such as dextran, gelatin, heparin, etc.) or biomolecules (biotin, streptavidin, etc.) via covalent coupling to silanized waveguides, for example. Different terminal functionalities, such as amine, hydroxyl or carboxyl are also available and allow the further modification of the sensor surface if required by the application.

Analogous to SPR, LSPR can be exploited for biosensing applications, as the wavelength is highly dependent on the refractive index of the surrounding media [21]. The binding on the surface of the nanostructures results in a refractive index change, causing a shift in the extinction peak wavelength, λ_{max}. However, few reports are found in the literature about the application of LSPR sensors for nucleic acids detection [18,22].

In this paper, we develop a single nucleotide mismatch detection method, relevant to KRAS-related pathologies, based on the rapid DNA hybridization process in binary solution. Our approach involves thiolated single strand oligonucleotides immobilized on the nanostructured LSPR sensors, able to reveal the refractive index changes following the DNA hybridization processes. In particular, we have explored the effect of perfect and mismatch target concentration and its time dependence on the sensing performances in a two-component system. The hybridization rate constants for 93–mer sequences are determined for PM and a single nucleotide polymorphism (SNP) mismatch, at a well-defined ionic strength. Additionally, the dynamics of the two-component system versus a single-component system are analyzed, suggesting that the intensity of the relative LSPR signal at a fixed time provides an useful metric to quantify the MM strands fraction in PM-MM binary solutions, i.e., the possibility of using the time response to reveal the presence of single base polymorphism.

2. Materials and methods

2.1. Materials

All DNA strands were obtained from Purimex (Ellipsometry, Germany) in double HPLC-purified grade. Synthetic oligonucleotide sequences for probes and targets are listed in Table S1 of the supporting information. The 5′-thiol-modified probe solutions consisting of a 35-nucleotide long single strand DNA (ssDNA) sequence (henceforth indicated as probe) (-CTA-) were prepared by diluting to a final concentration of 300 nM in 0.1 M PBS and stored at 5 °C. KRAS target length is chosen to be 93-mer to mimic the PCR length sequence target and in order to minimize possible secondary structure, which can lead to inhibited probe-target hybridization and diminished sensitivity of the assay as well as minimizing possible regions where the probes can bind nonspecifically [23]. The chosen targets are the perfect match (PM) (-TAG-), and the mismatch, (MM) (-GCT-) presenting the single base mutation in the central part. The pure target solutions were prepared at various concentrations ranging from 10 nM to 170 nM. The deionized water was purified using a Millipore filtration system and used in all experiments. All measurements were performed in 0.1 M phosphate buffered saline (PBS, pH 7.4) at room temperature. Target solutions were thermally denatured 2 min and snap cooled 3 min, in order to obtain single-stranded targets before using for the LSPR experiments.

2.2. LSPR instrumentation

LSPR measurements are performed in optical transmission mode by using an Insplorion XNano instrument (Insplorion AB, Göteborg, Sweden). A detailed description of the operating principle of LSPR is reported in literature [24].

Briefly, a white light beam entered the measurement chamber, passed through the sensor chip (~4 mm^2 circular spot), and exited through a quartz glass window. The transmitted light is collected by a spectrophotometer, and data analysis is performed with the Insplorer software package (Insplorion AB). The time resolution is 1 Hz. The spectral resolution of the plasmon resonance is determined by high-order polynomial fitting, and the centroid position is calculated from the fit [25]. In this study two different types of sensor chip, both purchased from Insplorion AB, have been used. The first type consists of a glass slide decorated with gold nanodisks, prepared by hole-mask colloidal lithography [26] (see Fig. 1A for an AFM image of the sensor surface). This method yields a partly random distribution of nanostructures on the substrate, which combined with a large particle-particle separation, eliminates both far and near field coupling between the particles so that the measured optical signal reflects the optical (LSPR) response of a single particle [27]. The second type of sensor has a further silicon oxide film (thickness ~10 nm) deposited on top of gold nanodisks by a plasma enhanced chemical vapor deposition (PECVD) technique (Insplorion AB).

The individual gold nanodisk has an average height and diameter of 24 ± 2 nm and 118 ± 5 nm, respectively as indicated by the data of section analysis performed by atomic force microscopy (AFM) technique with Nanoscope IIIa controller (Digital Instrument, Veeco, USA) (see Fig. 1B). The surface coverage is 9 disks per μm^2 (~7% of total area) and the average particle pitch is 330 ± 30 nm.

The bulk sensitivity of the gold nanodisks is 210 ± 17 nm per refractive index unit based on a series of measurements performed using water/ethanol mixtures (see Fig. S2 of SI). The measured sensitivity is in line with previous data by other authors [28] it was concluded that the sensitivity is sufficiently high for biosensing purposes.

Immediately before experiment, both type of sensors are treated with UV Ozone Procleaner (BioForce Nanoscience, Ames, USA) for 15 min, then rinsed with Millipore water and dried under a nitrogen flow.

For the Au and SiO_2 sensor chips, the LSPR plasmon peak, recorded in PBS buffer solution, are found respectively at around 670 and 710 nm (see, e.g., Fig. S1). The baseline LSPR response is recorded in PBS buffer solution. After stabilization of the signal, the PBS buffer solution is replaced by the one containing thiolated ssDNA oligonucleotide. During the experiment, the liquid sample is introduced by peristaltic pump at a constant flow rate of 50 μL/min. After 7 min the pump is shouted down and the signal is recorded until baseline stabilization is obtained (20 min). Then, the PBS solution is again injected into the measurement cell. Finally, the hybridization process is allowed by exchanging the buffer solution with the one containing the ssDNA target strands.

3. Results and discussion

In order to evaluate the sensitivity and specificity of the Au nanodisk arrays as a biosensing platform, hybridization experiments of perfect (PM) and mismatched (MM) oligonucleotides target to the single stranded DNA probe immobilized onto the surface have been performed.

Therefore, at first thiolated single strands of DNA 35 nt (probe) have been immobilized onto the nanoplasmonic LSPR sensor, whose length has been chosen to reduce the unwanted nonspecific interactions [29,30].

The stability of the immobilized probes has been tested by means of an accurate rinsing process with buffer. Finally, the respective yield and rate of the hybridization process for PM and MM targets have been monitored in situ. All data presented in the following paragraphs are the mean of three independent experiments ± standard deviation (SD) (unless mentioned otherwise).

3.1. Probes immobilization onto LSPR sensor

Typical extinction spectra of ssDNA oligonucleotide-modified Au nanodisk arrays is shown in Fig. 2A. The specific binding of ssDNA oligonucleotides caused a red shift in the LSPR resonance, due to the variation of the refractive index from that of PBS buffer (n_{PBS} = 1.33) to that of the DNA layer (n_{DNA} = 1.46) bound to the Au nanostructures [31].

The LSPR signal change, monitored in real-time after the ssDNA probe injection (see Fig. 2B), can be used to figure out the probe immobilization kinetic. The ssDNA probe molecules are stably bound on the Au LSPR sensor surface as indicated by the negligible Δλ change measured after the rinsing step. The anchoring stability can be explained in terms of the synergic effect of the covalently bound terminal thiol and the sequence of 10 adenines adjacent to the linking group, which, according to literature, contribute to the enhancement of the strength of interaction between the ssDNA probe and Au LSPR surface [32].

In order to rule out the possible effect of aspecific interactions, the adsorption of ssDNA probe has been monitored also on SiO_2 coated sensor. In this case, no shift is detected within the experimental error, indicating that the immobilization process is basically driven by the specific formation of covalent bonds between the ssDNA probe molecules with the Au nanodisks (see Fig. 2B).

Assuming that at the steady state, ssDNA molecules forms an uniform adlayer on surface, the plasmon peak shift (1.1 ± 0.2 nm) can be converted in optical thickness [33] according to the following equation:

$$\Delta\lambda = S\left[1 - e^{-\frac{t}{l}}\right](n_{DNA} - n_{buffer}) \quad (1)$$

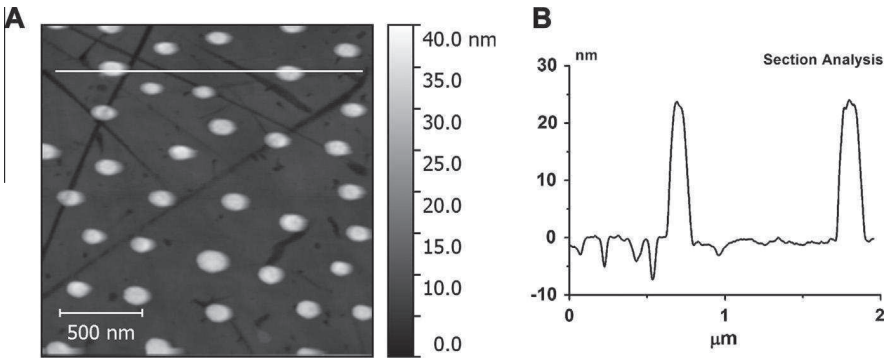

Fig. 1. Atomic force microscopy image of LSPR sensor decorated with gold nanodisks acquired in tapping mode (A) and section analysis (B).

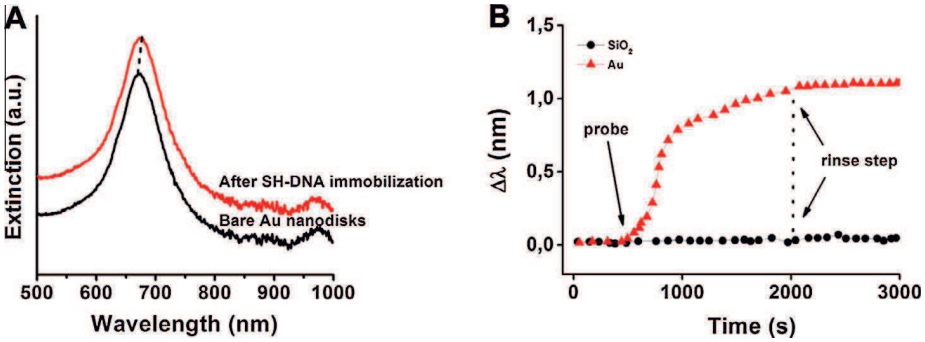

Fig. 2. (A) Representative extinction spectra of the bare Au nanodisk arrays and after immobilization with thiolated ssDNA probe. (B) Plasmon peak shift curves ($\Delta\lambda$) following the binding of thiolated ssDNA probes, respectively on Au nanodisks and SiO_2-coated LSPR sensors.

where S = 72 nm/RIU is the bulk refractive sensitivity of the LSPR sensor (see SI for further details), L = 27.2 nm the decay length of the LSPR evanescent wave according to sensor specification, t is the adsorbed protein layer thickness, n_{DNA} = 1.46 and n_{buffer} = 1.33 are respectively the bulk refractive index for the a uniform ssDNA layer and the buffer solution [31].

The calculated thickness has been further converted in adsorbed mass (M) according to the De Feijter's equation [34],

$$M = t\frac{(n_{DNA} - n_{buffer})}{\left(\frac{dn}{dc}\right)} \quad (2)$$

where dn/dc is the refractive index increment for a concentration change assumed to be nearly constant for protein solutions, at a value of 0.175 cm^3/g [35].

In turn, from the adsorbed mass value the ssDNA surface density, normalized for the gold nanodisks' active area, has been estimated to be of $2.8 \pm 0.1 \times 10^{12}$ molecules/cm^2, which corresponds to $\sim 3.5 \times 10^3$ molecules for each Au nanodisk.

In our condition the average [effective area]/[probe molecule] is $\sim$35 nm^2, i.e., about seven times higher than the value calculated ($\sim$5 nm^2) for ssDNA strands of the same length under high ionic force condition [36]. This rules out the possibility that steric hindrance between DNA strands becomes a significant barrier to hybridization [37]. Furthermore, the value of association rate constant, estimated using a simple Langmuir kinetics equation [37], is $1.64 \pm 0.02 \times 10^4\ M^{-1}\ s^{-1}$, is higher than the one reported in literature for the immobilization of the same length ssDNA strands onto flat Au surfaces [38] ($5 \times 10^3\ M^{-1}\ s^{-1}$). This, in fact, suggests that the nanostructures significantly enhance the rate of DNA immobilization process.

3.2. Evaluation of sensor performance

Fig. 3 reports the calibration curves generated reporting the plasmon peak (Fig. 3A) and peak shift (Fig. 3B) (measured at saturation) with respect to the concentration of PM and MM targets in solution. The signal increases with the target concentration reproducing a Langmuir isotherm behavior for both types of target over a concentration range from 10 nM to 170 nM.

Taking into account the three data points at low concentrations (see inset in Fig. 3B), we obtained a regression line showing r^2 values of 0.964 and 0.941 for PM and MM target respectively. The detection limit (LOD) of the LSPR DNA sensor was calculated as three times of the standard deviation of the ordinate intercept divided by the slope of the regression line [39,40]. As a result, we found that the LOD for PM is about of 10 nmol/L, while for MM is 13 nmol/L (corresponding respectively to 40 and 52 fmol of target). This sensitivity is in the same range of the ones obtained by using fluorescence methods and PCR-based sequence recognition [5,7].

3.3. Kinetic of probe-target hybridization from single component solution

The comparison of the kinetics of the probe- perfect matching sequence (PM) and probe-single base mutated sequence (MM), where adenine (A) is replaced by cytosine (C) in the MM sequence, may be used to determine the dependence of the hybridization process on the base mispairing.

The kinetic curves, obtained exposing the ssDNA layer to a series of MM and PM solutions with concentration ranging from 10 nM to 170 nM are shown in Fig. 4A and B. The shift of the plasmon peak gradually increases with time both for the probe-PM and

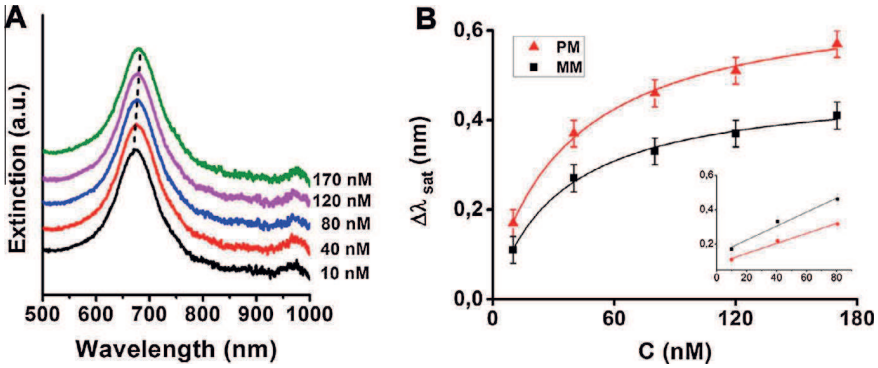

Fig. 3. (A) Representative extinction spectra of the functionalized Au nanodisks after hybridizing with various concentrations of perfect match complementary DNA (PM) and single base mismatch DNA (MM). (B) Calibration curves plotting the maximum peak shift at saturation versus DNA concentrations over the full range of concentrations (main plot) and for the lower concentration point (inset), together with the fitted curves.

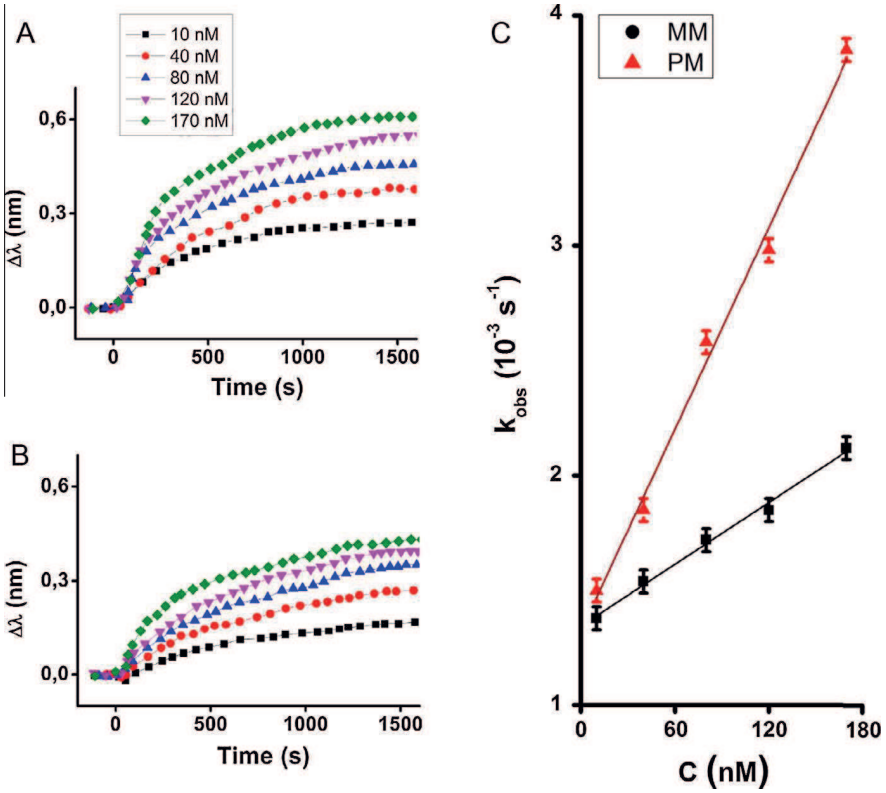

Fig. 4. Kinetic analysis of PM and MM targets interacting with surface bound probe molecules. A,B: Association of PM (A) and MM (B) ssDNA with surface bound probe strands monitored as change with time in the LSPR peak wavelength (Δλ) for different target concentration (10,40,80,120,170 nM). C: Apparent rate constants k_{obs} from kinetic curve of Δλ (t) for PM (triangle symbols) and MM (square symbols) target versus concentration (10 nM to 170 nM); solid lines are linear fits, $k_{obs} = C \cdot k_a$. Each point is the linear regression slope (±standard deviation, SD) of three independent experiments, $R^2 > 90\%$.

probe-MM hybridization. The signal reaches the steady state at shorter time for higher concentrations. In particular, for the highest concentration (170 nM) is stabilized after about 16 and 27 min respectively for PM and MM.

According to the literature [41,42], in order to evaluate the hybridization rate constant, k_a, the hybridization process was treated as an adsorption process. Since we performed the hybridization experiment under an excess of target strands compared to number of probe molecules tethered on surface, we can assume that the whole process can be treated as a pseudo-first order one [43,44], according to the following rate equation [14]:

$$\frac{d(\Delta\lambda)}{dt} \propto \frac{dB}{dt} = k_a C(R_t - B) \tag{3}$$

where Δλ represents the plasmon shift, and it is assumed to be directly proportional to the surface concentration of bound targets, B. C is the concentration of target in solution and R_t is the initial surface concentration of probes.

In our experimental condition, dissociation rate constants are negligible (no target dissociation is observed during post-hybridization buffer rinse experiments) and therefore only one variable (k_a) is considered in the fitting analysis for surface kinetic data. Moreover, if the negligibly small dissociation rate constant was considered as a second fitting parameter, then the resulting k_a value obtained from fitting analysis does not change, although it would have a larger error.

The solution of the previous equation is the following:

$$B = R_t[1 - e^{-(k_{obs}t)}] \tag{4}$$

where k_{obs} is the apparent rate constant, depending on the target concentration in solution according to the relationship reported below:

$$k_{obs} = Ck_a \tag{5}$$

According to above assumptions, the peak shift as a function of time, $\Delta\lambda_t$, is proportional to the adsorbed mass at surface, i.e., to the surface concentration of bound targets, B. Accordingly, a single exponential function can be used to fit the experimental data,

$$\Delta\lambda_t \propto [1 - e^{-(k_{obs}t)}] \tag{6}$$

Fig. 4C reports the Plot of the measured k_{obs} versus the target concentration in solution, C, for PM and MM sequences. As one can see, a linear relationship is obtained, as expected from literature [12], which can be used to determine the intrinsic rate constant k_a by a simple linear regression.

In particular, the value of k_a is found to be higher for PM sequences, $1.46 \pm 0.06 \times 10^4\ M^{-1}\ s^{-1}$, than the k_a value for MM sequences, $4.5 \pm 0.2 \times 10^3\ M^{-1}\ s^{-1}$. This confirms that the hybridization of fully complementary strand (PM) is a significantly faster process compared to the one of mismatched sequences (Fig. 4A and B).

3.4. Competitive PM vs MM hybridization (binary solutions)

An important consideration for clinical translation is the ability to detect a point mutation (i.e., the single base defect) in a mixed sample [45], containing both mutant and perfect match DNA. In order to determine the capability of the present method to detect the mutation point, we investigated various binary solutions with different mutant/perfect match molar ratio, maintaining constant the total concentration at 40 nM.

The kinetic of hybridization for a 40:60, 50:50, 60:40, 70:30 and 80:20 PM/MM target solutions are shown in Fig. 5A. After injecting the solution, the plasmon peak shift was measured at the same

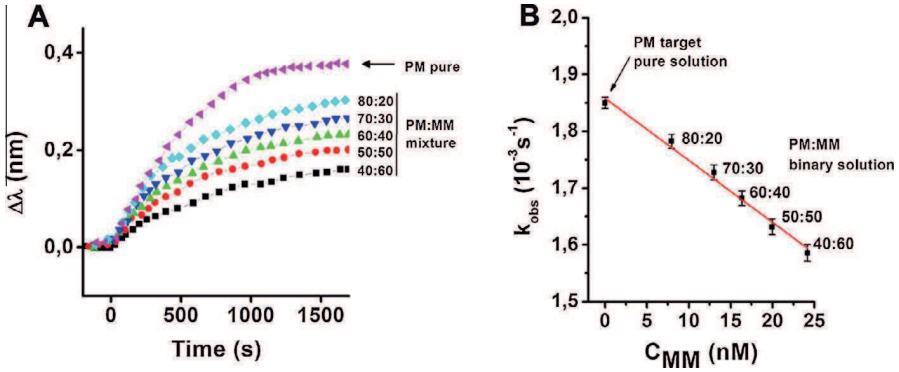

Fig. 5. Kinetic analysis of two-component systems (PM and MM) interacting with surface bound probe molecules as a function of time for different molar ratio (80:20, 70:30, 60:40, 50:50 and 40:60 PM/MM ratio). Peak shift (Δλ) measured at saturation for different molar ratio compared to the PM at 40 nM. (B) Rate constants k_{obs} from kinetic curve of Δλ (t) for PM pure solution and PM: MM binary solution versus MM target concentration; red solid lines is linear fits. Each point is the linear regression slope (±standard deviation, SD) of three independent experiments, $R^2 > 90\%$.

time for all the binary solutions, corresponding to the average time (20 min) until the equilibrium is reached between the bulk concentration and the corresponding hybridization steady state for the 40 nM reference PM concentration, taken as reference. After the reference time the experiment was stopped.

As shown in Fig. 5A, the hybridization from the two-component systems resulted in lower yield, with a lower peak shift compared to the one measured for the reference 40 nM solution of pure PM hybridization. In particular, the rate of hybridization is found to decrease with the increasing fraction of MM in the binary solution.

This suggests that presence of MM target kinetically interferes with the PM hybridization process, behaving as competitor.

In order to clarify this effect, we have applied the rate equation developed by Bishop [14] to describe the hybridization rate for mixtures of perfect match/mismatch targets.

The binary solution with PM and a MM target, can be described by a system of equations similar to those used for pure target solution (see Eq. (1)). The equations have to reflect the consumption of available probe sites due to both the match and mismatch:

$$\frac{dB^m}{dt} = k_a^m C^m \left(R_t - B^m - B^{mis}\right) \tag{7}$$

$$\frac{dB^{mis}}{dt} = k_a^{mis} C^{mis} \left(R_t - B^m - B^{mis}\right) \tag{8}$$

where C^m corresponds to the concentration of perfectly matched target, C^{mis} corresponds to the concentration of the mismatch target, B^m is the bound concentration by the match and B^{mis} is the bound concentration by the mismatch, with the corresponding hybridization rate constants.

Since LSPR measures the rate of the overall hybridization process, we have to consider the sum of the Eqs. (5) and (6) obtaining the following equation:

$$\frac{dB^{tot}}{dt} = \left(k_a^m C^m + k_a^{mis} C^{mis}\right)\left(R_t - B^{tot}\right) \tag{9}$$

where B^{tot} is the sum of the concentration of B^m and B^{mis}.

Due to the fact that, in our experimental conditions, the total concentration of the binary mixture is constant (C_0), the Eq. (7) can be rearranged as it contains only the concentration term of the mismatch target:

$$\frac{dB^{tot}}{dt} = \left[k_a^m C_0 - (k_a^m - k_a^{mis}) C^{mis}\right]\left(R_t - B^{tot}\right) \tag{10}$$

where the term $\left[k_a^m C_0 - \left(k_a^m - k_a^{mis}\right) C^{mis}\right]$ represents the apparent rate constant (k_{obs}) for the hybridization from binary solution.

In Fig. 5B the k_{obs} values obtained by the Langmuir fitting of LSPR curves reported in Fig. 5A, are plotted as a function of the mismatch target concentration in the mixture. As reference value we also reported the k_{obs} for pure perfect matched target at 40 nM. A linear equation can fit the experimental points for two component solutions indicating that the apparent rate constant decrease linearly with the increasing mismatch target concentration. Moreover, the value of the slope is found in fair agreement with the above reported difference of hybridization rate constants for perfect match and mismatch target (see Section 3.3).

Accordingly, in presence of the competing MM sequences, for a given time, a higher amount of substrate molecules is required to reach half of the Δλ maximum signal, with respect to the case of the uninhibited case (Fig. 5A).

On the other hand, from the solid red line in Fig. 5B, representing the apparent rate constant for the mixture, we may figure out an indication on the presence or not of mutation and we can also estimate the relative molar ratios. This finding is obviously valid under the assumptions that the two targets in the mixture adsorb each with its own value of k_a, that is, $k_a^m > k_a^{mis}$ (see Fig. 4C) and that the measurement of peak shift for the two-component systems reflects the two-components composition of the solution.

4. Conclusions

In summary, we have investigated the effects of single base mutation on the competitive hybridization rate between surface-bound DNA probes and DNA target strands in solution.

LSPR sensors, that when compared to other optical techniques, allows the detection of biomolecular interactions in localized sensing volume skipping the interfering effect of the bulk of solution, were used to demonstrated at first the efficient probe immobilization on gold nanodisks in a nondestructive manner and also to detect both perfect matching (PM) and mismatching (MM) targets hybridization, with a limit of detention in the range of 10 nmole/L.

Furthermore, this allowed to measure the "effective" hybridization kinetics and affinity for the various systems. Indeed, it has been found a probe-PM target hybridization faster and stronger than the one of probe-MM target interaction. In turn, the single component isotherms determined for the two DNA strands enabled the unraveling of the more complex process occurring for binary solution.

Under the assumption that both PM and MM may hybridize with the surface-anchored probes in the binary solutions, it has been shown that the MM sequences play a clear inhibition role on the hybridization rate of PM strand.

In summary, the present approach, while keeping comparable sensitivity with techniques as fluorescence or PCR-based methods, allows the single step and label-free discrimination of subtle hybridization steps, providing a valuable improvement with respect to the recent literature, either employing in silico simulations [14], or multistep processes implying manipulation of the samples to be analyzed [12].

Further studies are in progress in our laboratory to exclude the possible presence of single mutation sequences (MM) on the sensing surfaces. We feel that the results here presented may provide significant improvement in view of their application to the DNA array-based technologies.

Author contributions

Author contributed equally to this work. All authors have given approval to the final version of the manuscript.

Conflict of interest

The authors declare no competing financial interest.

Acknowledgement

The authors acknowledge the financial support of FIR 2014 (University of Catania).

Appendix A. Supplementary material

List of probe and target sequences. Bulk refractive index calibration for LSPR sensor. Supplementary data associated with this article can be found, in the online version, at http://dx.doi.org/10.1016/j.jcis.2016.10.026.

References

[1] F.S. Collins, Medical and societal consequences of the Human Genome Project, N. Engl. J. Med. 341 (1999) 28–37.
[2] T. Song, S. Xiao, D. Yao, F. Huang, M. Hu, H. Liang, An efficient DNA-fueled molecular machine for the discrimination of single-base changes, Adv. Mater. 26 (2014) 6181–6185.
[3] O. Kranenburg, The KRAS oncogene: past, present, and future, Biochim. Biophys. Acta 1756 (2005) 81–82.
[4] D. Shao, Y. Lin, J. Liu, L. Wan, Z. Liu, S. Cheng, L. Fei, R. Deng, J. Wang, X. Chen, L. Liu, X. Gu, W. Linag, P. He, J. Wang, M. Ye, J. He, A targeted next-generation sequencing method for identifying clinically relevant mutation profiles in lung adenocarcinoma, Sci. Rep. 6 (2016) 22338–22347.
[5] S.I. Stoeva, J.-S. Lee, C.S. Thaxton, C.A. Mirkin, Multiplexed DNA detection with biobarcoded nanoparticle probes, Angew. Chem. Int. Ed. 45 (2006) 3303–3306.
[6] M.A. Vlachou, K.M. Glynou, P.C. Ioannou, T.K. Christopoulos, G. Vartholomatos, Development of a three-biosensor panel for the visual detection of thrombophilia-associated mutations, Biosens. Bioelectron. 26 (2010) 228–234.
[7] E.-O. Ganbold, T. Kang, K. Lee, S.Y. Lee, S.-W. Joo, Aggregation effects of gold nanoparticles for single-base mismatch detection in influenza A (H1N1) DNA sequences using fluorescence and Raman measurements, Colloids Surf. B 93 (2012) 148–153.
[8] Y. You, B.G. Moreira, M.A. Behlke, R. Owczarzy, Design of LNA probes that improve mismatch discrimination, Nucleic Acids Res. 34 (2006) e60–e71.
[9] K.K. Jensen, H. Orum, P.E. Nielsen, B. Norden, Kinetics for hybridization of peptide nucleic acids (PNA) with DNA and RNA studied with the BIAcore technique, Biochemistry 36 (1997) 5072–5077.
[10] H. Urakawa, S. El Fantroussi, H. Smidt, J.C. Smoot, E.H. Tribou, J.J. Kelly, P.A. Noble, D.A. Stahl, Optimization of single-base-pair mismatch discrimination in oligonucleotide microarrays, Appl. Environ. Microbiol. 69 (2003) 2848–2856.
[11] L.D.S. Lapitan Jr., Y. Guo, D. Zhou, Nano-enabled bioanalytical approaches to ultrasensitive detection of low abundance single nucleotide polymorphisms, Analyst 12 (2015) 3872–3887.
[12] K. Tawa, D.F. Yao, W. Knoll, Matching base-pair number dependence of the kinetics of DNA-DNA hybridization studied by surface plasmon fluorescence spectroscopy, Biosens. Bioelectron. 21 (2005) 322–329.
[13] D.A. Edwards, S.A. Jackson, Testing the validity of the effective rate constant approximation for surface reaction with transport, Appl. Math. Lett. 15 (2002) 547–552.
[14] J. Bishop, S. Blair, A.M. Chagovetz, A competitive kinetic model of nucleic acid surface hybridization in the presence of point mutants, Biophys. J . 90 (2006) 831–840.
[15] M.L. Ermini, S. Mariani, S. Scarano, M. Minunni, Bioanalytical approaches for the detection of single nucleotide polymorphisms by Surface Plasmon Resonance biosensors, Biosens. Bioelectron. 61 (2014) 28–37.
[16] H. Šípová, J. Homola, Surface plasmon resonance sensing of nucleic acids: a review, Anal. Chim. Acta 773 (2013) 9–23.
[17] R. D'Agata, G. Spoto, Artificial DNA and surface plasmon resonance, Artif. DNA PNA XNA 3 (2012) 45–52.
[18] G.A. Lopez, M.C. Estevez, M. Soler, L.M. Lechuga, Recent advances in nanoplasmonic biosensors: applications and lab-on-chip integration, Nanophotonics (2016), http://dx.doi.org/10.1515/nanoph-2016-010.
[19] K.A. Willets, R.P. Van Duyne, Localized surface plasmon resonance spectroscopy and sensing, Annu. Rev. Phys. Chem. 58 (2007) 267–297.
[20] J. Voros, J.J. Ramsden, G. Csùcs, I. Szendrő, S.M. De Paula, M. Textor, N.D. Spencer, Optical grating coupler biosensors, Biomaterials 23 (2002) 3699–3710.
[21] A.B. Dahlin, N.J. Wittenberg, F. Höök, Sang-Hyun Oh, Promises and challenges of nanoplasmonic devices for refractometric biosensing, Nanophotonics 2 (2013) 83–101.
[22] S.L. Dodson, C. Caob, H. Zaribafzadeha, S. Lic, Q. Xionga, Engineering plasmonic nanorod arrays for colon cancer marker detection, Biosens. Bioelectron. 63 (2015) 472–477.
[23] J. SantaLucia (Jr), D. Hicks, The thermodynamics of DNA structural motifs, Annu. Rev. Biophys. Biomol. Struct. 33 (2004) 415–440.
[24] E.M. Larsson, M.E.M. Edvardsson, C. Langhammer, I. Zoric, B. Kasemo, A combined nanoplasmonic and electrodeless quartz crystal microbalance setup, Rev. Sci. Instrum. 80 (2009) 125105–125110.
[25] K. Johansen, R. Stalberg, I. Lundstrom, B. Liedberg, Surface plasmon resonance: instrumental resolution using photo diode arrays, Meas. Sci. Technol. 11 (2000) 1630–1638.
[26] H. Fredriksson, Y. Alaverdyan, A. Dmitriev, C. Langhammer, D.S. Sutherland, M. Zäch, B. Kasemo, Hole-mask colloidal lithography, Adv. Mater. 19 (2007) 4297–4302.
[27] C. Huang, J. Ye, S. Wang, T. Stakenborg, L. Lagae, Gold nanoring as a sensitive plasmonic biosensor for on-chip DNA detection, Appl. Phys. Lett. 100 (2012) 173114–1731118.
[28] B. Grunwald, G. Holst, Fibre optic refractive index microsensor based on white-light SPR excitation, Sens. Actuators, A 113 (2004) 174–180.
[29] K. Knez, D. Spasic, K.P.F. Janssen, J. Lammertyn, Emerging technologies for hybridization based single nucleotide polymorphism detection, Analyst 139 (2014) 353–370.
[30] S. Ikuta, K. Takagi, R.B. Wallace, K. Itakura, Dissociation kinetics of 19 base paired oligonucleotide-DNA duplexes containing different single mismatched base pairs, Nucleic Acids Res. 15 (1987) 797–811.
[31] E. Özkumur, S. Ahn, A. Yalçın, C.A. Lopez, E. Çevik, R.J. Irani, C. DeLisi, M. Chiari, M. Selim, Ünlü. Label-free microarray imaging for direct detection of DNA hybridization and single-nucleotide mismatches, Biosens. Bioelectron. 25 (2010) 1789–1795.
[32] M. Yang, H.C.M. Yau, H.L. Chan, Adsorption kinetics and ligand-binding properties of thiol-modified double-stranded DNA on a gold surface, Langmuir 14 (1998) 6121–6129.
[33] M.P. Jonsson, P. Jönsson, F. Höök, Simultaneous nanoplasmonic and quartz crystal microbalance sensing: analysis of biomolecular conformational changes and quantification of the bound molecular mass, Anal. Chem. 80 (2008) 7988–7995.
[34] J.A. de Feijter, J. Benjamins, F.A. Veer, Ellipsometry as a tool to study the adsorption of synthetic and biopolymers at the air-water interface, Biopolymers 17 (1978) 1759–1772.
[35] S. Vogt, Q. Su, C. Gutiérrez-Sánchez, G. Nöll, Critical view on electrochemical impedance spectroscopy using the ferri/ferrocyanide redox couple at gold electrodes, Anal. Chem. 88 (2016) 4383–4390.
[36] A.B. Steel, R.L. Levicky, T.M. Herne, M.J. Tarlov, Immobilization of nucleic acids at solid surfaces: effect of oligonucleotide length on layer assembly, Biophys. J. 79 (2000) 975–981.
[37] A. Halperin, A. Buhot, E.B. Zhulina, Sensitivity, specificity, and the hybridization isotherms of DNA chips, Biophys. J. 86 (2004) 718–730.
[38] R. Marie, H. Jensenius, J. Thaysen, C.B. Christensen, A. Boisen, Adsorption kinetics and mechanical properties of thiol-modified DNA-oligos on gold investigated by microcantilever sensors, Ultramicroscopy 91 (2002) 29–36.
[39] X. Liu, W. Tan, A fiber-optic evanescent wave DNA biosensor based on novel molecular beacons, Anal. Chem. 71 (1999) 5054–5059.
[40] P.A. Piunno, U.J. Krull, R.H. Hudson, M.J. Damha, H. Cohen, Fiber-optic DNA sensor for fluorometric nucleic acid determination, Anal. Chem. 67 (1995) 2635–2643.
[41] T. Liebermann, W. Knoll, Surface-plasmon field-enhanced fluorescence spectroscopy, Colloids Surf. A 171 (2000) 115–130.
[42] T. Liebermann, W. Knoll, P. Sluka, R. Herrmann, Complement hybridization from solution to surface-attached probe- oligonucleotides observed by surface-plasmon-field-enhanced fluorescence spectroscopy, Colloids Surf. A 169 (2000) 337–350.

[43] S.M. Schreiner, D.F. Shudy, A.L. Hatch, A. Opdahl, L.J. Whitman, D.Y. Petrovykh, Controlled and efficient hybridization achieved with DNA probes immobilized solely through preferential DNA-substrate interactions, Anal. Chem. 82 (2010) 2803–2810.

[44] A. Halperin, A. Buhot, E.B. Zhulina, On the hybridization isotherms of DNA microarrays: the Langmuir model and its extensions, J. Phys.: Condens. Matter 18 (2006) S463–S490.

[45] T. Naiser, O. Ehler, J. Kayser, T. Mai, W. Michel, A. Ott, Impact of point-mutations on the hybridization affinity of surface-bound DNA/DNA and RNA/DNA oligonucleotide-duplexes: comparison of single base mismatches and base bulges, BMC Biotechnol. 8 (2008) 48–70.

Supporting Informations

Kinetic Discrimination of DNA single-base mutations by Localized Surface Plasmon Resonance

Antonino Rapisarda, Nicoletta Giamblanco and Giovanni Marletta*

Laboratory for Molecular Surfaces and Nanotechnology (LAMSUN), Department of Chemical Science, University of Catania and CSGI, Italy

Table S1. List of probe and target sequences.

Name	Sequence (5'→3')
Probe	SH-AAAAAAAAAAGCCTACGCCACTAGCTCCAACTACC
Perfect match target	GAC TGA ATA TAA ACT TGT GGT AGT TGG AGC TAG TGG CGT AGG CAA GAG TGC CTT GAC GAT ACA GCT AAT TGA GAA TCA TTT TGT GGA CGA ATA
Mismatch target	GAC TGA ATA TAA ACT TGT GGT AGT TGG AGC TCG TGG CGT AGG CAA GAG TGC CTT GAC GAT ACA GCT AAT TGA GAA TCA TTT TGT GGA CGA ATA

Bulk refractive index calibration for LSPR sensor

The surface plasmon resonance phenomenon is very sensitive to changes of the refractive index near the gold surface. Regardless of any surface-binding event, the increase of refractive index around the nanostructure will induce a red shift of the maximum in the LSPR extinction signal towards higher wavelengths. This value referred as bulk refractive index sensitivity $\left(S_{bulk}\right)$ characterizes the refractometric sensing performance of the LSPR system. It is defined by the following equation

$$S_{bulk} = \left(\frac{\partial \lambda_{SP}}{\partial n} \right) \tag{S1}$$

where λ_{SP} is the wavelength of the plasmon peak maximum and n is the refractive index of the non-interacting medium close to the plasmonic nanostructures.

The bulk refractive index has been measured respectively for bare Au nanodisks array and for the sensors coated with a 10 nm-thick silicon oxide layer deposited by PECVD (Insplorion AB, Göteborg, Sweden). In Fig S1 are shown the representative extinction spectra for the bare and SiO_2 coated Au nanodisk sensor chips, recorder in PBS buffer.

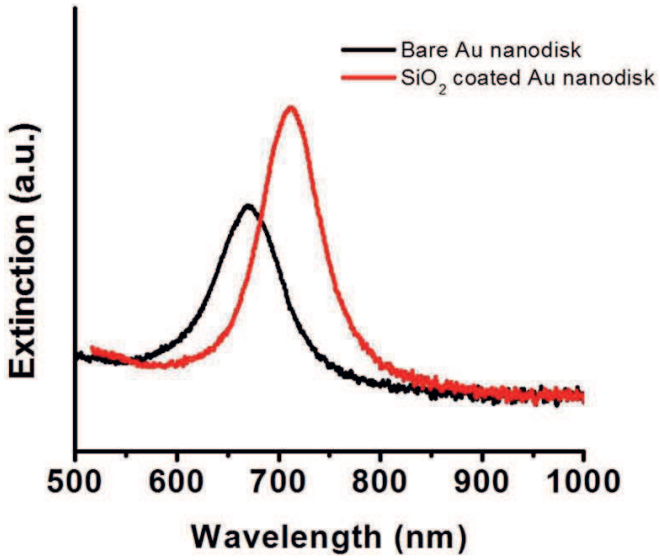

Fig. S1. Representative extinction spectra for the bare and SiO_2 coated Au nanodisks in PBS buffer.

S_{bulk} has been evaluated according the method reported in literature[1].

Water-ethanol mixtures of concentration spanning from 0 to 60% w/w have been prepared resulting in a refractive index n = 1.33 to 1.37.

The calibration solutions have been injected into the measurement cell of LSPR instrument followed by the rinsing with Millipore water. Sensitivity has been determined by plotting the LSPR shift in plasmonic peak maximum wavelength as a function of the measured refractive index (see Fig. S2).

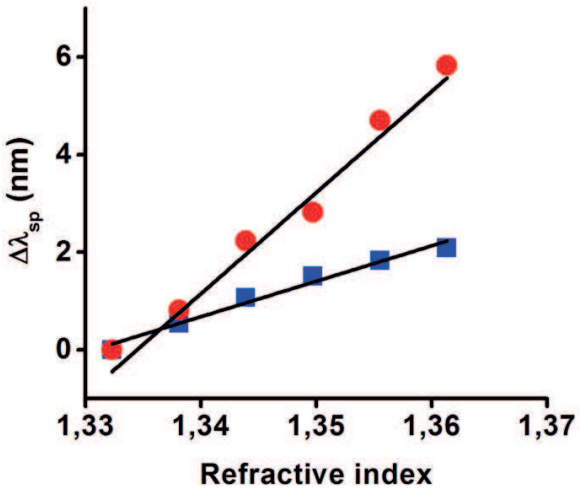

Fig. S2. Calibration curves for refractive index for bare Au nanodisks' array (red circle point) and SiO_2-coated Au nanodisks' array (blue square point). Solid black lines represent the linear fit curves for experimental data.

According to literature, a linear relation between 1.33 and 1.37 refraction index units (RIU) has been observed. Sensitivity (S_{bulk}) is the slope obtained from linear fitting.

As expected, the RI sensitivity of the Au nanodisks' array is 210±17 nm/RIU, about 2.9 times higher than that measured for SiO_2-coated nanodisks (72±5 nm/RIU).

APPENDIX 3:

A. Rapisarda, N. Giamblanco, G. Marletta. Kinetics Study of Adsorption Competition at hydrophobic and hydrophilic surfaces. Colloids and Surfaces B: Biointerfaces (Manuscript submitted

Kinetics Study of Adsorption Competition at hydrophobic and hydrophilic surfaces

*Antonino Rapisarda, Nicoletta Giamblanco, and Giovanni Marletta**

Laboratory for Molecular Surfaces and Nanotechnology (LAMSUN), Department of Chemical Science, University of Catania and CSGI, Italy

ABSTRACT Localized Surface Plasmon Resonance (LSPR), taking profit of its capability to reveal the "dry adsorbed mass", was used to study the adsorption kinetics of single and binary solution of proteins onto model hydrophilic and hydrophobic surfaces. The analysis of the adsorption kinetics, consisting of a two-step process described as sequential diffusion-limited and RSA processes, showed that competitive adsorption occurs, at physiological pH 7.4 and relatively high ionic strength (NaCl 0.1 M), favoring the heavier protein (fibronectin, in our case), which is shown to adsorb faster and in larger amount than the lighter one (human serum albumin, in our case). This process corresponds, at least in the short term, to a non Vroman behaviour. The effect is proposed to be driven by protein-protein and protein-surface electrostatic interaction. In overall, the results provide useful hints to rationalize the behaviour of complex solutions onto weakly or no charged surfaces.

KEYWORDS Localized surface plasmon resonance (LSPR), proteins, adsorption competition, adsorption kinetics, Human Serum Albumin, Human Plasma Fibronectin.

Due to its very complex nature, the study of adsorption of plasma proteins to solid surfaces has been mostly focused either on the quantitative aspects of adsorption of single

proteins, or the reorganization events responsible for the biofunctionality of the adsorbed proteins [1]. Both these aspects of the protein adsorption processes are indeed very important, but it seems obvious that the adsorption processes are strongly conditioned by the inherent kinetics aspects of the whole adsorption process. Thus, important facts such as adsorption selectivity or the adoption of a specific conformation of the adsorbed proteins must be discussed in terms of the previous transport of proteins from the bulk of solution to the solid-liquid interface as well as the kinetics of their binding to the surface, clearly involving also the range and relative strength of the relevant acting surface-molecule interactions [2], and the kinetics of the protein relaxation mode after adsorption [3].

In the last 15 years essentially acoustic and optical detection techniques have been used to monitor the adsorption processes at interfaces [4]. All these techniques have specific strengths and weaknesses regarding, e.g., use of molecule labeling, ease of use, type of information gained, degree of transducer complexity, detection limits and how quantitative the obtained data is [5]. In this context, one of the most used techniques has been the quartz crystal microbalance with dissipation monitoring (QCM-D) allowing to investigate in real time the quantitative and viscoelastic aspects of the protein adsorption [6]. However, a major drawback of the techniques has been shown to concern the determined mass, as it has been shown to include significant and unpredictable amounts of water molecules associated with the adsorbed protein layer and adsorbent surfaces, i.e., the so called “wet mass” [7], thus yielding a basic uncertainty in the interpretation of the data, especially when the matter of interest is the study of protein adsorption on substrates with different hydrophobicity [8].

At variance of this, conventional optical techniques (e.g. surface plasmon resonance (SPR), spectroscopic ellipsometry (SE), optical waveguide lightmode spectroscopy (OWLS)), based on

the analysis of refractive index changes produced by the protein adsorption events and being insensitive to the solvent trapped in the protein adlayer [9], allowed the direct measurement of the real amount of protein molecules in the adsorbed layer, indicated as “dry mass”. Nevertheless, the decay length of the evanescent wave associated with these techniques is at least one or two order of magnitude bigger than the protein layer thickness, limiting the depth resolution of such techniques and making the data critically influenced by bulk refractive index changes [10].

Recently, a new surface sensitive technique, i.e., localized surface plasmon resonance (LSPR), has been developed, based on the sensing properties of evanescent waves propagating just for a few nanometers from the sensing surface (5-30 nm) [11]. The LSPR technique has proved to be particularly suitable for studies aimed to determine the real adsorbed masses of biomolecule in ultrathin layers, whatever the nature of the substrate [12]. The present paper reports on the use of LSPR to determine the real kinetics, i.e., skipping the perturbing effect of different hydration contribution to the adsorbed protein mass, of single and competitive adsorption processes from protein solutions.

In particular, we report the adsorption kinetics of Human Serum Albumin (HSA) and Human Plasma Fibronectin (Fn) from single and binary solutions onto hydrophilic and hydrophobic model surfaces, obtained by functionalization of nanostructured LSPR sensor chips (Insplorion AB, Göteborg, Sweden), consisting of a glass slide decorated with gold nanodisks 25 nm high, with an average diameter of ~120 nm, spaced about 200 nm and coated with a thin layer of silicon oxide (~10 nm) deposited on the top of gold nanodisks (Insplorion AB). This set up, indeed, protects the plasmonic sensing elements from the harsh solution environment. The

arrangement of the nanodisks on the sensing surface is shown in the Atomic Force Microscopy image reported in Fig. S1 of the Supporting Information.

Briefly (see SI for experimental details), the hydrophilic surfaces were prepared by treating the LSPR sensor surface in an UV-O_3 discharge (these samples will be henceforth indicated as Hyl-SiO_2). The hydrophobic surfaces were prepared by depositing a monolayer of Octadecyltrichlorosilane (henceforth indicated as OTS) on the surface of the SiO_2-coated LSPR sensor.

The real-time adsorption of the protein "dry" mass was detected by means of an Insplorion XNano instrument (Insplorion AB, Göteborg, Sweden) (see SI for a detailed description of the apparatus), providing the plasmonic peak shift ($\Delta\lambda$) as a function of adsorbed matter and time.

Fig. 1 reports the LSPR response for the adsorption of HSA and Fn, respectively, onto Hyl-SiO_2 and OTS substrates at 25°C from a 100 μg/ml protein solution prepared in 0.01 M phosphate buffer (PBS), pH 7.4.

Assuming that each adsorbed protein, at the steady state, forms an uniform adlayer on both surfaces, the LSPR response can be converted in optical thickness [13] according to the following equation:

$$\Delta\lambda = S\left[1 - e^{-\frac{t}{L}}\right]\left(n_{protein} - n_{buffer}\right) \qquad Eq.\,1$$

where S=76.4 nm/RIU is the bulk refractive sensitivity of the LSPR sensor, L=27.2 nm the decay length of the LSPR evanescent wave, t is the adsorbed protein layer thickness, $n_{protein}$=1.456 and n_{buffer}=1.335 are respectively the bulk refractive index for the a uniform proteinaceous layer and the buffer solution [14].

The protein adlayer thickness ca be further converted in dry mass (M) according to the De Feijter's equation [15],

$$M = t\frac{n_{protein} - n_{buffer}}{\frac{dn}{dc}} \qquad Eq.2$$

Where dn/dc is the refractive index increment for a concentration change assumed to be nearly constant for protein solutions, at a value of 0.18 cm^3/g [16].

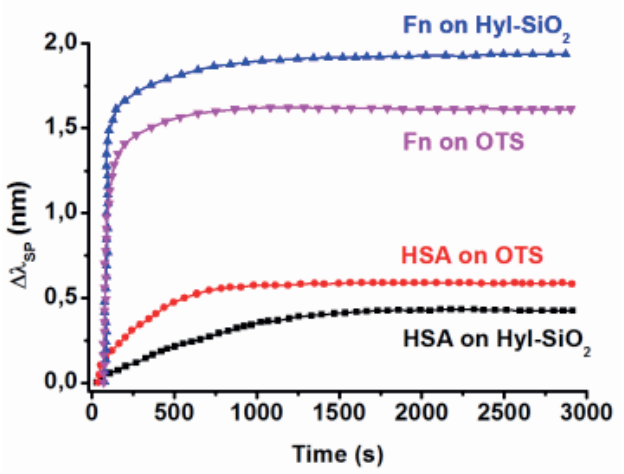

Figure 1. Single protein adsorption curves by LSPR respectively for HSA and Fn solutions (100 μg/ml, buffer PBS 0.01 M, pH = 7.4, T= 25.0 °C).

Fig.1 reports the shift of the plasmon wavelength for the HSA and Fn adsorption processes, which, converted in effective thickness by using equ.2, shows that, for both surfaces, the adsorbed amount of Fn is higher than the one of HSA. Furthermore, while the amount of adsorbed HSA is slightly higher for OTS surfaces (with an effective thickness of the adsorbed layer t = 2.2 nm), than for Hyl-SiO_2 (t = 1.5 nm), Fn adsorption follows an opposite trend, with a higher adsorption onto Hyl-SiO_2 (t = 7.8 nm) than onto OTS (t = 5.9 nm). It is to note that the measured thickness of the adsorbed protein layers is lower than the protein native dimension both for HSA (4x4x14 nm^3) and Fn (16.5 x 9.6 x 2.5 nm^3). According to well-established

literature, globular HSA predominantly undergoes a drastic denaturation process Fn is adsorbed in a random/non-oriented fashion yielding the thickness reported above is intermediate between the two molecular shorter axes, i.e., 9.6 and 2.5 nm. In overall, these findings are in nice agreement with previous reports for albumin and fibronectin [17, 18]. LSPR experiments suggest that the kinetics adsorption paths for the two proteins and the two surfaces can be simply analyzed in terms of a two-step model, including a first, an almost linear and fast step corresponding to a simple diffusion-controlled kinetic model [19], followed by a second slow adsorption step, corresponding to a simple random sequential adsorption (RSA) model [20].

In particular, the first step can be fitted in the framework of the above mentioned diffusion-controlled model by using the following equation [19]:

$$M = 2C_b\sqrt{\frac{D}{\pi}}t^{\frac{1}{2}} \qquad Eq.3$$

where M is the adsorbed mass, C_b is the protein concentration in the bulk solution and D is the diffusion coefficient of the protein from the solution to the adsorbent surfaces. According to the equation, we obtained that the very early rising adsorption steps are fitted with straight lines, one characterized by a peculiar value of the diffusion coefficient D for each protein, corresponding to the different slope of the adsorption process respectively for HSA and Fn (see Figure 2 A).

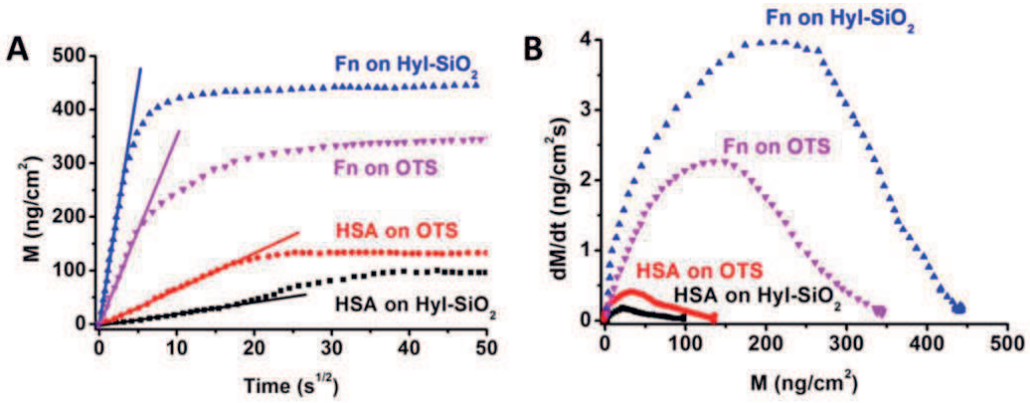

Figure 2. (A) Protein adsorbed mass (ng/cm^2) vs. square root of time (s$^{1/2}$). The straight line fit of the 1st adsorption steps is shown for each curve. (B) Rate of adsorption as a function of deposited mass density for HSA and Fn solution (100 μg/ml, buffer PBS 0.01 M, pH = 7.4, T= 25.0 °C).

It can be seen that, counterintuitively, the heavier Fn molecules adsorb with a faster diffusion-controlled kinetics, with respect to the slower kinetics of HSA adsorption. A minor effect can be seen to discriminate a slightly higher D value for HSA adsorption onto OTS, while as above indicated, Fn appears to diffuse faster to Hyl-SiO_2 surfaces.

The data of adsorbed mass at saturation and estimated diffusion coefficient are summarized in Table 1. It is to mention that, for both hydrophilic and hydrophobic surfaces, the measured D are about two or three order of magnitude lower than the bulk solution values reported, in similar conditions of pH (7.2), buffer and ionic force, for HSA (D_{bulk}= 6.4 x10^{-7} cm^2/s) [21] On the contrary, the measured D values for Fn are of the same order of the values reported in literature for this protein (D_{bulk} = 2.11x10^{-7} cm^2/s) [22]. We suggest that the observed difference for HSA diffusion coefficient can be related with repulsive protein –surface interactions strongly reduce to the D values for the protein [23]. Indeed it should be pointed out that D represents an "effective" diffusion coefficient, reproducing the success of adsorption events, critically depending on the peculiar chemical and structural features of the adsorbent surfaces.

Table 1. Adsorbed mass, Diffusion coefficients (D) and RSA affinity constant (k_a) for single and protein mixture on Hyl-SiO_2 and OTS surfaces by LSPR.

Protein	Surface	Mass (ng/cm^2)	D (cm^2/s)	k_a (cm/s)
HSA	Hyl-SiO_2	85±5[a]	(4.0±0.2[b])x10^{-10}	(1.7±0.2[c])x10^{-6}
	OTS	120±5	(3.6±0.1)x10^{-9}	(6.2±0.1)x10^{-6}
Fn	Hyl-SiO_2	430±5	(4.1±0.2)x10^{-7}	(6.6±0.3)x10^{-4}
	OTS	330±5	(9.1±0.3)x10^{-8}	(2.1±0.1)x10^{-4}
HSA + Fn	Hyl-SiO_2	450±5	(4.5±0.4)x10^{-8}	(1.1±0.1)x10^{-4}
	OTS	370±5	(7.2±0.5)x10^{-9}	(3.9±0.2)x10^{-5}

[a]Mean ± Standard deviation; experiment was performed in triplicate;
[b]Standard error of the linear regression slope; R^2>90%;
[c]Standard error of the Fit as derived from Nonlinear Least-square Fitting with Equation 4;

The second step of adsorption has been analysed according to the random sequential adsorption model (RSA) [20], based on the relationship between protein adsorption rate (dM/dt) and the protein adsorbed mass (M) shown below (see Figure 2 B):

$$\frac{dM}{dt} = mk_a C_b \left[1 + 0.812\frac{Ma}{m\theta_\infty} + 0.4258\left(\frac{Ma}{m\theta_\infty}\right)^2 + 0.0716\left(\frac{Ma}{m\theta_\infty}\right)^3 \times \left(1 - \frac{Ma}{m\theta_\infty}\right)^3 \right] \qquad Eq.4$$

where m is the protein molecular weight, k_a is the adsorption rate constant, C_b is the protein concentration in the bulk solution and θ_∞=0.547 is the maximum coverage in the simplest hard spherical particle approximation, assuming a cubic packing [24].

The RSA analysis confirms the surprisingly higher efficiency of the Fn adsorption events, well represented by k_a values (in the range of 10^{-4} cm^2/s) which are about two order of magnitude higher than the ones estimated for HSA (in the range of 10^{-6} cm^2/s).

As the k_a term in the RSA model represents the effective interaction success, we may argue that the adsorption rate is controlled by the surface/protein interactions in the adopted experimental conditions. In particular, at the pH 7.4, both HSA and Fn are negatively charged,

their isoelectric points being 4.7 and 5.5 [25] respectively, as well as SiO_2 and OTS surfaces at the same pH [26]. In this framework, the high ionic strength condition employed in the present experiments (0.1 M NaCl), determines an estimated Debye length lower than 0.8 nm [26], suggesting that for the smaller (and lighter) Albumin, electrostatic repulsion is significantly higher than for the larger (and heavier) Fn.

Further minor differences in k_a value are seen both for HSA adsorbed on OTS and Hyl-SiO_2 and for Fn onto Hyl-SiO_2 OTS (see Table 1), reflecting the fact that a detailed balance must be taken into account for the interaction of each protein with hydrophobic and hydrophilic surfaces.

In overall, D for the first step and k_a for the second can be assumed as the probability factors that any given protein-to-surface collision will result in an adsorption event, thus providing a "measure" of the adsorption efficiency. Moreover, for both surfaces, the affinity constants are homogeneously higher than the corresponding effective diffusion coefficient confirming that, in the present experimental conditions, the adsorption process occurs in a diffusion limited regime.

The above discussed higher efficiency of the Fn sticking process with respect to HSA suggests that this effect can be used to promote selective adsorption from complex protein mixture. Accordingly, the behaviour of a binary protein solution (HSA+Fn, 200 µg/ml) on both Hyl-SiO_2 and OTS has been studied investigated, employing the very same experimental conditions employed for single protein solutions. As shown in Fig. 3, it has been found that the protein binary solution essentially behaves as the pure Fn solution, with the heavier Fn preferentially adsorbing on both surfaces (see Table 2), also if, for both surfaces, the adsorption kinetic of Fn for the mixture is slower than the one measured for the single component solution (Fig.4), and reflected from the decrease of D and k_s (about a factor of 10).

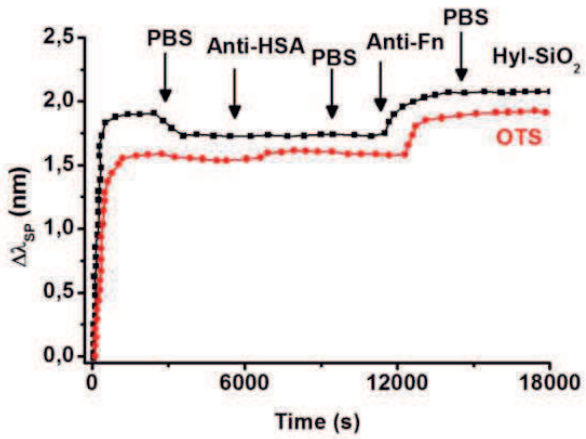

Figure3. Competitive protein adsorption curves by LSPR for a binary solution of HSA + Fn (200 μg/ml, buffer PBS 0.01 M, pH = 7.4, T= 25.0 °C).

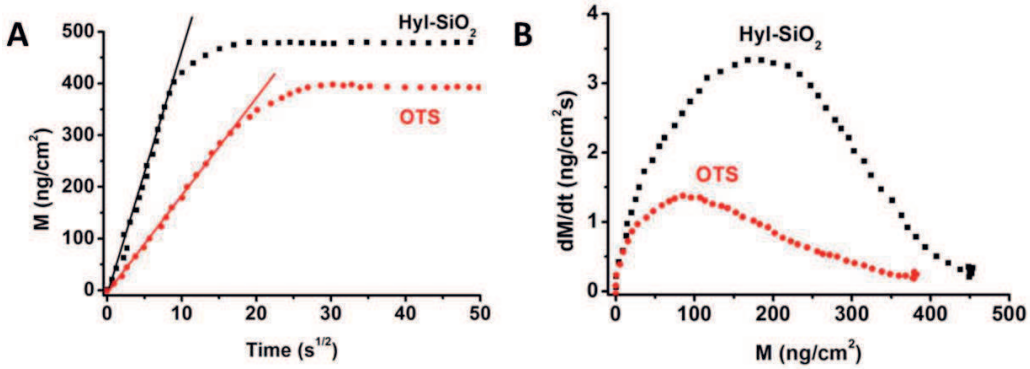

Figure 4. (A) Protein adsorbed mass (ng/cm^2) vs. square root of time (s$^{1/2}$) for the HSA and Fn mixture. The straight line fit of the 1st adsorption steps is shown for each curve. (B) Rate of adsorption as a function of deposited mass density for HSA and Fn mixture (200 μg/ml, buffer PBS 0.01 M, pH = 7.4, T= 25.0 °C).

Anyhow, the occurrence of the preferential fibronectin adsorption was further confirmed by testing the adsorbed protein layer with specific antibody conjugation. The results is reported in Fig.3, where a solution of specific HSA-antibody (Anti-HSA) is injected after the interaction of protein mixture with SiO_2 surface reaches saturation. In fact, no detectable increase of the LSPR signal is observed after the Anti-HSA addition, suggesting that is not present on Hyl-SiO_2 surfaces, while, on OTS surfaces a small response was measured after Anti-HSA injection, being

completely removed during the rinsing step with buffer, suggesting that a mere unspecific adsorption occurred for the antibody molecules for hydrophobic surfaces.

On the contrary, when the Fn antibody (Anti-Fn) solution was injected, a relevant adsorption step is measured on both surfaces, and no desorption was found after the buffer rinsing, suggesting that the Anti-Fn molecules are specifically conjugated.

These effect suggests that a small amount of coadsorbed albumin may slow down the adsorption of Fn.

In summary, the dynamics of albumin and fibronectin “dry mass” adsorption from single and binary protein solutions, studied by taking profit of the capability of LSPR technique of providing the “real” protein adsorbed mass, show that surprisingly, i.e., in spite of its much higher molecular weight, Fibronectin adsorbs faster and in larger amount than albumin on both hydrophilic and hydrophobic surfaces. According to the reported results, we surmise that this non-Vroman behaviour is driven by electrostatic factors, enhanced in the peculiar experimental conditions we used, i.e., pH 7.4 and relatively high ionic strength (NaCl 0.1 M), disfavouring the adsorption of the smaller proteins, if the Debye length, in the peculiar conditions of the solution, is close to their radius of gyration, i.e., increasing the efficiency of the repulsive forces with surfaces of the same charge. Moreover, it turns out that the dynamics of competitive protein adsorption is in agreement with the hypothesis that the diffusion coefficients and the affinity constants obtained for single protein adsorption, remain also valid for binary solutions, i.e., there is no interfering effect of proteins in solutions, such as clustering or association.

In conclusion, the obtained results pave the way to the understanding of the behaviour of complex solutions onto hydrophilic/hydrophobic weakly charged surfaces.

Acknowledgment

The authors acknowledges the financial support of FIR 2014 (University of Catania).

References

1. F. Höök, J. Vörös, M. Rodahl, R. Kurrat, P. Böni, J.J. Ramsden, M. Textor, N.D. Spencer, P. Tengvall, J. Gold, B. Kasemo. A comparative study of protein adsorption on titanium oxide surfaces using in situ ellipsometry, optical waveguide lightmode spectroscopy, and quartz crystal microbalance/ dissipation, Colloids and Surfaces B: Biointerfaces 24 (2002) 155-170.
2. J. Voros. The Density and Refractive Index of Adsorbing Protein Layers, Biophysical Journal, 87 (2004) 553-561.
3. M. F. Mora , J. L. Wehmeyer, R. Synowicki, C. D. Garcia. Investigating Protein Adsorption via Spectroscopic Ellipsometry, in D.A. Puleo and R. Bizios (eds.), Biological Interactions on Materials Surfaces, Springer Science + Business Media, New York, 2009, pp.19-41
4. G. Diaconu, T. Schäfer. Study of the interactions of proteins with a solid surface using complementary acoustic and optical techniques. Biointerphases 9 (2014) 029015.
5. R. Konradi, M. Textor, E. Reimhult. Using Complementary Acoustic and Optical Techniques for Quantitative Monitoring of Biomolecular Adsorption at Interfaces. Biosensors 2 (2013) 341-376.
6. J. L. Jordan, E. J. Fernandez. QCM-D Sensitivity to Protein Adsorption Reversibility. Biotechnology and Bioengineering 101 (2008) 837-842.
7. A. Laschitsch, B. Menges, and D. Johannsmann. Simultaneous determination of optical and acoustic thicknesses of protein layers using surface plasmon resonance spectroscopy and quartz crystal microweighing. Applied Physics Letters 77 (2000) 2252-2254.
8. J. Malmström, H. Agheli, P. Kingshott, D. S. Sutherland. Viscoelastic Modeling of Highly Hydrated Laminin Layers at Homogeneous and Nanostructured Surfaces: Quantification of Protein Layer Properties Using QCM-D and SPR. Langmuir 23 (2007) 9760-9768.
9. C. R. Wittmera, J. A. Phelpsa, W. M. Saltzmanb, P. R. Van Tassel. Fibronectin Terminated Multilayer Films: Protein Adsorption and Cell Attachment Studies. Biomaterials 28 (2007) 851–860.
10. A. J. Haes, R. P. Van Duyne. A unified view of propagating and localized surface plasmon resonance biosensors. Anal Bioanal Chem 379 (2004) 920–930.
11. K. A. Willets, R. P. Van Duyne. Localized Surface Plasmon Resonance Spectroscopy and Sensing. Annu. Rev. Phys. Chem. 58 (2007) 267–297.
12. K. A. Willets, R. P. Van Duyne. Localized Surface Plasmon Resonance Spectroscopy and Sensing. Annu. Rev. Phys. Chem. 58 (2007) 267–297.

13. Jonsson, M. P; Jönsson, P; Höök, F. Simultaneous Nanoplasmonic and Quartz Crystal Microbalance Sensing: Analysis of Biomolecular Conformational Changes and Quantification of the Bound Molecular Mass. Anal. Chem. 80 (2008) 7988–7995.
14. J. Benesch , A. Askendal, P. Tengvall. Quantification of adsorbed human serum albumin at solid interfaces: a comparison between radioimmunoassay (RIA) and simple null ellipsometry. Colloids and Surfaces B: Biointerfaces 18 (2000) 71–81.
15. K. Rechendorff, M. B. Hovgaard, M. Foss, V. P. Zhdanov, F. Besenbacher. Enhancement of Protein Adsorption Induced by Surface Roughness. Langmuir 22 (2006) 10885–10888.
16. C. F. Wertz, M. M. Santore. Adsorption and Relaxation Kinetics of Albumin and Fibrinogen on Hydrophobic Surfaces: Single-Species and Competitive Behavior. Langmuir 15 (1999) 8884-8894.
17. J. B. Lhoest, E. Detrait, P. van den Bosch de Aguilar, P. Bertrand. Fibronectin adsorption, conformation, and orientation on polystyrene substrates studied by radiolabeling, XPS, and ToF SIMS. J Biomed Mater Res. 41 (1998) 95-103.
18. N. Giamblanco, M. Yaseen, G. Zhavnerko, J. R. Lu, and G. Marletta. Fibronectin Conformation Switch Induced by Coadsorption with Human Serum Albumin. Langmuir 27 (2011) 312–319.
19. U. Klueh, T. Seery, D.G. Castner, J.D. Bryers, D.L. Kreutzer. Binding and orientation of fibronectin to silanated glass surfaces using immobilized bacterial adhesin-related peptides. Biomaterials 24 (2003) 3877–3884.
20. J. J. Ramsden. Observation of Anomalous Diffusion of Proteins Near Surfaces. J. Phys. Chem. 96 (1992) 3388-3391.
21. R. Lu, Q. Li, T. H. Nguyen. Random sequential adsorption of human adenovirus 2 onto polyvinylidene fluoride surface influenced by extracellular polymeric substances. Journal of Colloid and Interface Science 466 (2016) 120–127.
22. A. E. Kamholz, B. H. Weigl, B. A. Finlayson, P. Yager. Quantitative Analysis of Molecular Interaction in a Microfluidic Channel: The T-Sensor. Anal. Chem. 71 (1999) 5340-5347.
23. M. Rocco, M. Carson, R. Hantgan, J. McDonagh, J. Hermans. Dependence of the shape of the plasma fibronectin molecule on solvent composition. Ionic strength and glycerol content. J Biol Chem 258 (1983) 14545–14549.
24. F. M. Richards. Areas, volumes, packing and protein structure. Annu Rev Biophys Bioeng. 6 (1977) 151-176.
25. M. Tagaya, T. Ikoma, N. Hanagata, T. Yoshioka, J. Tanaka. Competitive adsorption of fibronectin and albumin on hydroxyapatite nanocrystals. Sci. Technol. Adv. Mater. 12 (2011) 034411- 034416.
26. M. Bellion, L. Santen, H. Mantz, H. Hähl, A. Quinn, A. Nagel, C. Gilow, C. Weitenberg, Y. Schmitt, K. Jacobs. Protein adsorption on tailored substrates: long-range forces and conformational changes. J. Phys.: Condens. Matter 20 (2008) 404226.

Supplementary Information

Kinetics Study of Adsorption Competition at hydrophobic and hydrophilic surfaces

*Antonino Rapisarda, Nicoletta Giamblanco and Giovanni Marletta**

Laboratory for Molecular Surfaces and Nanotechnology (LAMSUN), Department of Chemical Science, University of Catania and CSGI, Italy

LSPR instrumentation

LSPR measurements have been performed in optical transmission mode by using an Insplorion XNano instrument (Insplorion AB, Göteborg, Sweden). A detailed description of the operating principle of LSPR is reported in literature [1].

Briefly, a white light beam entered the measurement chamber, passed through the sensor chip (~4 mm^2 circular spot), and exited through a quartz glass window. The transmitted light is collected by a spectrophotometer, and data analysis is performed with the Insplorer software package (Insplorion AB). The time resolution is 1 Hz. The spectral resolution of the plasmon resonance is determined by high-order polynomial fitting, and the centroid position is calculated from the fit [2].

LSPR sensor chips characterization

The LSPR sensor chips have been used in this study, purchased from Insplorion AB, consists of a glass slide decorated with gold nanodisks, prepared by hole-mask colloidal lithography [3]. This method yields a partly random distribution of nanostructures on the substrate, which combined with a

large particle-particle separation, eliminates both far and near field coupling between the particles so that the measured optical signal reflects the optical (LSPR) response of a single particle [4].

On top of gold nanodisks a thin layer of silicon oxide (~10 nm) is deposited by a plasma enhanced chemical vapor deposition (PECVD) technique (Insplorion AB), in order to protect the plasmonic sensing elements from the harsh solution environment.

The arrangement of the nanodisks on the surface after completed nanofabrication is shown in the Atomic Force Microscopy image reported in Fig. S1 a. The individual nanodisk has an average height and diameter of 25 ± 5 nm and 150 ± 5 nm, respectively as indicated by the data of section analysis performed by AFM technique with Nanoscope IIIa controller (Digital Instrument, Veeco, USA) (see Fig. S1 b). The surface coverage is 9 disks per μm^2 (~7% of total area) and the average particle pitch is 330±30 nm.

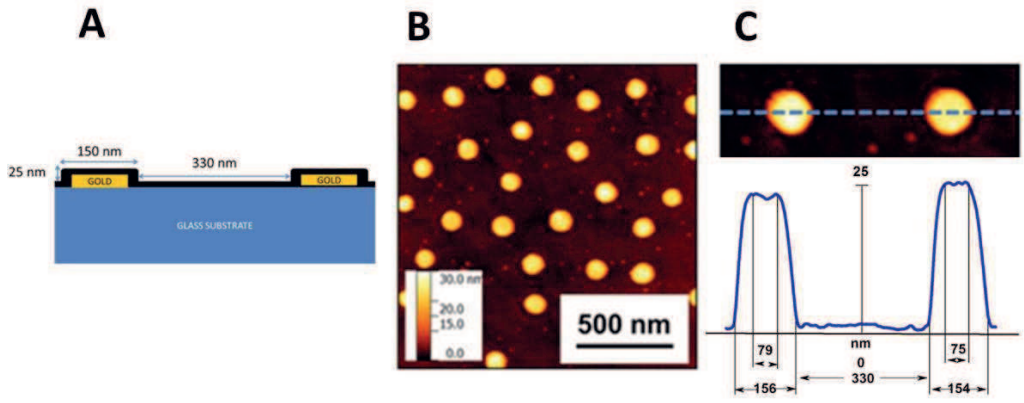

Fig. S1. (A) Schematic description of LSPR sensor structure. (B) AFM image of LSPR sensor chip surface and corresponding section analysis of individual nanodisks (C).

Surfaces preparation

SiO_2-coated LSPR sensor chips were treated with UV-ozone for 15 min then rinsed with Millipore water and dried under a nitrogen flow. Following this treatment, LSPR sensor were either used without

further treatment for the adsorption experiments on hydrophilic surface or were coated with a monolayers of octadecyltrichlorosilane (OTS) for the measurement on the hydrophobic substrate.

The OTS SAM was made by immersing a clean LSPR sensor into a 0.4 mM OTS (Aldrich, >90% solution in a mixture (3:1) of hexadecane (Sigma, >99%) and chloroform (Sigma-Aldrich, 99.8%) at a temperature (ca. 40 °C) in an ambient atmosphere for 60 min. The OTS sample was rinsed with a mixture (3:1) of hexadecane and chloroform, chloroform and methanol. After being dried with a stream of N_2, the SAM-coated sample was stored in a Petri dish.

Static water contact angle measurements were performed to characterize the two surfaces. The surface wettability is analyzed by the sessile drop method with Milli-Q water using a half automatic video-based contact angle meter (OCA30, Data physics). The droplet of 2μl was applied on five different zones of each sample. The measured values were determined to be respectively 18 ± 3° for Hyl-SiO_2 surface and 100 ± 2° for OTS surface, consistent with previous reported data [5].

Experimental method for protein adsorption measurement

All protein adsorption experiment were conducted according to the following experimental procedure.

The blank solution (PBS, 0.01 M, pH 7.4) and protein solution (100 μg/mL in PBS, pH 7.4) were pumped into the flow cell (channel cross-section and length is 1 × 2 and 5 mm, respectively) containing the sensor chip using a peristaltic pump at a constant flow rate of 50 μL/min . The flow cell was maintained at 25 °C by the thermoelectric circuit.

Before exposing the sensor chip surface to the protein solution, the surfaces were equilibrated with the background environment by flushing with the blank PBS solutions. After steady-state was obtained and a flat baseline indicating equilibrium was established, 200 μL of the protein solution was pumped into the measurement cell, and it was allowed to adsorb for 60 minutes under static condition. After the protein solution injection was complete, the adsorption process was monitored until the saturation was

reached. After that, a buffer rinsing for 10 minutes was used to remove reversibly adsorbed molecules from LSPR sensor chip surface.

For competitive adsorption experiments, after the PBS buffer rinsing, further 200 μL of Monoclonal antibody of Albumin (Sigma-Aldrich, product code n° A6684) solution (0.2 μg/mL in PBS, pH 7.4) was introduced, and allowed to adsorb for 40 minutes under static condition in order to ensure it had equilibrated. PBS buffer was pumped over the protein/antibody layer at a flow rate of 50 μL, until any weakly bound albumin antibody molecules was removed from the surface. After the second buffer rinsing, 200 μL of Polyclonal rabbit antifibronectin (Sigma-Aldrich, product code n° F3648) solution (0.2 μg/mL in PBS, pH 7.4) was introduced, and allowed to adsorb for 40 minutes under static condition. Finally, a further PBS rinsing was performed in order to displace any weakly bound fibronectin antibody molecules.

Identical experiments were carried out at least three times on each specimen to obtain statistical information and representative data curves at median were reported herein.

References

[1] E.M. Larsson, M.E.M Edvardsson, C. Langhammer, I. Zoric, B Kasemo, A combined nanoplasmonic and electrodeless quartz crystal microbalance setup. Review Of Scientific Instruments 80 (2009) 125105-125110.

[2] K. Johansen, R. Stalberg, I. Lundstrom, B. Liedberg, Surface plasmon resonance: Instrumental resolution using photo diode arrays. Meas. Sci. Technol. 11 (2000) 1630–1638.

[3] H. Fredriksson, Y. Alaverdyan, A. Dmitriev, C. Langhammer, D.S. Sutherland, M. Zäch, B. Kasemo, Hole–Mask Colloidal Lithography. Adv. Mater. 19 (2007) 4297–4302.

[4] C. Huang, J. Ye, S. Wang, T. Stakenborg, L. Lagae, Gold nanoring as a sensitive plasmonic biosensor for on-chip DNA detection. Appl. Phys. Lett. 100 (2012) 173114-1731118.

[5] D. Janssen, R. De Palma, S. Verlaak, P. Heremans, W. Dehaen. Static solvent contact angle measurements, surface free energy and wettability determination of various self-assembled monolayers on silicon dioxide. Thin Solid Films 515 (2006) 1433–1438.